

Air Force Institute of Technology

**AFIT Scholar**

---

Theses and Dissertations

Student Graduate Works

---

3-2005

## **Biaxial Fatigue Behavior of NiTi Shape Memory Alloy**

Daniel M. Jensen

Follow this and additional works at: <https://scholar.afit.edu/etd>



Part of the [Materials Science and Engineering Commons](#)

---

### **Recommended Citation**

Jensen, Daniel M., "Biaxial Fatigue Behavior of NiTi Shape Memory Alloy" (2005). *Theses and Dissertations*. 3702.

<https://scholar.afit.edu/etd/3702>

This Thesis is brought to you for free and open access by the Student Graduate Works at AFIT Scholar. It has been accepted for inclusion in Theses and Dissertations by an authorized administrator of AFIT Scholar. For more information, please contact [AFIT.ENWL.Repository@us.af.mil](mailto:AFIT.ENWL.Repository@us.af.mil).



**BIAXIAL FATIGUE BEHAVIOR OF NiTi SHAPE MEMORY ALLOY**

THESIS

Daniel M. Jensen, 1<sup>st</sup> Lieutenant, USAF

AFIT/GA/ENY/05-M06

**DEPARTMENT OF THE AIR FORCE  
AIR UNIVERSITY**

**AIR FORCE INSTITUTE OF TECHNOLOGY**

**Wright-Patterson Air Force Base, Ohio**

APPROVED FOR PUBLIC RELEASE; DISTRIBUTION UNLIMITED

The views expressed in this thesis are those of the author and do not reflect the official policy or position of the United States Air Force, Department of Defense, or the U.S. Government.

AFIT/GA/ENY/05-M06

BIAXIAL FATIGUE BEHAVIOR OF NiTi SHAPE MEMORY ALLOY

THESIS

Presented to the Faculty

Department of Aeronautics and Astronautics

Graduate School of Engineering and Management

Air Force Institute of Technology

Air University

Air Education and Training Command

In Partial Fulfillment of the Requirements for the  
Degree of Master of Science in Astronautical Engineering

Daniel M. Jensen, BS

1<sup>st</sup> Lieutenant, USAF

March 2005

APPROVED FOR PUBLIC RELEASE; DISTRIBUTION UNLIMITED

AFIT/GA/ENY/05-M06

**BIAXIAL FATIGUE BEHAVIOR OF NiTi SHAPE MEMORY ALLOY**

Daniel M. Jensen, BS

1<sup>st</sup> Lieutenant, USAF

Approved:

/SIGNED/ _____ Marina Ruggles-Wrenn, PhD, (Chairperson)	9 March 2005 _____ Date
/SIGNED/ _____ Shankar Mall, PhD, (Member)	8 March 2005 _____ Date
/SIGNED/ _____ Robert Canfield, PhD, (Member)	9 March 2005 _____ Date

### **Abstract**

Nitinol is a shape memory alloy (SMA) capable of martensite-to-austenite phase transformations enabling shape-memory behavior. Shape-memory properties make Nitinol a strong candidate material for use in aircraft applications such as actuators. Structural integrity and reliability of torque tube actuators must be assured before this material can be used in flight-critical components. Thorough understanding of the fatigue response of the material is essential for a structurally-sound SMA actuator design.

The present effort investigates pure torsion and combined tension-torsion fatigue behavior of Nitinol at room temperature. Monotonic tests in tension and torsion were conducted to typify uni-directional stress-strain behavior. Fully-reversed torsion fatigue tests were conducted with shear stress ranges of 416, 584, 674, and 1310 MPa. In fully-reversed biaxial fatigue tests, a shear stress range of 500 MPa was superimposed on the axial stress ranges of 250, 500, 1000, 1120, and 1500 MPa. Fatigue behavioral characteristics, including fatigue S-N curves were established. Fatigue lives obtained in torsion-dominated biaxial tests were similar to those obtained in pure torsion. Conversely, tension-dominated biaxial fatigue was significantly more damaging, resulting in decreased fatigue lives. Applicability of von Mises criterion to correlating uniaxial and biaxial test results was examined. Evolution of stress-strain behavior with cycling is discussed.

AFIT/GA/ENY/05-M06

*To My Wife*

## Acknowledgments

First and foremost, I would like to express my deep gratitude and appreciation to my wife, thank you for tolerating the long hours and for making this possible. I would like to express my sincere appreciation to my faculty advisor, Dr. Marina B. Ruggles-Wrenn, for her guidance and support throughout the course of this thesis effort. The insight and experience was certainly appreciated. Special recognition is also sent to Dr. M. Taya from the University of Washington for supplying the material to be tested. I would also like to thank my sponsor, Dr. Brian Sanders of the Air Force Research Laboratories Air Vehicles Directorate for both the support and latitude provided to me in this endeavor.

Daniel M. Jensen

**This Note is not to be included with the Acknowledgments – it is for information only: *It is prohibited to include any personal information in the following categories about U.S. citizens, DOD Employees and military personnel: social security account numbers; home addresses; dates of birth; telephone numbers other than duty officers which are appropriately made available to the general public; names, locations and any other identifying information about family members of DOD employees and military personnel.***



## Table of Contents

	Page
Abstract.....	iv
Acknowledgments.....	vi
Table of Contents.....	vii
List of Figures.....	ix
List of Tables.....	xvi
I. Introduction and Background.....	1-1
II. Experimental Arrangements.....	2-1
2.1 Material and Specimen.....	2-1
2.2 Test Equipment.....	2-2
2.2.1 Biaxial Testing System.....	2-2
2.2.2 Microstructural Characterization.....	2-4
2.3 Mechanical Test Procedures.....	2-4
2.3.1 Monotonic Tests.....	2-4
2.3.1.1 Monotonic Tension to Failure.....	2-4
2.3.1.2 Monotonic Test in Pure Torsion.....	2-5
2.3.2 Cyclic Tests.....	2-7
2.3.2.1 Cyclic Test in Pure Torsion.....	2-8
2.3.2.2 Cyclic Tests in Combined Tension-Torsion.....	2-9
2.4 Post Failure Analysis.....	2-9
III. Results and Discussion.....	3-1
3.1 Monotonic Tension.....	3-1
3.2 Monotonic Torsion.....	3-2
3.3 Cyclic Tests in Pure Torsion.....	3-3
3.3.1 Torsion Fatigue with the 1310 MPa Shear Stress Range.....	3-5
3.3.2 Torsion Fatigue with the 674 MPa Shear Stress Range.....	3-7
3.3.3 Torsion Fatigue with the 576 MPa Shear Stress Range.....	3-10
3.3.4 Torsion Fatigue with the 416 MPa Shear Stress Range.....	3-13
3.3.5 Evolution of Engineering Shear Strain Range in Torsion Fatigue.....	3-15
3.4 Combined Tension-Torsion Fatigue Tests.....	3-16
3.4.1 Combined Tension-Torsion Fatigue, Axial Stress Range = 1480 MPa, Shear Stress Range = 500 MPa.....	3-18
3.4.2 Combined Tension-Torsion Fatigue, Axial Stress Range = 1120 MPa, Shear Stress Range = 500 MPa.....	3-23
3.4.3 Combined Tension-Torsion Fatigue, Axial Stress Range = 1000 MPa, Shear Stress Range = 500 MPa.....	3-29

3.4.4 Combined Tension-Torsion Fatigue, Axial Stress Range = 500 MPa, Shear Stress Range = 500 MPa .....	3-34
3.4.5 Combined Tension-Torsion Fatigue, Axial Stress Range = 250 MPa, Shear Stress Range = 500 MPa .....	3-40
3.4.6 Evolution of Axial Strain Range, Shear Strain Range, and Effective Strain Range in Combined Tension-Torsion Fatigue .....	3-46
3.4.7 Comparison of Effective Strain Range Evolution in Pure Torsion Fatigue and in Combined Tension-Torsion Fatigue .....	3-48
3.5 Post-Failure Analysis.....	3-50
3.5.1 Tensile Failure of NiTi SMA .....	3-51
3.5.2 Failure of NiTi in Torsion Fatigue .....	3-53
3.5.3 Cyclic Bi-axial Failure .....	3-57
 IV. Conclusions and Recommendations.....	 4-1
Bibliography .....	BIB-1
Vita .....	VITA-1

## List of Figures

	Page
Figure 2-1. Thin-Walled Tubular Test Specimen. Drawing not to scale.....	2-1
Figure 2-2. MTS 809 Axial-Torsional Testing System .....	2-2
Figure 2-3. Split Collar Inserts.....	2-3
Figure 3-1. Tensile Stress-Strain Curve.....	3-1
Figure 3-2. Shear Stress-Engineering Shear Strain Curve.....	3-2
Figure 3-3. Monotonic Tension and Monotonic Torsion Stress-Strain Curves in von Mises Effective Stress and Effective Strain Space .....	3-3
Figure 3-4. S-N Curve for Pure Torsion, Cyclic, Fully-Reversed Tests .....	3-4
Figure 3-5. Hysteresis loop evolution in torsion fatigue test with a shear stress range of 1310 MPa. Hysteresis loops for increasing cycles are offset to the right to show changes in shape of loops. ....	3-5
Figure 3-6. Shear stress-strain curves obtained in selected cycles of a torsion fatigue test with the shear stress range of 1310 MPa. ....	3-6
Figure 3-7. Evolution of maximum and minimum engineering shear strain with cycles in torsion fatigue test with the shear stress range of 1310 MPa.....	3-7
Figure 3-8. Hysteresis loop evolution in torsion fatigue test with a shear stress range of 674 MPa. Hysteresis loops for increasing cycles are offset to the right to show changes in shape of loops. ....	3-8
Figure 3-9. Shear stress-strain curves obtained in selected cycles of a torsion fatigue test with the shear stress range of 674 MPa. ....	3-9
Figure 3-10. Evolution of maximum and minimum engineering shear strain with cycles in torsion fatigue test with the shear stress range of 674 MPa.....	3-10
Figure 3-11. Hysteresis loop evolution in torsion fatigue test with a shear stress range of 576 MPa. Hysteresis loops for increasing cycles are offset to the right to show changes in shape of loops. ....	3-11

Figure 3-12. Shear stress-strain curves obtained in selected cycles of a torsion fatigue test with the shear stress range of 576 MPa. ....	3-12
Figure 3-13. Evolution of maximum and minimum engineering shear strain with cycles in torsion fatigue test with the shear stress range of 576 MPa.....	3-12
Figure 3-14. Hysteresis loop evolution in torsion fatigue test with a shear stress range of 416 MPa. Hysteresis loops for increasing cycles are offset to the right to show changes in shape of loops. ....	3-13
Figure 3-15. Shear stress-strain curves obtained in selected cycles of a torsion fatigue test with the shear stress range of 416 MPa. ....	3-14
Figure 3-16. Evolution of maximum and minimum engineering shear strain with cycles in torsion fatigue test with the shear stress range of 416 MPa.....	3-15
Figure 3-17. Shear strain range as a function of fatigue cycles.....	3-16
Figure 3-18. Effective Stress Range Versus Fatigue Life.....	3-17
Figure 3-19. Evolution of axial hysteresis loop in combined tension-torsion fatigue with axial stress range of 1480 MPa and shear stress range of 500 MPa. Hysteresis loops for increasing cycles are offset to the right to show changes in shape of loops. ....	3-19
Figure 3-20. Axial stress-strain curves obtained in combined tension-torsion with axial stress range of 1480 MPa and shear stress range of 500 MPa. ....	3-19
Figure 3-21. Shear stress-strain hysteresis loops obtained in combined tension-torsion fatigue test with an axial stress range of 1480 MPa and a shear stress range of 500 MPa. Hysteresis loops for increasing cycles are offset to the right to show changes in shape of loops.....	3-20
Figure 3-22. Shear stress-shear curves obtained in combined tension-torsion with axial stress range of 1480 MPa and shear stress range of 500 MPa.....	3-20
Figure 3-23. Effective stress-strain hysteresis loops obtained in combined tension-torsion fatigue test with an axial stress range of 1480 MPa and a shear stress range of 500 MPa. Hysteresis loops for increasing cycles are offset to the right to show changes in shape of loops.....	3-21
Figure 3-24. Effective stress-strain curves obtained in combined tension-torsion with axial stress range of 1480 MPa and shear stress range of 500 MPa. ....	3-22

Figure 3-25. Evolution maximum and minimum axial strain, shear strain, and effective strain with fatigue cycles in a fatigue test with axial stress range of 1480 MPa and shear stress range of 500 MPa.....	3-23
Figure 3-26. Axial stress-strain hysteresis loops obtained in combined tension-torsion fatigue test with an axial stress range of 1120 MPa and a shear stress range of 500 MPa. Hysteresis loops for increasing cycles are offset to the right to show changes in shape of loops.....	3-24
Figure 3-27. Axial stress-strain curves obtained in combined tension-torsion with axial stress range of 1120 MPa and shear stress range of 500 MPa.....	3-25
Figure 3-28. Shear stress-strain hysteresis loops obtained in combined tension-torsion fatigue test with an axial stress range of 1120 MPa and a shear stress range of 500 MPa. Hysteresis loops for increasing cycles are offset to the right to show changes in shape of loops.....	3-25
Figure 3-29. Shear stress-strain curves obtained in combined tension-torsion with axial stress range of 1120 MPa and shear stress range of 500 MPa.....	3-26
Figure 3-30. Effective stress-strain hysteresis loops obtained in combined tension-torsion fatigue test with an axial stress range of 1120 MPa and a shear stress range of 500 MPa. Hysteresis loops for increasing cycles are offset to the right to show changes in shape of loops.....	3-27
Figure 3-31. Effective stress-strain curves obtained in combined tension-torsion with axial stress range of 1120 MPa and shear stress range of 500 MPa.....	3-27
Figure 3-32. Evolution maximum and minimum axial strain, shear strain, and effective strain with fatigue cycles in a fatigue test with axial stress range of 1120 MPa and shear stress range of 500 MPa.....	3-28
Figure 3-33. Axial stress-strain hysteresis loops obtained in combined tension-torsion fatigue test with an axial stress range of 1000 MPa and a shear stress range of 500 MPa. Hysteresis loops for increasing cycles are offset to the right to show changes in shape of loops.....	3-30
Figure 3-34. Axial stress-strain curves obtained in combined tension-torsion with axial stress range of 1000 MPa and shear stress range of 500 MPa.....	3-30
Figure 3-35. Shear stress-strain hysteresis loops obtained in combined tension-torsion fatigue test with an axial stress range of 1000 MPa and a shear stress range of 500 MPa. Hysteresis loops for increasing cycles are offset to the right to show changes in shape of loops.....	3-31

Figure 3-36. Shear stress-strain curves obtained in combined tension-torsion with axial stress range of 1000 MPa and shear stress range of 500 MPa. .... 3-31

Figure 3-37. Effective stress-strain hysteresis loops obtained in combined tension-torsion fatigue test with an axial stress range of 1000 MPa and a shear stress range of 500 MPa. Hysteresis loops for increasing cycles are offset to the right to show changes in shape of loops. .... 3-32

Figure 3-38. Effective stress-strain curves obtained in combined tension-torsion with axial stress range of 1000 MPa and shear stress range of 500 MPa. .... 3-33

Figure 3-39. Evolution maximum and minimum axial strain, shear strain, and effective strain with fatigue cycles in a fatigue test with axial stress range of 1000 MPa and shear stress range of 500 MPa. .... 3-33

Figure 3-40. Axial stress-strain hysteresis loops obtained in combined tension-torsion fatigue test with an axial stress range of 500 MPa and a shear stress range of 500 MPa. Hysteresis loops for increasing cycles are offset to the right to show changes in shape of loops. .... 3-35

Figure 3-41. Axial stress-strain curves obtained in combined tension-torsion with axial stress range of 500 MPa and shear stress range of 500 MPa. .... 3-35

Figure 3-42. Shear stress-strain hysteresis loops obtained in combined tension-torsion fatigue test with an axial stress range of 500 MPa and a shear stress range of 500 MPa. Hysteresis loops for increasing cycles are offset to the right to show changes in shape of loops. .... 3-36

Figure 3-43. Shear stress-strain curves obtained in combined tension-torsion with axial stress range of 500 MPa and shear stress range of 500 MPa. .... 3-36

Figure 3-44. Effective stress-strain hysteresis loops obtained in combined tension-torsion fatigue test with an axial stress range of 500 MPa and a shear stress range of 500 MPa. Hysteresis loops for increasing cycles are offset to the right to show changes in shape of loops. .... 3-37

Figure 3-45. Effective stress-strain curves obtained in combined tension-torsion with axial stress range of 500 MPa and shear stress range of 500 MPa. .... 3-38

Figure 3-46. Evolution maximum and minimum axial strain, shear strain, and effective strain with fatigue cycles in a fatigue test with axial stress range of 500 MPa and shear stress range of 500 MPa. .... 3-39

Figure 3-47. Axial stress-strain hysteresis loops obtained in combined tension-torsion fatigue test with an axial stress range of 250 MPa and a shear stress range of 500 MPa. Hysteresis loops for increasing cycles are offset to the right to show changes in shape of loops..... 3-41

Figure 3-48. Axial stress-strain curves obtained in combined tension-torsion with axial stress range of 250 MPa and shear stress range of 500 MPa. .... 3-41

Figure 3-49. Shear stress-strain hysteresis loops obtained in combined tension-torsion fatigue test with an axial stress range of 250 MPa and a shear stress range of 500 MPa. Hysteresis loops for increasing cycles are offset to the right to show changes in shape of loops..... 3-42

Figure 3-50. Shear stress-strain curves obtained in combined tension-torsion with axial stress range of 250 MPa and shear stress range of 500 MPa. .... 3-43

Figure 3-51. Shear stress-strain curves obtained in combined tension-torsion with axial stress range of 250 MPa and shear stress range of 500 MPa. Emphasis on cycle 5000 to cycle 10000. .... 3-43

Figure 3-52. Effective stress-strain hysteresis loops obtained in combined tension-torsion fatigue test with an axial stress range of 250 MPa and a shear stress range of 500 MPa. Hysteresis loops for increasing cycles are offset to the right to show changes in shape of loops..... 3-44

Figure 3-53. Effective stress-strain curves obtained in combined tension-torsion with axial stress range of 250 MPa and shear stress range of 500 MPa. .... 3-44

Figure 3-54. Evolution maximum and minimum axial strain, shear strain, and effective strain with fatigue cycles in a fatigue test with axial stress range of 250 MPa and shear stress range of 500 MPa..... 3-45

Figure 3-55. Biaxial fatigue axial strain range progression with select cycle count. .... 3-47

Figure 3-56. Biaxial fatigue torsional engineering shear strain range progression with select cycle count. .... 3-47

Figure 3-57. Biaxial fatigue effective strain range progression with select cycle count..... 3-48

Figure 3-58. Biaxial and torsional fatigue effective strain range progression with select cycle count, where Eff is effective stress, CL denotes biaxial fatigue, PT denotes torsion fatigue, and FL is short for Fatigue Life..... 3-49

Figure 3-59. Tensile Test Failure.....	3-52
Figure 3-60. Tensile Test Failure Close-up .....	3-52
Figure 3-61. Micrograph of tensile failure at 100x magnification (a) and 500x magnification (b). Loading Direction is perpendicular to image. The full width of the thin-walled tube is visible in A. ....	3-53
Figure 3-62. Pure Torsion 1310 MPa Shear Stress Range (2269 MPa Effective Stress Range) Failure.....	3-54
Figure 3-63. Pure Torsion 674 MPa Shear Stress Range (1167 MPa Effective Stress Range) Failure.....	3-55
Figure 3-64. Micrograph of cyclic torsion angled fracture at 100x (A) and 250x (B) magnification. The full width of the thin-walled tube is visible in 4.5-7a. The black arrows mark out V-shaped troughs meeting in the center of the thin-walled tube. ....	3-55
Figure 3-65. Micrograph of cyclic torsion parallel fracture at 100x (a) and 250x (b) magnification. The full width of the thin-walled tube is visible (a). The black arrows mark out circumferential troughs in the thin-walled tube.....	3-56
Figure 3-66. Pure Torsion 584 MPa Shear Stress Range (1012 MPa Effective Stress Range) Failure.....	3-56
Figure 3-67. Combined 1500 MPa Stress Range with 500 MPa Shear Stress Range Failure(1732 MPa Effective Stress Range).....	3-58
Figure 3-68. Combined 1120 MPa Stress Range with 500 MPa Shear Stress Range Failure (1416 MPa Effective Stress Range).....	3-59
Figure 3-69. Micrograph of combined tension-torsion cyclic fracture at 100x (a) and 500x (b) magnification. The full width of the thin-walled tube is visible in 4.5-10a. Arrows point out apparent trough flow away from the apex. ....	3-60
Figure 3-70. Combined 1000 MPa Stress Range with 500 MPa Shear Stress Range Failure (1323 MPa Effective Stress Range).....	3-61
Figure 3-71. Combined 500 MPa Stress Range with 500 MPa Shear Stress Range Failure (1000 MPa Effective Stress Range).....	3-61
Figure 3-72. Combined 250 MPa stress range with 500 MPa shear stress range failure (901 MPa effective stress range). Micrograph locations are marked with arrows as well as the direction of the V-troughs on the fracture surface.....	3-63



Figure 3-73. Micrograph of combined tension-torsion 901 MPa effective stress range tensile-area fracture at 100x (a) and 250x (b) magnification. The full width of the thin-walled tube is visible in 3-72a. Arrows point out suggest trough direction ..... 3-63

Figure 3-74. Micrograph of combined tension-torsion 901 MPa effective stress range angled fracture surface at 100x (a) and 500x (b) magnification. The full width of the thin-walled tube is visible in 3-73a. Arrows point out apparent V-trough flow away from the tensile failure and towards the parallel fracture area. .... 3-64

Figure 3-75. Micrograph of combined tension-torsion 901 MPa effective stress range parallel fracture at 100x (a) and 500x (b) magnification. The full width of the thin-walled tube is visible in 3-74a. Arrows point out apparent parallel trough flow along the gage section ..... 3-64

Figure 3-76. Micrograph of combined tension-torsion 901 MPa effective stress range angle fracture away from parallel fracture at 100x (a) and 500x (b) magnification. The full width of the thin-walled tube is visible in 3-75a. Arrows point out apparent trough flow away from the parallel fracture section. .... 3-65

## List of Tables

	Page
Table 2-1 Summary of tests .....	2-7

# BIAXIAL FATIGUE BEHAVIOR OF NiTi SHAPE MEMORY ALLOY

## I. Introduction and Background

Shape memory refers to a material's ability to return to its original shape after experiencing large scale bending, stretching, twisting, compression, or some varied combination of these plastic deformation processes (6:2; 7). Shape memory alloys (SMAs) represent a class of materials capable of "remembering" a shape, even after severe deformations (7; 18). Once deformed at low temperatures (in their martensitic phase), SMAs will stay deformed until heated (to their austenitic phase), at which point they will return to their original pre-deformed shape. The basis for the memory effect is that these materials can easily transform to and from martensite. Nitinol is a solid-state, durable alloy capable of shape-memory behavior. None recover their original shape with higher efficiency than Nitinol (7; 16). In addition, Nitinol exhibits superelasticity with recoverable "elastic" strains of up to 8% at temperatures slightly above the austenite finish temperature (temperature at which reverse transformation to austenite is complete) (6:2; 7; 15; 16; 19; 24; 26; 28). The temperature at which recovery takes place is completely dependent upon material composition and annealing temperature (6; 8; 17).

Phenomenal shape memory effect of equiatomic NiTi was first revealed at the U.S. Naval Ordnance Laboratory (NOL) in 1963 and was brought into application in 1965 (6:2, 8:71, 16). Near equiatomic nickel-titanium shape memory alloy is also referred to as NiTi, TiNi, and Nitinol. Interestingly, the name "Nitinol" comes from combining the atomic symbols of nickel and titanium with the place of discovery, NOL

(6:1). The phenomenal shape recovery behavior of NiTi is limited to NiTi alloys having near equiatomic composition (6:1).

Because of its shape-memory, superelastic, and biocompatible properties, Nitinol is an ideal candidate for many applications including actuators, pipe connectors, and various biotechnology devices including eye-glass frames, braces, and most importantly, endovascular stents (15; 16; 25; 26; 28). The fact that Nitinol is largely unaffected by environment makes aerospace applications including deformable wings and SMA rotorcraft actuators possible (9; 10; 11; 14).

As one could imagine, a great number of research efforts involving NiTi has centered on optimizing the shape memory and super elastic effect by perfecting alloy percentages and ideal annealing temperatures (6,21,29). Given that multitudes of applications involve cyclic loading and that cyclic fatigue represents a prime mechanism of failure, the comparative lack of published information on Nitinol fatigue resistance is quite alarming (13; 15). The sparse fatigue studies that have been reported have focused on uniaxial tension fatigue (13; 19). Torsional fatigue data is even more sparse (11). Moreover, the majority of cyclic tests reported in literature were performed on wires, where macro scale geometric effects cannot be utilized, determined, or benefited from (8; 17; 19; 20; 21; 22; 27; 28; 29; 30). For example, thin-walled, torque tube actuators hold more promise than solid rods due to savings in weight and larger torque outputs (10). To insure safe and reliable utilization of this material in future applications, multiaxial as well as uniaxial fatigue behavior must be examined (11; 16).

The present study focuses on torsion and biaxial tension-torsion fatigue behavior of NiTi shape memory alloy at room temperature. Monotonic tests in tension and torsion were conducted to typify uni-directional stress-strain behavior. Fully-reversed torsion fatigue tests were conducted with shear stress ranges of 416, 584, 674, and 1310 MPa. In fully-reversed biaxial fatigue tests, a shear stress range of 500 MPa was superimposed on the axial stress ranges of 250, 500, 1000, 1120, and 1500 MPa. Fatigue behavioral characteristics, including fatigue S-N curves were established. Detailed observations on the evolution of mechanical behavior with cycling are provided to guide development of experiment-based constitutive and life-prediction models. Applicability of von Mises criterion to correlating uniaxial and biaxial test results is also examined. Evolution of stress-strain behavior with cycling is discussed. The research effort finishes with a brief discussion and characterization of fracture surfaces produced in monotonic tension, cyclic pure torsion, tension-dominant biaxial fatigue, and torsion-dominant biaxial fatigue.

Test material, specimen, and experimental arrangements are described in chapter 2. Chapter 3 is dedicated to the presentation and discussion of the results and observations. Finally, concluding remarks and recommendations for further research are offered in chapter 4.

## II. Experimental Arrangements

Experimental arrangements chapter describes how the Nitinol specimens were manufactured, processed, and annealed. The testing equipment used to conduct this research program is then explained. Following that, the test procedures utilized are listed. The chapter ends with a discussion of post-failure analysis.

### 2.1 Material and Specimen

The specimens for study were provided by Dr. M. Taya of the University of Washington. Details of material processing and heat treatment are found in reference 7. Test material was near equiatomic Nickel-Titanium supplied in 8-in. diameter ingots (Titanium-49.9 atomic% Nickel) (7). Forged NiTi formed 2.5-in. diameter billets that were then hot rolled into 0.55-in. nominal diameter rods at 900°C (7). This process has been known to produce a fine grain size (~ASTM 6) (7). The rods were then solution annealed in air at 85°C for 20 minutes followed by a water quench (7). The rods were next drawn at room temperature to contain approximately 30% cold work (7). Finally cylindrical dog bone specimens were machined according to specifications in figure 2-1 (4; 7).

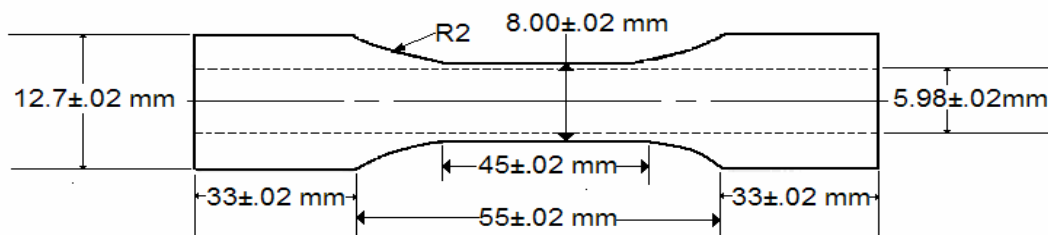


Figure 2-1. Thin-Walled Tubular Test Specimen. Drawing not to scale.

After machining, the thin-walled tubular dog-bone specimens were heat annealed at 475°C for 5 minutes in salt baths followed by a water quench (7).

## 2.2 Test Equipment

### 2.2.1 Biaxial Testing System

All tests were performed at room temperature nominally 23°C in laboratory air environment. A servo controlled MTS 809 Axial-Torsional Testing System (figure 2-2) together with an MTS TestStar IIm digital controller utilizing TestStar IIm station manager software (version 3.4B 1459) was used for computerized testing and data acquisition.

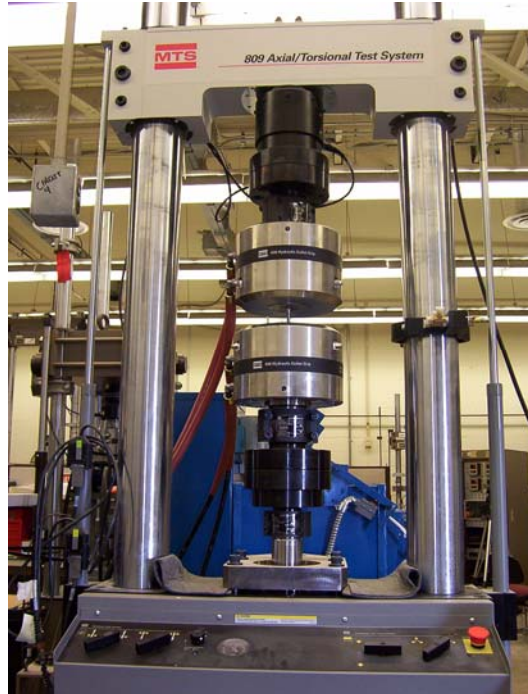


Figure 2-2. MTS 809 Axial-Torsional Testing System

Values recorded by the Teststar IIm software include time, cycle number (for cyclic tests), axial displacement, axial force command, axial force, torque, and angle of rotation. The data acquisition interval was set at 100 Hz for the monotonic tests. During cyclic testing, a data acquisition rate of 20Hz was utilized for the first 50 cycles and then again for every subsequent 50<sup>th</sup> cycle (cycles 1-50, 100, 150, etc). Peak-valley data was also recorded for all fatigue cycles. Complete digital data for every test is available for analysis. MTS 646 Hydraulic Collet Grips (model #646.25s) with an axial capacity of 250 kN and torsional capacity of 2200 N-m combined and split collar inserts (See Fig 2-3) permitted uniaxial and biaxial testing in load/control. Grip pressure of 3.5 MPa was used in all tests.

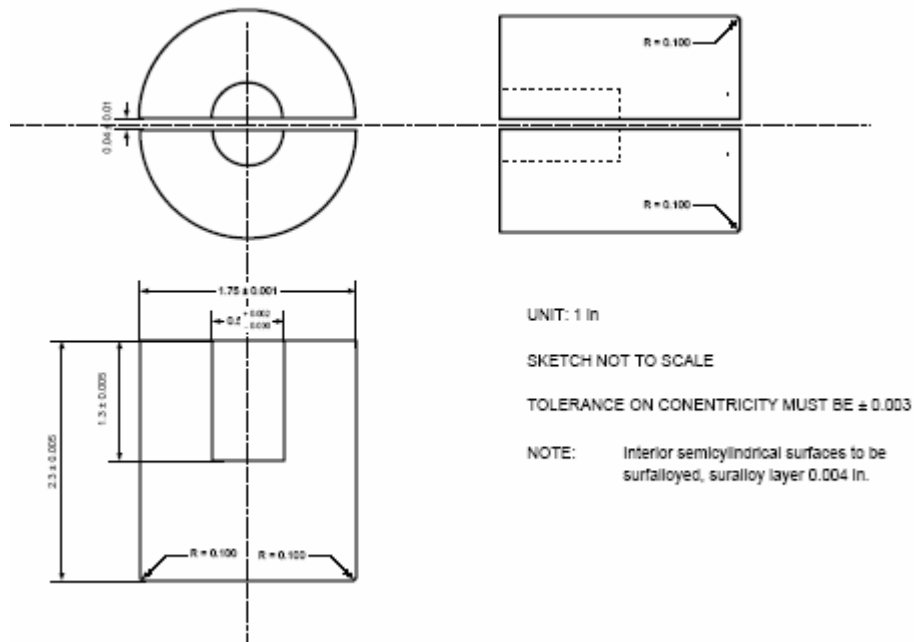


Figure 2-3. Split Collar Inserts

One thermocouple was attached to the middle of the specimen gage section. Thermocouple data was recorded manually during tests. Specimen temperature remained



below 43°C (110°F), much lower than the temperature required to trigger a thermal martensite to austenite phase change (19, 29) in NiTi SMA.

## **2.2.2 Microstructural Characterization**

Fracture surfaces produced in tension, torsion, or combination tension-torsion tests were examined ZEISS Stemi SVII optical microscope and a Quanta 200HV scanning electron microscope (SEM).

## **2.3 Mechanical Test Procedures**

Eleven Nickel-Titanium specimens were tested in this study. Two specimens were subjected to monotonic loading, one to tension to failure, and another to torsion. Four specimens were subjected to fatigue tests in pure torsion. Five specimens were subjected to combined tension-torsion fatigue tests.

### **2.3.1 Monotonic Tests**

#### **2.3.1.1 Monotonic Tension to Failure**

One specimen was subjected to load-controlled monotonic tension to failure. Angle of rotation was held at zero during the test. The purpose of this test was to establish the axial stress-strain curve of Nickel-Titanium and to determine the modulus of elasticity (E), the yield strength ( $\sigma_y$ ), and the Ultimate Tensile Strength (UTS) (2,3).

In all tests, axial load values recorded during the test were used to calculate axial engineering stresses. Conversion from axial load to stress was done by the standard method:

$$\sigma = \frac{P}{A} \quad (1)$$

where

$\sigma =$  Axial Stress (MPa)

$P =$  Axial Force (N)

$A =$  Cross-Sectional Gage Area (m<sup>2</sup>)

Axial engineering stress will be referred to as axial stress for the remainder of this paper.

In all tests, axial displacement recorded during the test was used to calculate strain. Conversion from axial displacement to strain was done by the standard method:

$$\varepsilon = \frac{\Delta L}{L_0} \quad (2)$$

where

$\varepsilon =$  Axial Engineering Strain (MPa)

$\Delta L =$  Axial Change in Length (m)

$L_0 =$  Original Distance Between the Grips (m)

The specimen was loaded at a rate of 304 N/s.

### **2.3.1.2 Monotonic Test in Pure Torsion**

One specimen was subjected to monotonic torsion in torque control. Axial displacement was held at zero. The purpose of this test was to investigate the shear

stress-engineering shear strain relationship of Nitinol and to determine the shear modulus (G) and the yield strength in shear ( $\tau_y$ ) (1).

In pure torsion tests, torque recorded during the test was used to calculate engineering shear stresses. Conversion from torque to engineering shear stress was done by standard methods.

$$\tau = \frac{T \cdot C_2}{J} \quad (3)$$

where

$\tau =$  *Engineering Shear Stress* (MPa)

$T =$  *Torque* (N-m)

$C_2 =$  *Outer Radius of the Gage Section* (m)

$J =$  *Polar Moment of Inertia* (m<sup>4</sup>)

The Polar Moment of Inertia is calculated as:

$$J = \frac{\pi}{2} (C_2^4 - C_1^4) \quad (4)$$

where

$C_1 =$  *Inner Radius of the Gage Section* (m)

Engineering shear strain was calculated directly from angle of rotation:

$$\gamma = \frac{\phi \cdot C_2}{L_0} \quad (5)$$

where

$\gamma =$  *Torsional Engineering Shear Strain* (mm/mm)

$\phi =$  *Angle of Rotation* (rad)

The specimen was tested in torque control at a rate of 8MPa/s. Note that the shear stress rate of 8 MPa/s is equivalent, in the von Mises sense, to the axial stress rate of 13.86 MPa/s used in monotonic tensile test. Once the maximum angle of rotation of the test machine was reached, the specimen was unloaded to zero torque in 5 seconds, the test paused, bottom of the specimen ungripped, and the lower grip repositioned. The test was resumed after the lower grip had been repositioned and the distance between the grips had been measured. The test was stopped after excessive deformation in the specimen.

### 2.3.2 Cyclic Tests

The fatigue tests conducted in the present effort are summarized in table 2-1 where axial stress range,  $\Delta\sigma$ , shear stress range,  $\Delta\tau$ , and von Mises effective stress range,  $\Delta\sigma_{\text{eff}}$ , together with the number of cycles to failure are given for each specimen. Fully-reversed fatigue tests with an R ratio (minimum stress divided by maximum stress) of -1 were performed at a frequency of 0.1 Hz.

Table 2-1 Summary of tests

AXIAL STRESS RANGE, $\Delta\sigma$ (MPa)	SHEAR STRESS RANGE, $\Delta\tau$ (MPa)	EFFECTIVE STRESS RANGE, $\Delta\sigma_{\text{eff}}$ (MPa)	CYCLES TO FAILURE
<b>PURE TORSION FATIGUE</b>			
N/A	1310	2269	244
N/A	674	1167	4219
N/A	584	1012	27789
N/A	416	721	100000
<b>COMBINED TENSION-TORSION FATIGUE</b>			
1500	500	1732	9
1120	500	1416	43
1000	500	1323	4164
500	500	1000	11079
250	500	901	37018

The fatigue run-out was defined as survival of  $10^5$  cycles.

Cyclic tests were conducted in load control. Presentation of hysteresis loops is made without consideration of grip slippage or changes in specimen diameter.

### 2.3.2.1 Cyclic Test in Pure Torsion

Four specimens were subject to load-controlled, fully reversed cyclic loading at a frequency of 0.1Hz. The applied shear stress ranges were 416, 584, 674, and 1310 MPa. The run-out was defined as survival of  $10^5$  cycles. The axial channel was held at zero displacement. The purpose of these tests was to establish fatigue life as a function of shear stress range. In addition, these tests permitted investigation of the shear stress-shear strain behavior and the usefulness of von Mises effective stress (effective strain) in correlating experimental results. The von Mises effective, or equivalent, stress,  $\sigma_{eff}$ , and effective strain,  $\varepsilon_{eff}$ , are defined as:

$$\sigma_{eff} = \sqrt{\sigma^2 + 3\tau^2} \qquad \varepsilon_{eff} = \sqrt{\varepsilon^2 + \frac{1}{3}\cdot\gamma^2} \qquad (6)$$

Note that in graphs involving effective stress, the effective stress was plotted as negative where the axial stress was negative (compression) and positive when axial stress was positive (tension). The same convention was used for effective strain whereas the sign of the effective strain was modified to negative when the axial strain was negative and positive when the axial strain was positive.

### **2.3.2.2 Cyclic Tests in Combined Tension-Torsion**

Five specimens were tested under cyclic, in-phase, fully-reversed, load-controlled combined tension-torsion at a frequency of 0.1 Hz. The axial stress range of 1500, 1120, 1000, 500, and 250 MPa were each combined with a shear stress range of 500 MPa. The purpose of these tests was to establish the S-N curve of NiTi under combined tension-torsion cycling. These tests permitted investigation of not only the axial stress-strain relationship and the shear stress-engineering shear strain relationship, but also of the von Mises effective stress-effective strain relationship for NiTi under fully reversed combined tension-torsion cyclic loading.

### **2.4 Post Failure Analysis**

Specimen failure was characterized as tensile, torsion fatigue, torsion-dominant biaxial fatigue, or tension-dominant biaxial fatigue and documented with photographs and SEM micrographs where applicable.

### III. Results and Discussion

#### 3.1 Monotonic Tension

The monotonic tensile test to failure was conducted in load control with the rate of 13.86 MPa/s. The axial stress-strain curve is presented in figure 3-1.

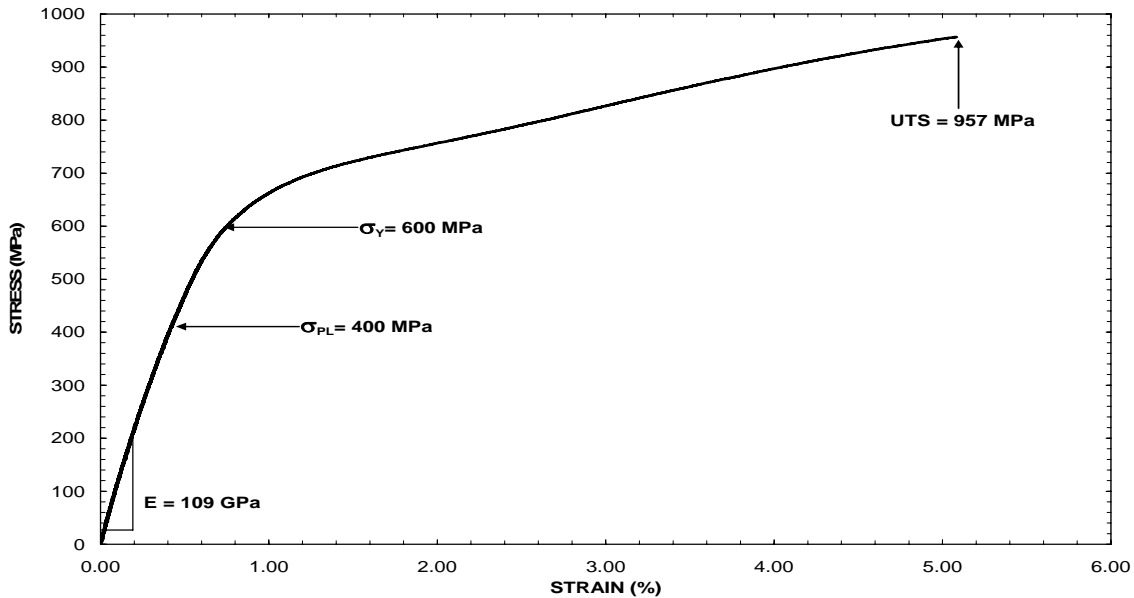


Figure 3-1. Tensile Stress-Strain Curve

The yield stress,  $\sigma_y$ , is 600 MPa and was determined using a 0.20% offset method. The initial departure from linearity, the proportional limit,  $\sigma_{PL}$ , occurs approximately ~400 MPa. The “knee” of the stress-strain curve extends to approximately ~700 MPa (corresponding strain of 1.30%), at which point the stress-strain curve appearance is akin to that typical for plastic flow with strain hardening. The ultimate tensile strength (UTS) was 957 MPa, fracture strain was 5.08%. It should be noted that failure stress level was equal to UTS. The stress-strain behavior obtained here was qualitatively similar to that reported in literature (15, 18). Young’s modulus,  $E$ , was calculated to be 109 GPa (3).

### 3.2 Monotonic Torsion

The monotonic torsion test results are presented in figure 3-2. The yield stress in shear stress,  $\tau_Y$ , of NiTi was 228 MPa using a 0.20% engineering shear strain offset method. The shear modulus,  $G$ , was 29 GPa (1). The test was terminated at the maximum shear stress of 847 MPa due to excessive deformation of the specimen.

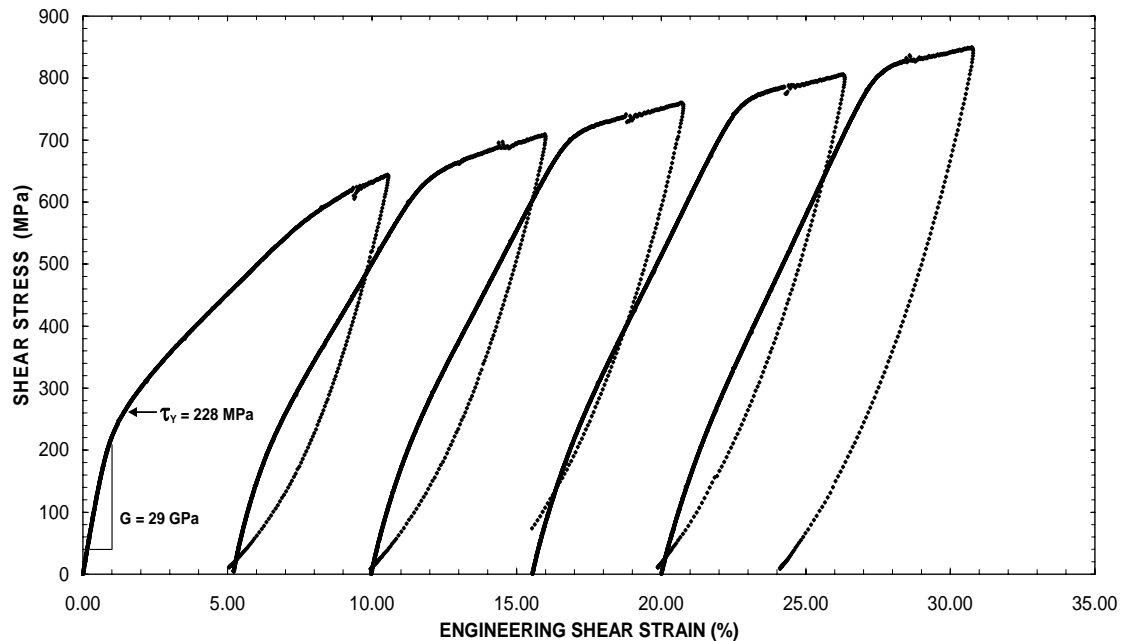


Figure 3-2. Shear Stress-Engineering Shear Strain Curve

The shear stress-engineering shear strain curve can be divided into three separate regions. The first region is the proportional yielding. After the yield stress was reached, more pliable linear deformation is noted along with slight plastic deformation as shear stress increases from 28 to ~600 MPa. In the third region, the stress-strain behavior is best described as plastic flow with hardening. All three regions are visible in figure 3-2.

Effective stress-strain diagrams for both monotonic uniaxial tests are displayed in figure 3-3. It is noteworthy that the stress-strain curve obtained in pure torsion departs



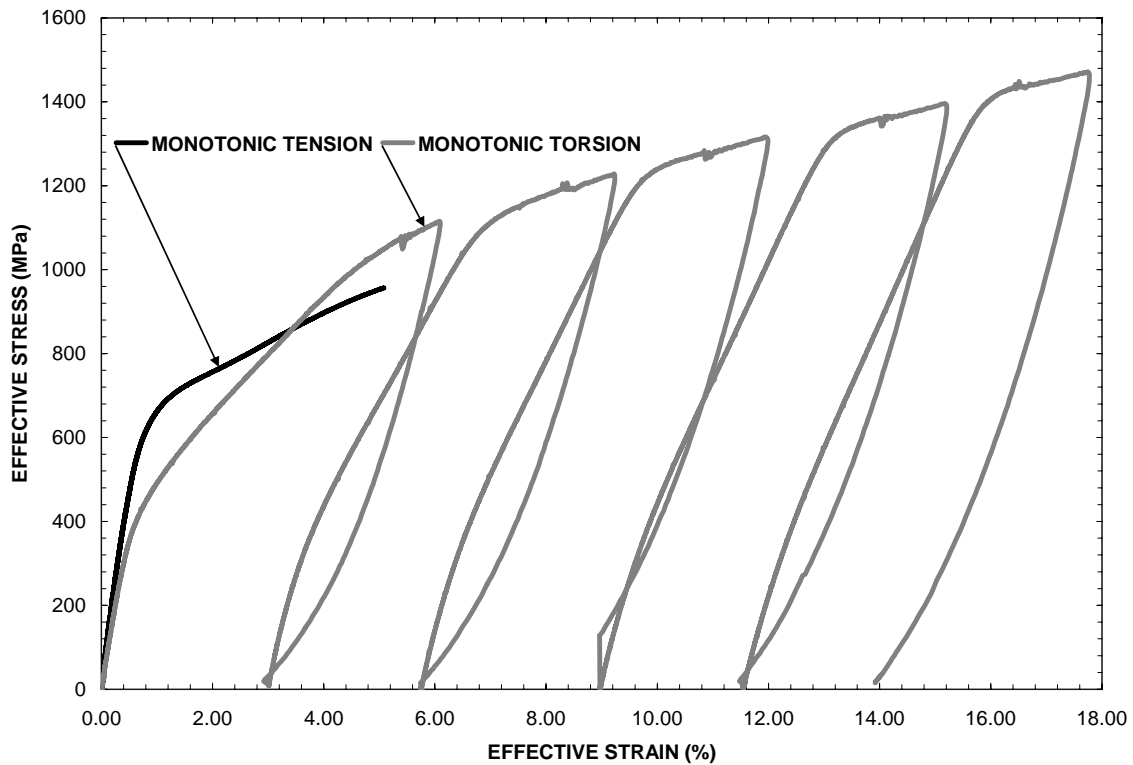


Figure 3-3. Monotonic Tension and Monotonic Torsion Stress-Strain Curves in von Mises Effective Stress and Effective Strain Space

from linearity at a much lower effective stress (395 MPa) than the stress-strain curve obtained in tension (600 MPa). Failure strain in tension was 5.08%. This contrasts with monotonic torsion where NiTi produced engineering shear strains in excess of 30%. Effective strain at failure produced in tension was 5.08%, while effective strain achieved in torsion was three and half times greater, 17.32%. Furthermore, NiTi achieves greater effective stress levels in torsion than in tension.

### 3.3 Cyclic Tests in Pure Torsion

Figure 3-4 presents the S-N curve established for pure torsion fatigue. It is important to note that the specimen tested with the shear stress range of 416 MPa

achieved a run-out (defined as surviving  $10^5$  cycles). Based on the adopted definition of fatigue run-out, the shear stress range endurance limit for equiatomic NiTi is estimated to be above 416 MPa

Results in figure 3-4 demonstrate that relationships between the shear stress range and number of cycles to failure can be represented by a power law:

$$N = 1.3722 \left( \frac{1}{\Delta\tau} \right)^{5.6306} \quad (7)$$

where

$N = \text{Number of Cycles to Failure}$

$\Delta\tau = \text{Shear Stress Range}$

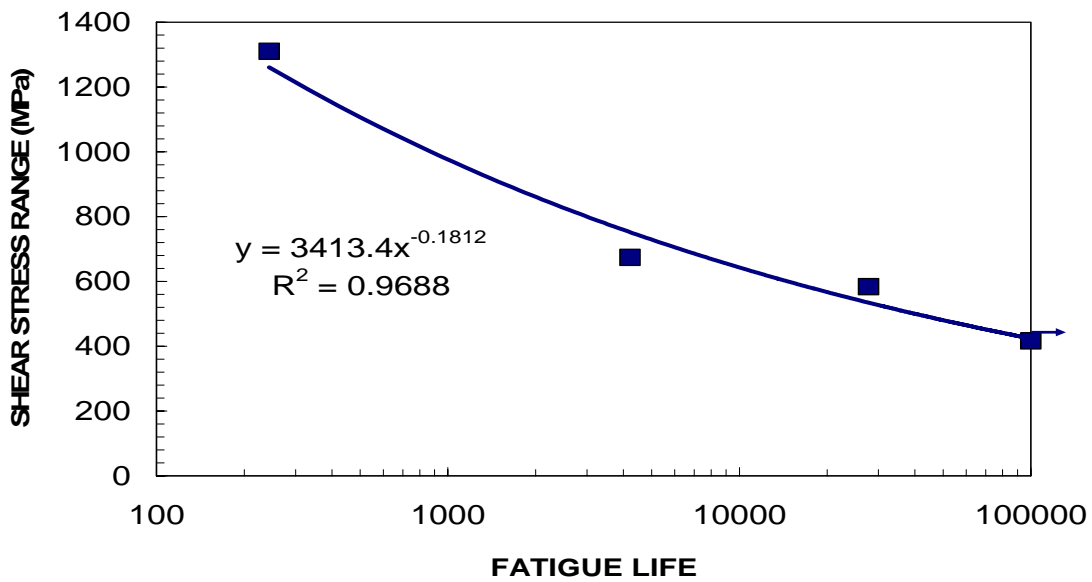


Figure 3-4. S-N Curve for Pure Torsion, Cyclic, Fully-Reversed Tests

Further understanding of the cyclic stress-strain behavior can be obtained through examination of the hysteresis loops produced during the test.

### 3.3.1 Torsion Fatigue with the 1310 MPa Shear Stress Range

Asymmetric loops, generated in fatigue test with the shear stress range of 1310 MPa are shown in figure 3-5. It is seen in figure 3-6 that the loops widen slightly as the cycling progresses. The engineering shear strain range increases from cycle 36 to cycle 236. The maximum engineering shear strain increases from 3.96% on cycle 36 to 4.36% on cycle 236, while the minimum engineering shear strain decreases from -4.86% on cycle 36 to -5.34% on cycle 236.

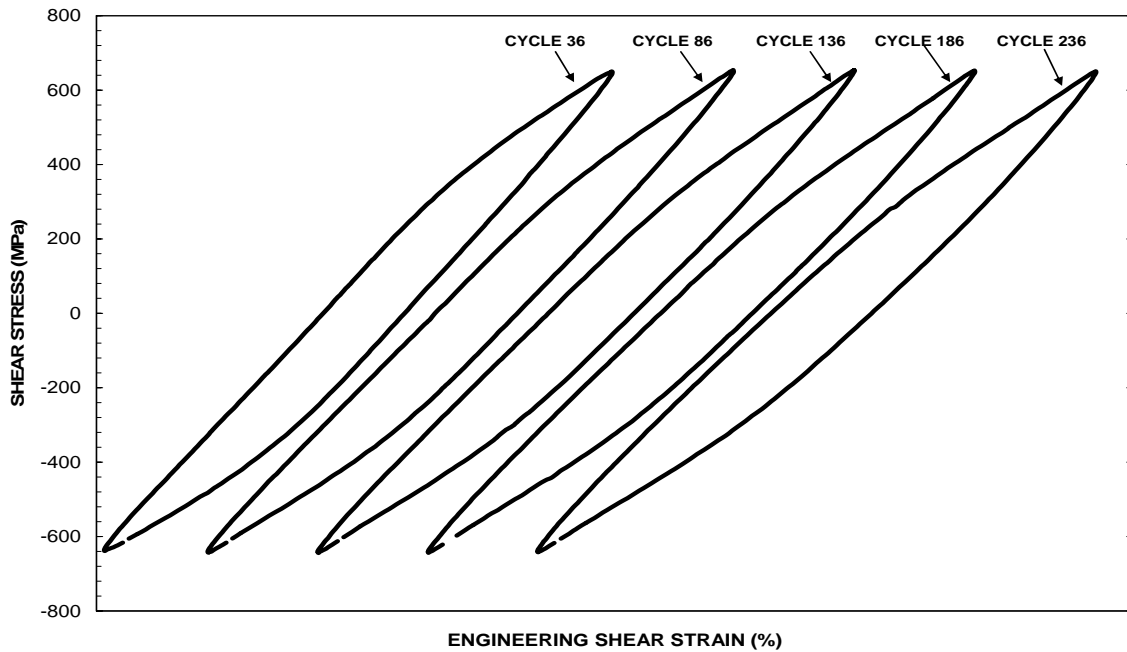


Figure 3-5. Hysteresis loop evolution in torsion fatigue test with a shear stress range of 1310 MPa. Hysteresis loops for increasing cycles are offset to the right to show changes in shape of loops.

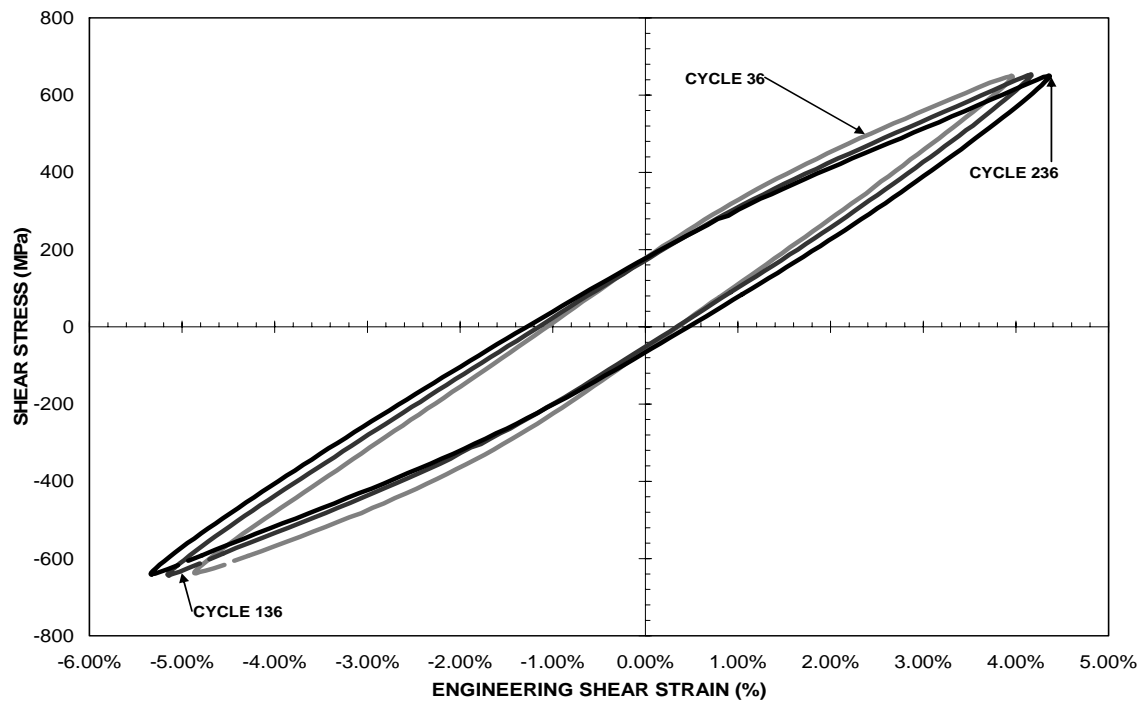


Figure 3-6. Shear stress-strain curves obtained in selected cycles of a torsion fatigue test with the shear stress range of 1310 MPa.

Maximum and minimum strains as functions of cycle number are seen in figure 3-7. The maximum engineering shear strain increases from 3.96% in cycle 1 to 4.30% in cycle 5 before stabilizing at 3.90% on cycle 20. After cycle 20, the maximum engineering shear strain per cycle increases to 4.37% on cycle 243 (the last complete cycle before failure).

The minimum engineering shear strain drops to -4.47% during the first 10 cycles before decreasing to -5.35% at cycle 243 before failure. The engineering shear strain range,  $\Delta\gamma$ , decreases in the first 20 cycles reaching a minimum of 8.57%, which indicates slight cyclic hardening. Increase in strain range and slight cyclic softening are observed during the remainder of cyclic life. The engineering shear stress range was 9.72% at cycle 243 shortly before failure.

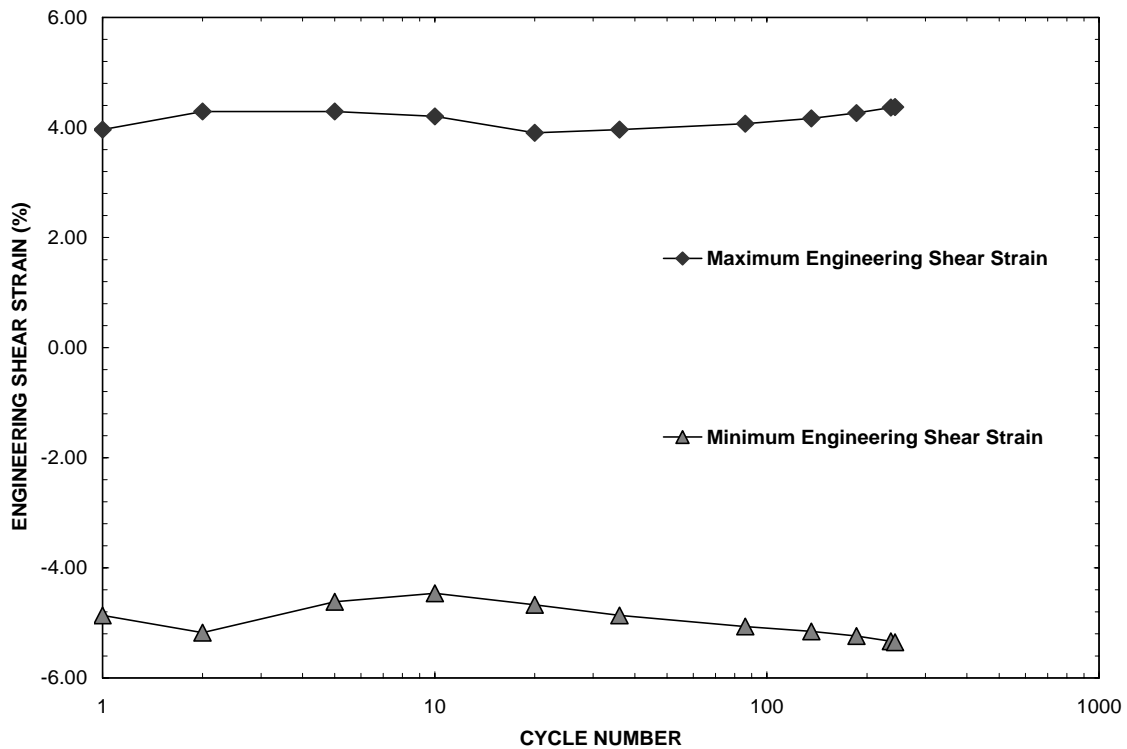


Figure 3-7. Evolution of maximum and minimum engineering shear strain with cycles in torsion fatigue test with the shear stress range of 1310 MPa.

### 3.3.2 Torsion Fatigue with the 674 MPa Shear Stress Range

Cyclic hysteresis loops obtained in torsion fatigue test with the shear stress range of 674 MPa are shown in figure 3-8. The ‘plastic’ engineering shear strain per cycle,  $\Delta\gamma_p$ , defined as the total width of the stress-strain hysteresis loop at zero stress (17) decreases through the first 500 cycles, then increases through later cycles of the test. From cycles number 500 on, hysteresis loops display increased plastic deformation at lower shear stress levels. Finally, hysteresis loops develop sharp corners at maximum and minimum engineering shear stress levels, which become sharper with increasing cycle count.

Furthermore, the area enclosed by each loop decreases through the first 100 cycles, remains stable cycles 100 to 1000, and then increases from cycle 1000 to cycle

4200. Note that failure occurred at cycle 4219.

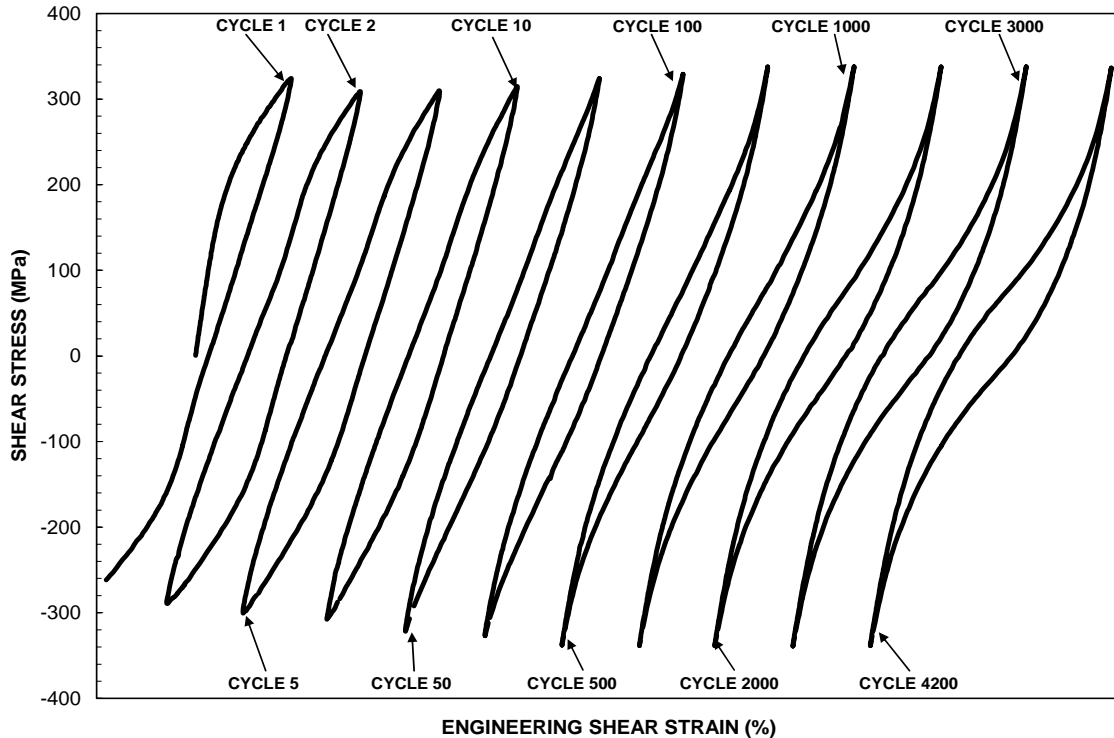


Figure 3-8. Hysteresis loop evolution in torsion fatigue test with a shear stress range of 674 MPa. Hysteresis loops for increasing cycles are offset to the right to show changes in shape of loops.

Figure 3-9 illustrates the changes in cyclic stress-strain behavior with continued cycling. Figure 3-9 clearly shows the ‘plastic’ strain per cycle,  $\Delta\gamma_p$ , changes with fatigue cycle count. Furthermore, it is seen that the stress-strain behavior becomes increasing asymmetric as the cycling progresses.

The progressions with increasing cycle count of the maximum and minimum shear strain are shown in figure 3-10. The maximum engineering shear strain decreases in the first 10 cycles, stabilizes at 2.23% for cycles 10 to 100, and then increases to 2.73% on cycle 4218 prior to failure. The minimum engineering shear strain remains

stable at  $-3.53\%$  during the first 10 cycles before continuously decreasing for cycles 10-4218 where it reaches  $-4.71\%$ .

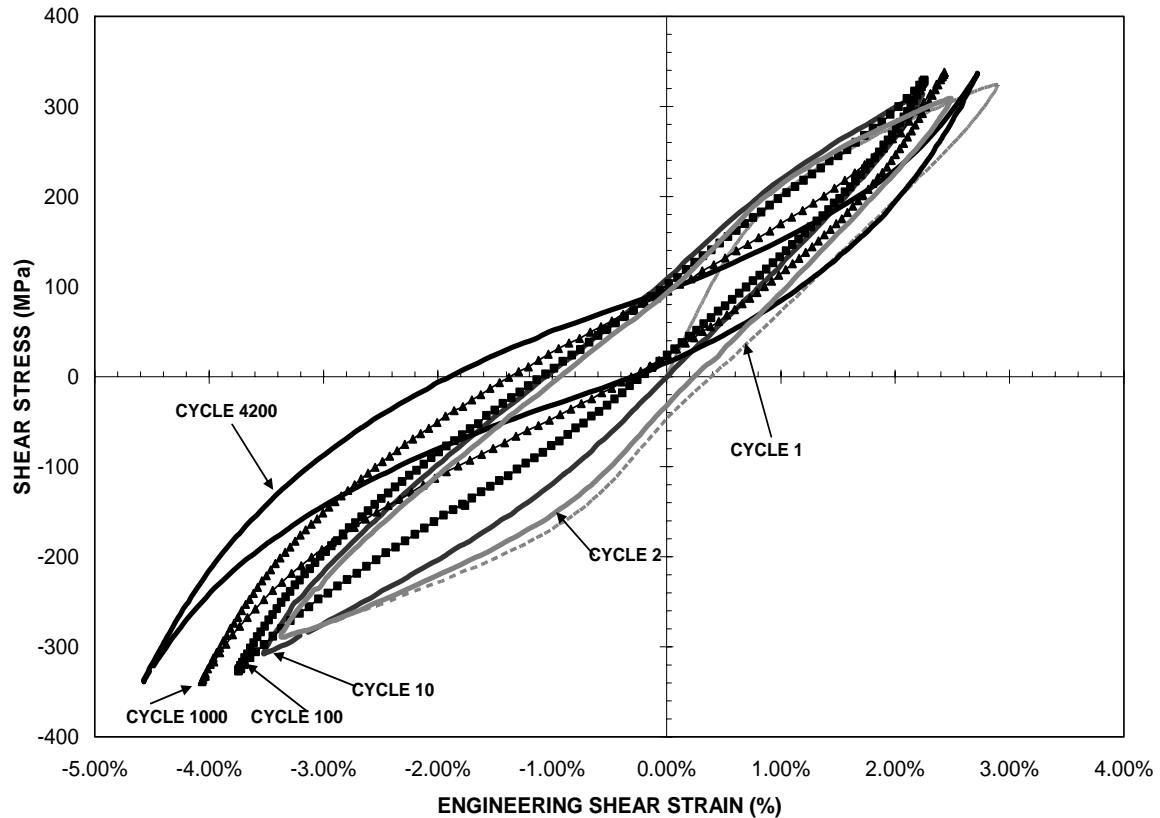


Figure 3-9. Shear stress-strain curves obtained in selected cycles of a torsion fatigue test with the shear stress range of 674 MPa.

A total decrease in minimum strain during cycles 2 to 4218 is 1.34%. Deformation behavior is not symmetric. Material behavior is cyclically neutral during the first 10 cycles, at which point it develops into cyclically softening. The shear strain range increases from 5.77% to 7.44% in the course of the cyclic life.

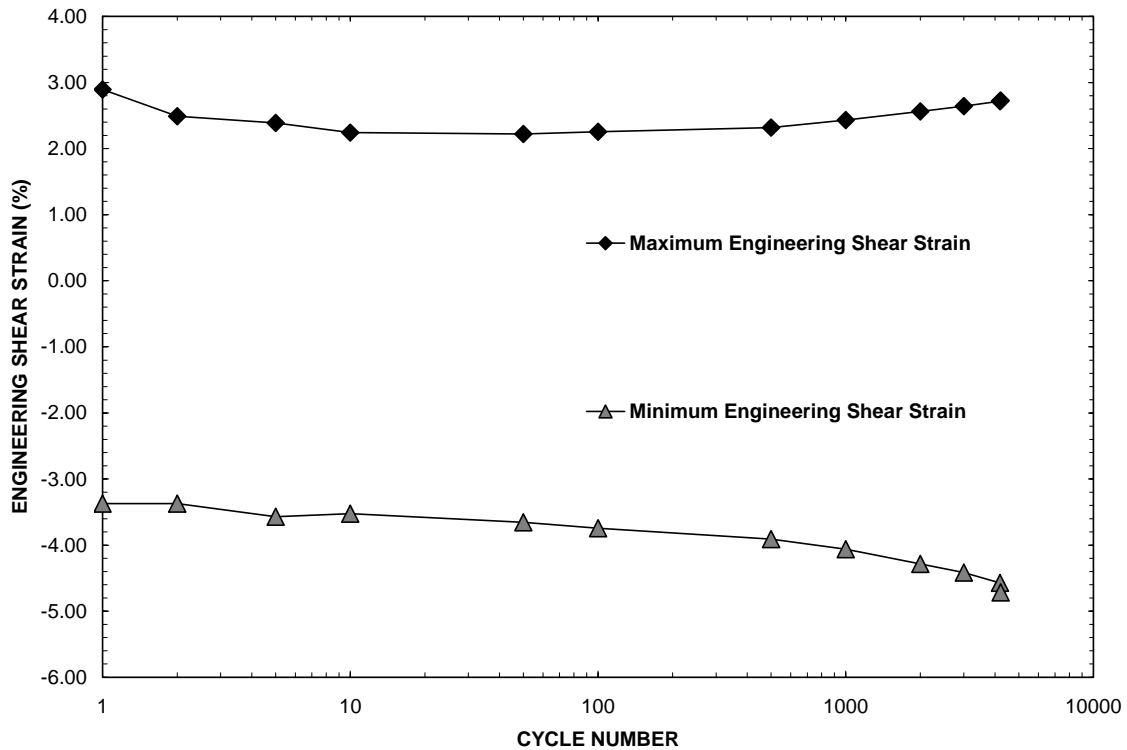


Figure 3-10. Evolution of maximum and minimum engineering shear strain with cycles in torsion fatigue test with the shear stress range of 674 MPa.

### 3.3.3 Torsion Fatigue with the 576 MPa Shear Stress Range

The pure torsion cyclic hysteresis loops obtained in torsion fatigue test with a shear stress range of 576 MPa are shown in figure 3-11. The shear strain range remains nearly constant throughout this test. The area enclosed by the hysteresis loops is very small at the beginning of the fatigue test and becomes negligible as the cycling progresses.

Stress-strain curves in figure 3-12 demonstrate that the ‘plastic’ engineering shear strain per cycle changed minimally with increasing cycle count. It is seen that the slope of the hysteresis loops decreases as cycle count increases. The progressions with



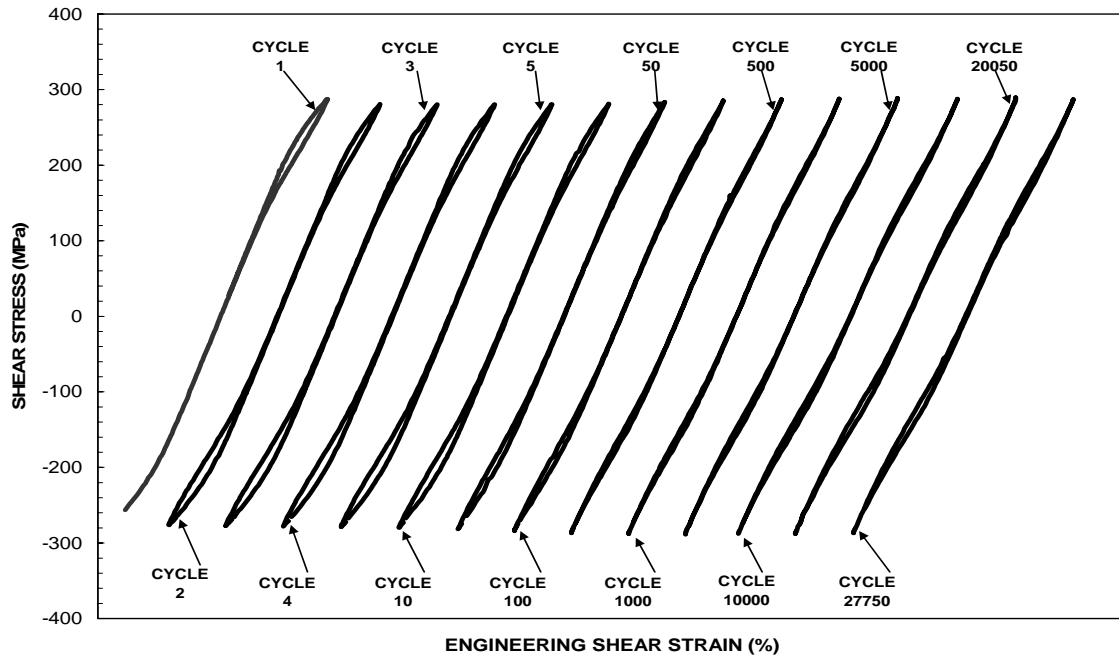


Figure 3-11. Hysteresis loop evolution in torsion fatigue test with a shear stress range of 576 MPa. Hysteresis loops for increasing cycles are offset to the right to show changes in shape of loops.

increasing cycle count of the maximum and minimum engineering shear strain are shown in figure 3-13. The maximum shear strain decreases from 1.29% (cycle 1) to 1.22% (cycle 2) where it remains stable for the first 5000 cycles. After cycle 5000, the maximum shear strain increases to 1.26% (cycle 27750) before dropping to 1.16% in the cycle immediately preceding failure.

The minimum engineering shear strain remains stable at -1.34% for the first 5000 cycles before decreasing to -1.41% on cycle 27750, then dropping to -1.51% in the cycle immediately preceding failure (cycle 27789). As seen in figure 3-13, the engineering shear strain range stabilizes at 2.57% (cycle 2) and decreases to 2.51% (cycle 50) before

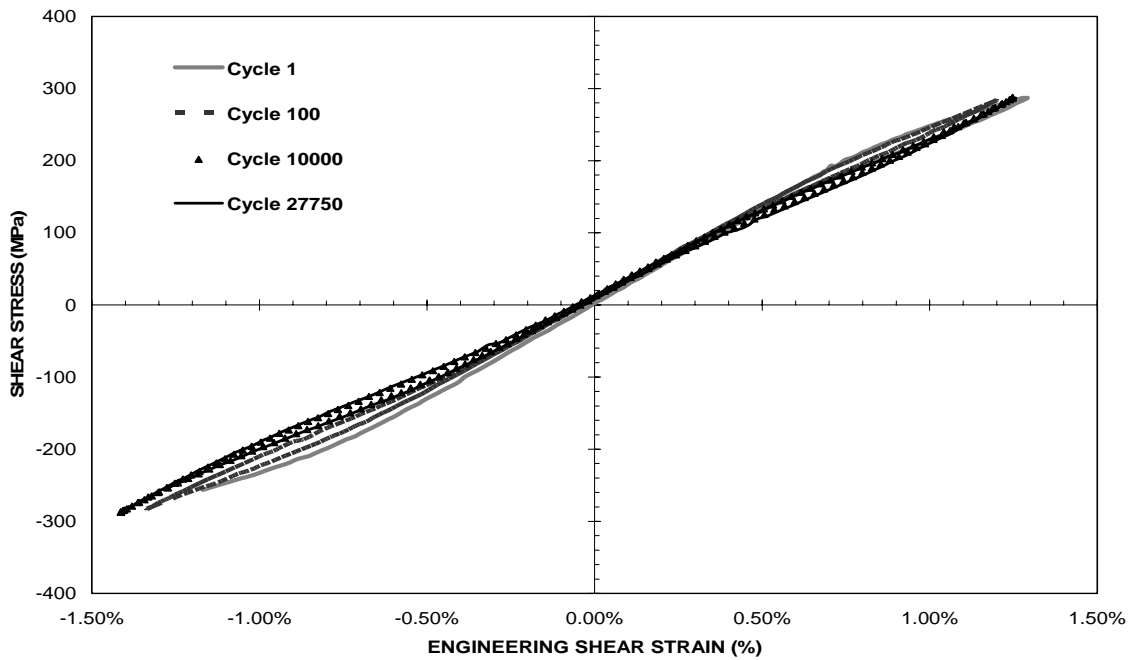


Figure 3-12. Shear stress-strain curves obtained in selected cycles of a torsion fatigue test with the shear stress range of 576 MPa.

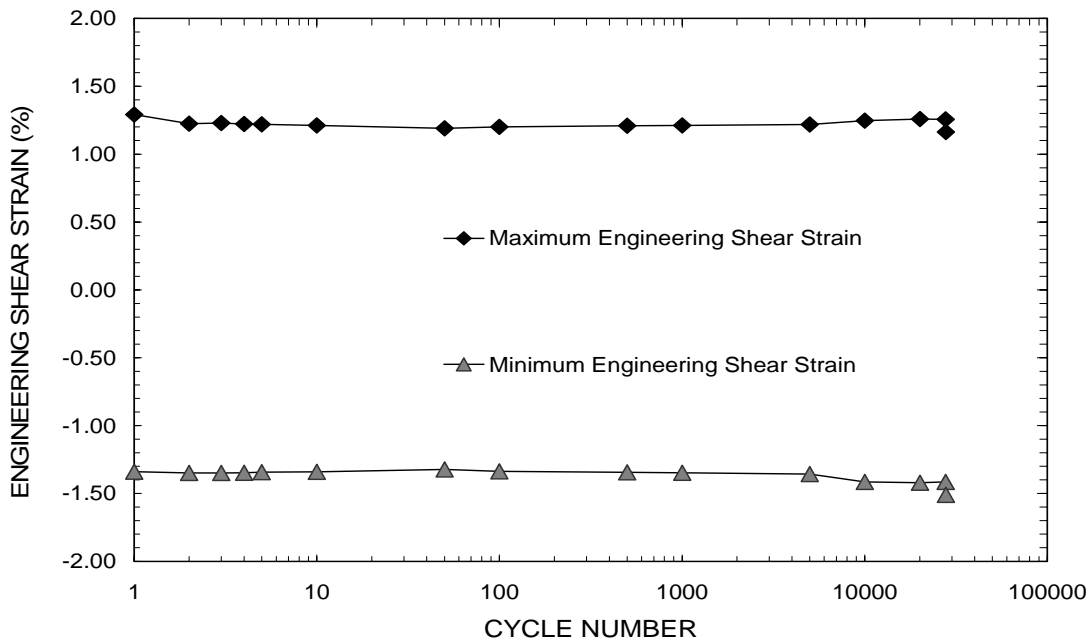


Figure 3-13. Evolution of maximum and minimum engineering shear strain with cycles in torsion fatigue test with the shear stress range of 576 MPa

stabilizing at 2.67% (cycle 10000). Material exhibits cyclically neutral behavior during the first 1000 cycles, followed by slight cyclic softening.

### 3.3.4 Torsion Fatigue with the 416 MPa Shear Stress Range

Cyclic hysteresis loops obtained in fatigue test with a shear stress range of 428 MPa are shown in figure 3-14. The ‘plastic’ engineering shear strain per cycle,  $\Delta\gamma_p$  decreases continuously throughout all 100,000 cycles. The loops become narrower in the first 100 cycles and then stabilize. Run-out was achieved in this test.

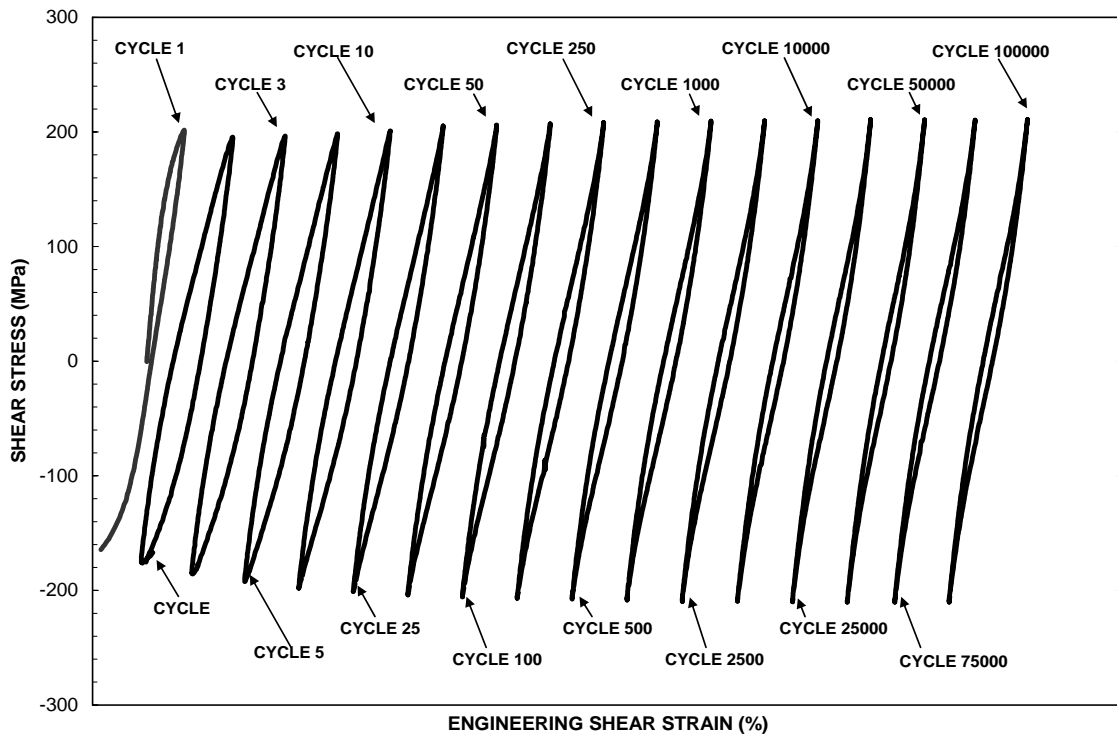


Figure 3-14. Hysteresis loop evolution in torsion fatigue test with a shear stress range of 416 MPa. Hysteresis loops for increasing cycles are offset to the right to show changes in shape of loops.

Figure 3-15 illustrates the evolution of the stress-strain behavior with cycling. As cycling progresses, stress-strain behavior becomes increasingly asymmetric. Minimum strain remains between -1.67% and -1.88% during the fatigue test. Conversely, maximum strain changes significantly from 1.04% to 0.35% in the course of the cyclic life.

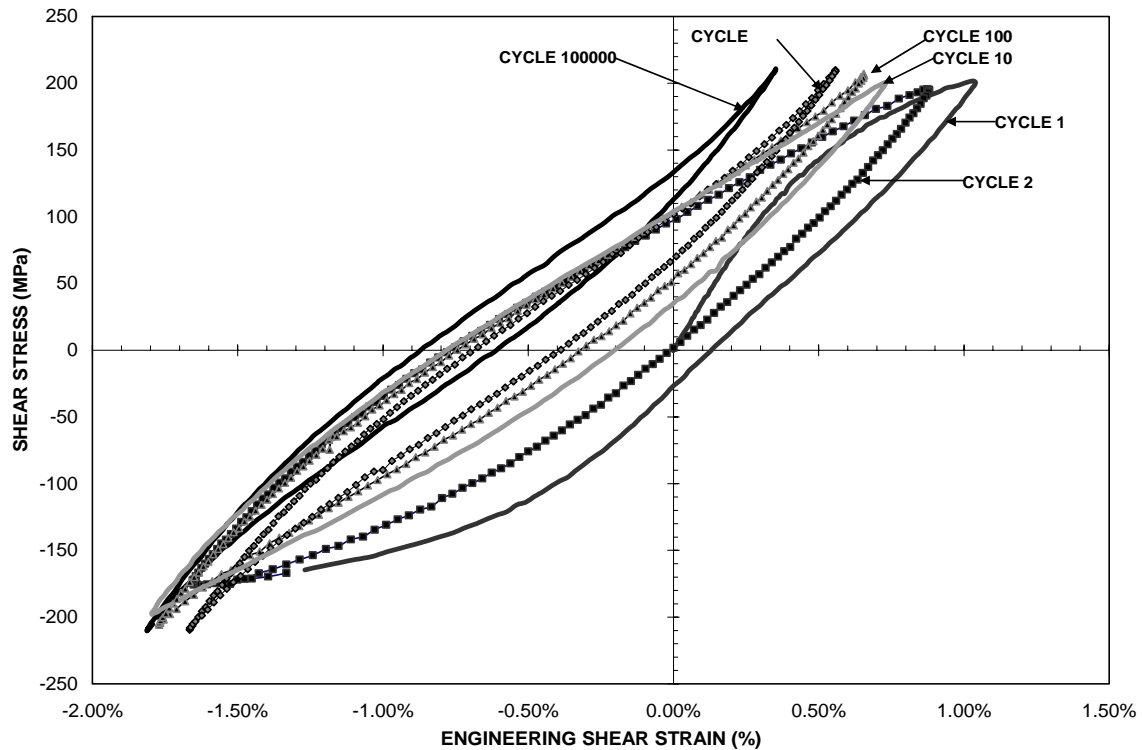


Figure 3-15. Shear stress-strain curves obtained in selected cycles of a torsion fatigue test with the shear stress range of 416 MPa.

Evolution of maximum and minimum strain with cycles is seen in figure 3-16. Maximum strain drops from 1.04% (cycle 1) to 0.88% (cycle 2), subsequently decreasing and reaching 0.35% at run-out. Minimum shear strain remains between -1.62% and -1.81% throughout the test. Cyclic softening is observed. This trend becomes less pronounced as the cycling progresses.

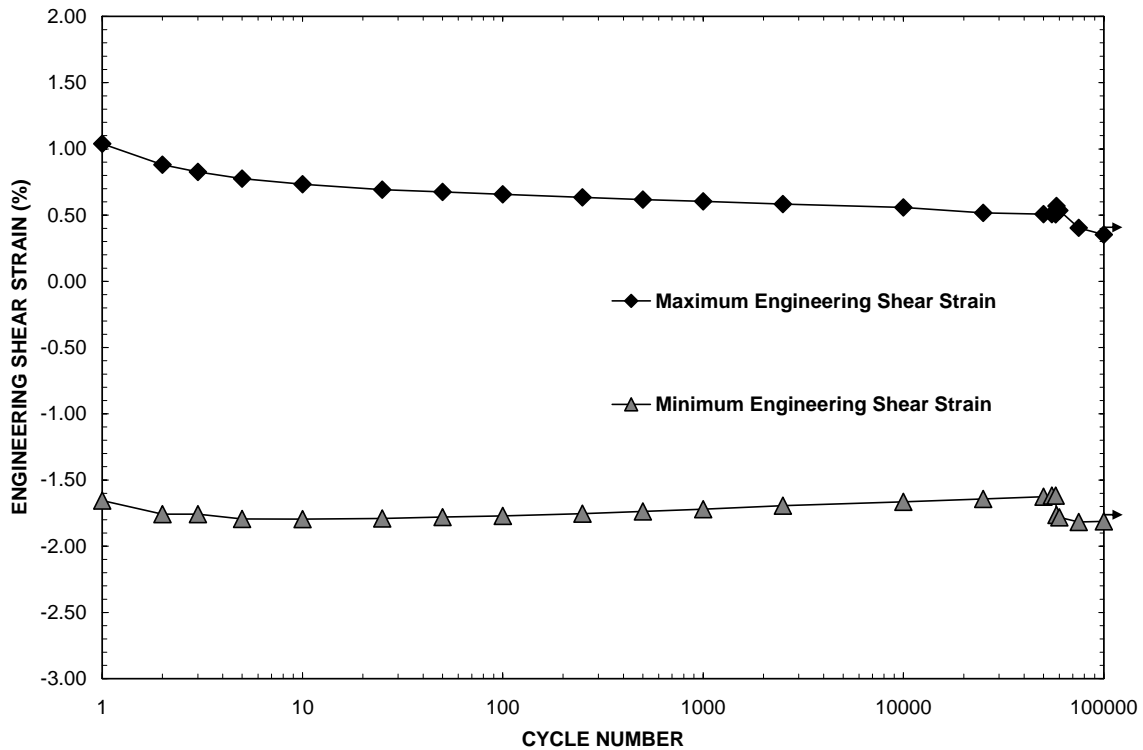


Figure 3-16. Evolution of maximum and minimum engineering shear strain with cycles in torsion fatigue test with the shear stress range of 416 MPa.

### 3.3.5 Evolution of Engineering Shear Strain Range in Torsion Fatigue

Figure 3-17 shows the engineering shear strain range as a function of fatigue cycles for all torsion fatigue tests. Results reveal cyclically neutral behavior in fatigue tests with shear stress range of 584 MPa. Slight hardening is observed in fatigue tests with shear stress range of 416 MPa. Fatigue test with the shear stress range of 674 MPa produced noticeable cyclic softening. Cyclic hardening followed by cyclic softening is observed in fatigue test with the shear stress range of 1310 MPa.

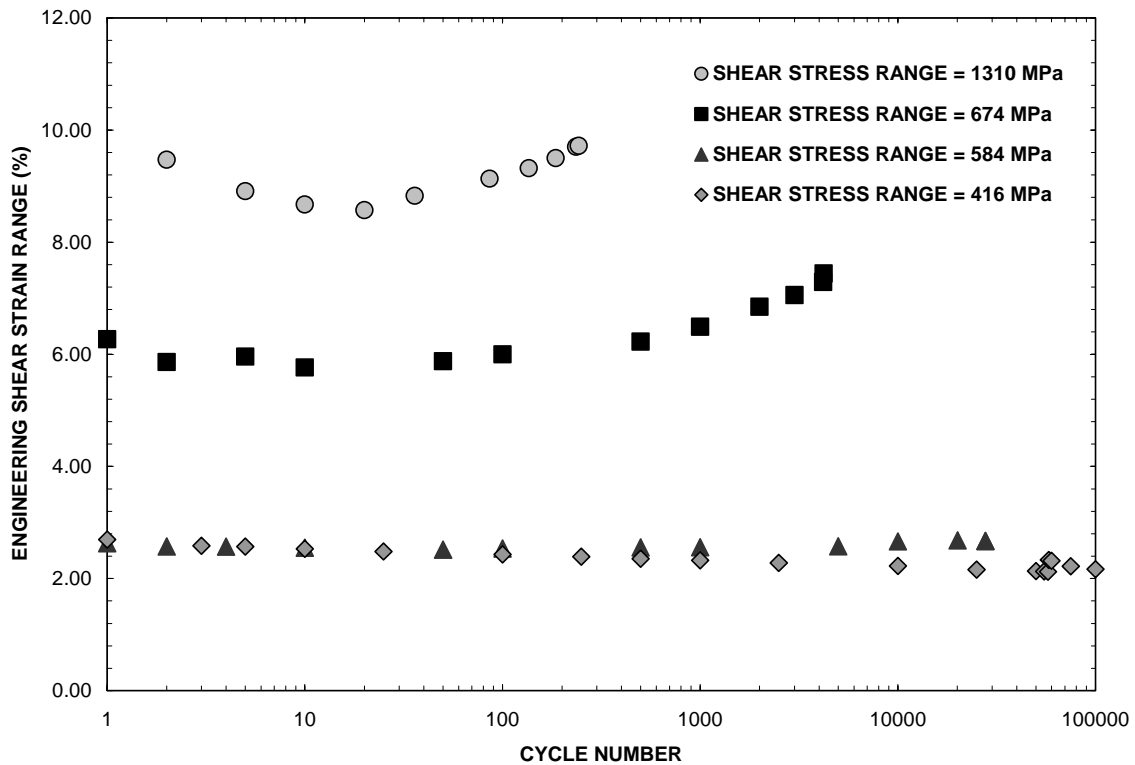


Figure 3-17. Shear strain range as a function of fatigue cycles.

### 3.4 Combined Tension-Torsion Fatigue Tests

The S-N curve for fully-reversed, combined tension-torsion fatigue is presented in figure 3-18 where effective (in the von Mises sense) stress range is plotted versus cycles to failure. Combined tension-torsion is significantly more damaging than pure torsion. For the effective stress range of ~1600 MPa cyclic life in combined tension-torsion is two orders of magnitude lower than in pure torsion. However, for effective stress ranges less than or equal to 1050 MPa, the trend is reversed. For effective stress ranges less than or equal to 1050 MPa, combined tension-torsion becomes less damaging than pure torsion. For a given effective stress range below 1050 MPa, longer fatigue life would be expected in combined tension-torsion than in pure torsion.

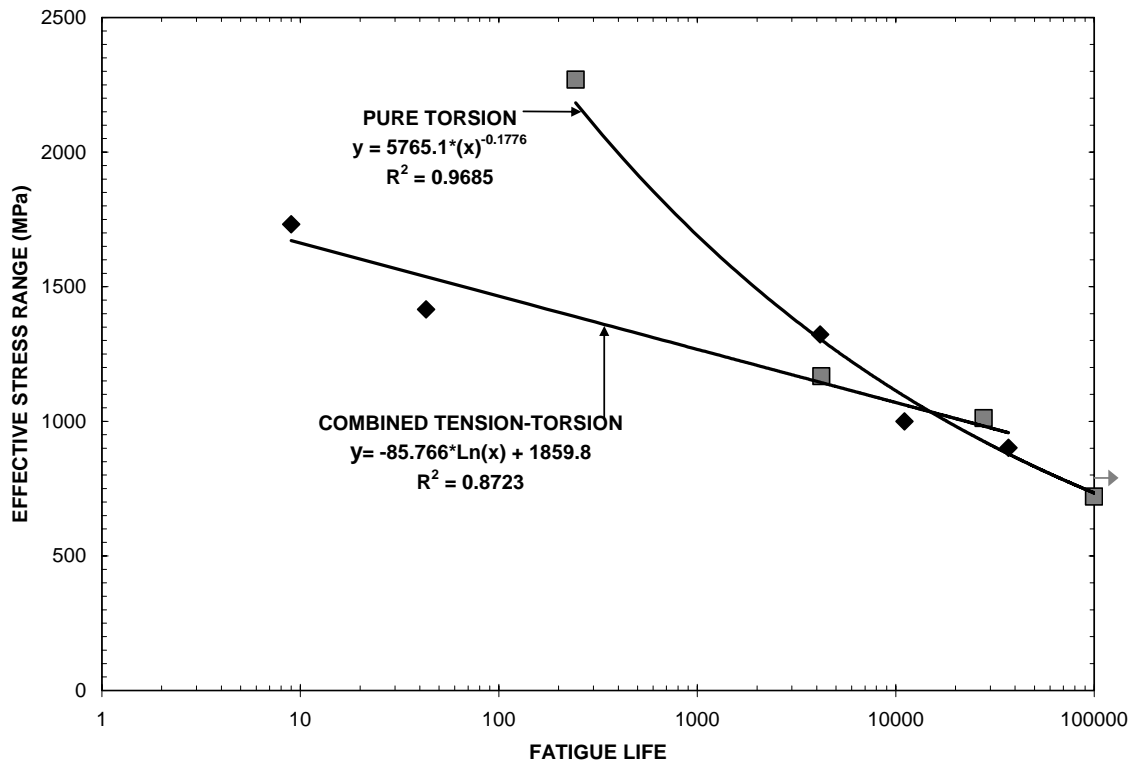


Figure 3-18. Effective Stress Range Versus Fatigue Life

For effective stress range of 2269 MPa a fatigue life of 243 cycles is achieved in pure torsion, while the same fatigue life in combined tension-torsion corresponds to an effective stress range of 1400 MPa (35% reduction in effective stress range). Conversely, for effective stress range values around 1000 MPa, torsion and combined tension-torsion fatigue would produce similar fatigue lives. This does make sense mathematically, as below 1000 MPa, the von Mises effective stress range is dominated by the torsional shear stress range. For effective stress range values below 1000 MPa, pure torsion becomes more damaging than combined tension-torsion fatigue. Combined tension-torsion fatigue test with the effective stress range of 1322 MPa produced a fatigue life of 4200 cycles. The same number of cycles to failure corresponds to a lower effective stress range of

1168 MPa in pure torsion. Additional tests would be required to further explore and confirm the observed trends.

### **3.4.1 Combined Tension-Torsion Fatigue, Axial Stress Range = 1480 MPa, Shear Stress Range = 500 MPa**

Fatigue test with an axial stress range of 1480 MPa and a shear stress range of 500 MPa (von Mises effective stress range = 1715 MPa) produced eight full cycles with failure occurring in tension on the ninth cycle. Figure 3-19 shows the axial stress-strain hysteresis loops.

The ‘plastic’ strain per cycle,  $\Delta\varepsilon_p$  decreases slightly as the cycle count increases. Hysteresis loops become narrower and pointed at the ends. The area inside each loop decreases with increasing cycle count. Figure 3-20 reveals that axial stress-stress behavior is asymmetric.

The shear stress-strain curves are shown in figure 3-21. The shear stress-strain hysteresis loops are narrow and irregular in shape with the sharp transition in shape occurring at zero stress. Figure 3-22 reveals that shear stress-strain behavior becomes progressively more asymmetric.

The evolution of the effective stress-effective strain hysteresis loops can be seen in figure 3-23. When both axial and shear hysteresis loops demonstrate asymmetry, the von Mises effective stress-effective strain is likewise asymmetric.



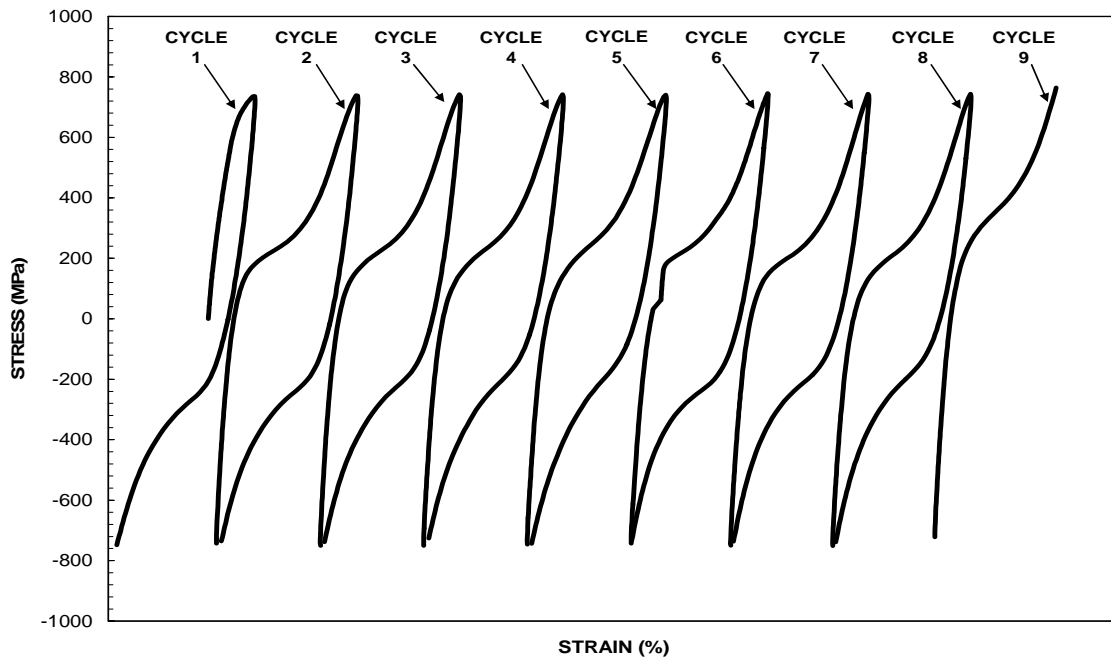


Figure 3-19. Evolution of axial hysteresis loop in combined tension-torsion fatigue with axial stress range of 1480 MPa and shear stress range of 500 MPa. Hysteresis loops for increasing cycles are offset to the right to show changes in shape of loops.

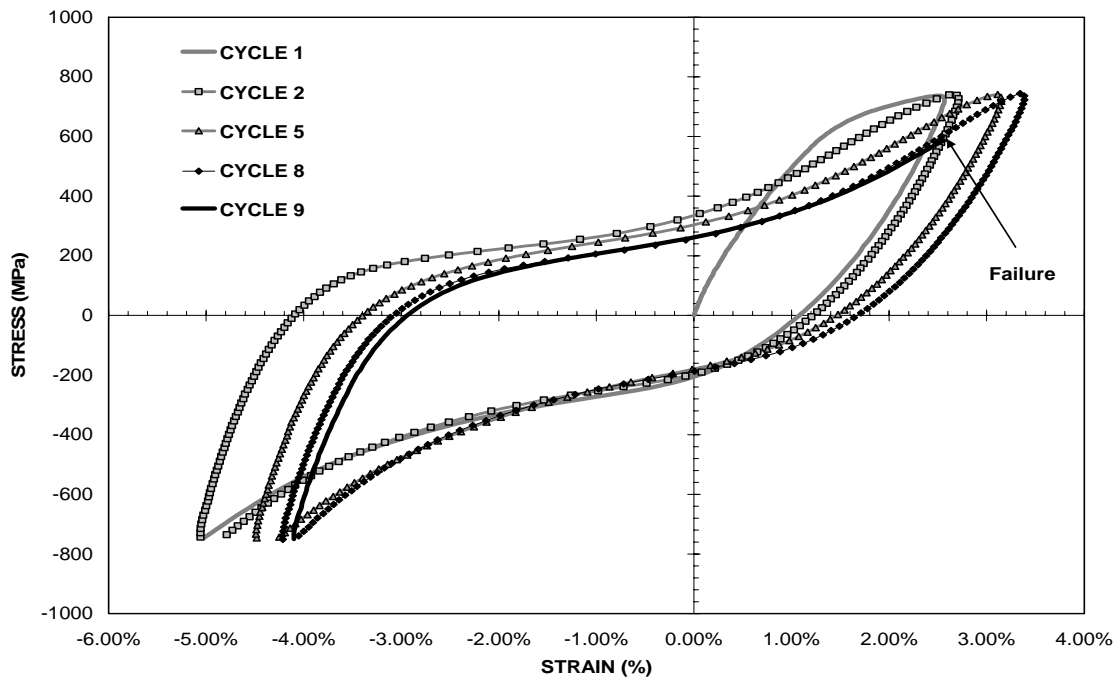


Figure 3-20. Axial stress-strain curves obtained in combined tension-torsion with axial stress range of 1480 MPa and shear stress range of 500 MPa.

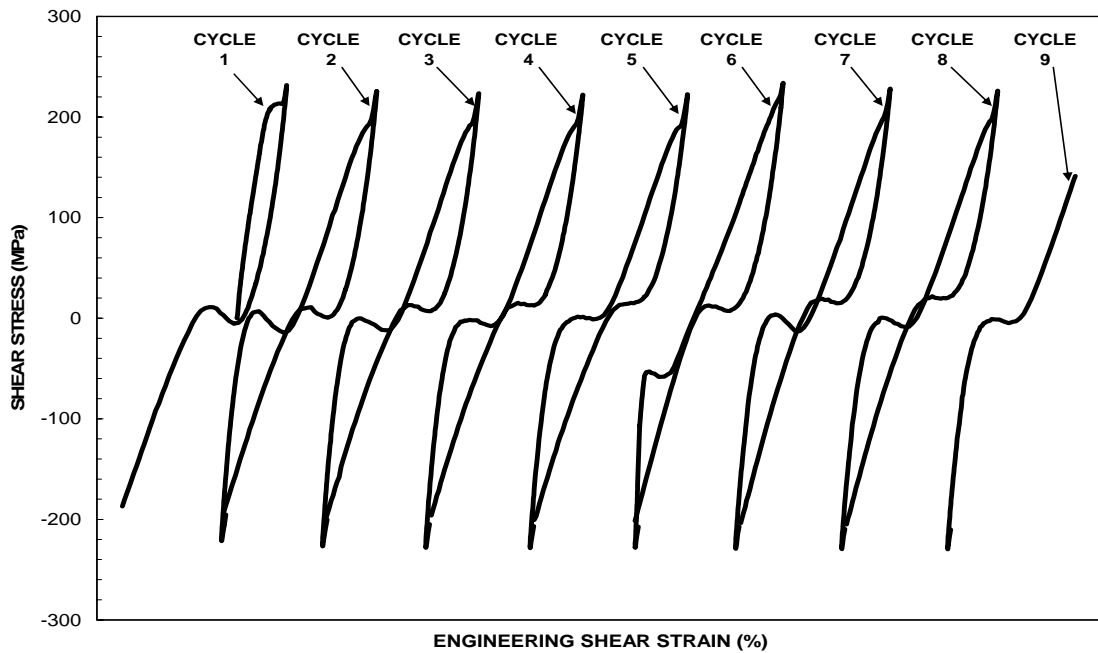


Figure 3-21. Shear stress-strain hysteresis loops obtained in combined tension-torsion fatigue test with an axial stress range of 1480 MPa and a shear stress range of 500 MPa. Hysteresis loops for increasing cycles are offset to the right to show changes in shape of loops.

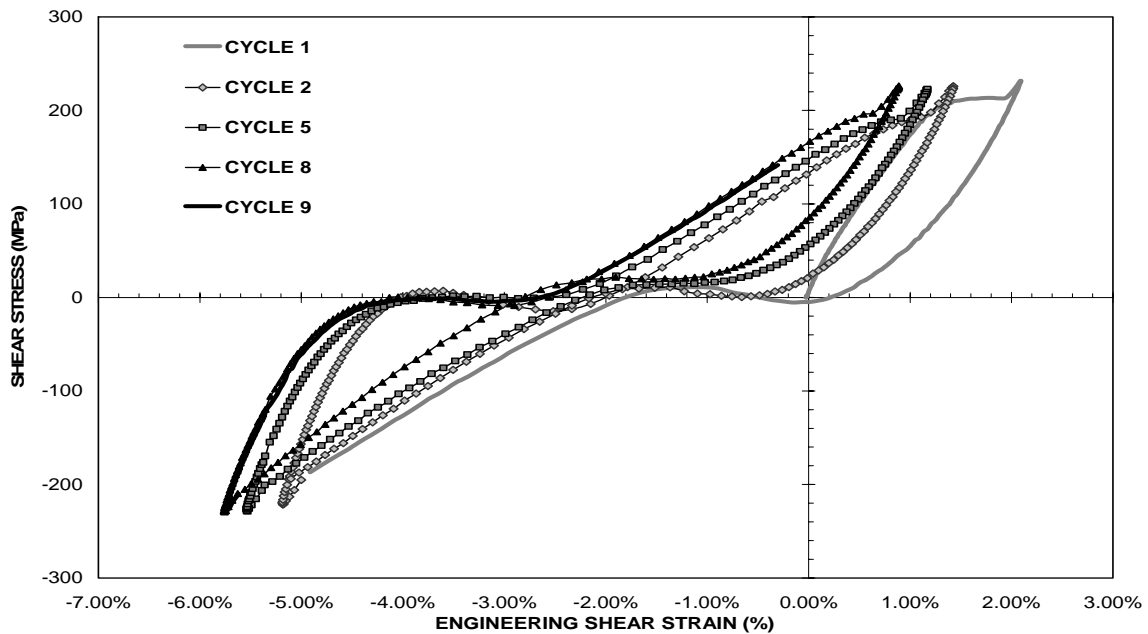


Figure 3-22. Shear stress-shear curves obtained in combined tension-torsion with axial stress range of 1480 MPa and shear stress range of 500 MPa.

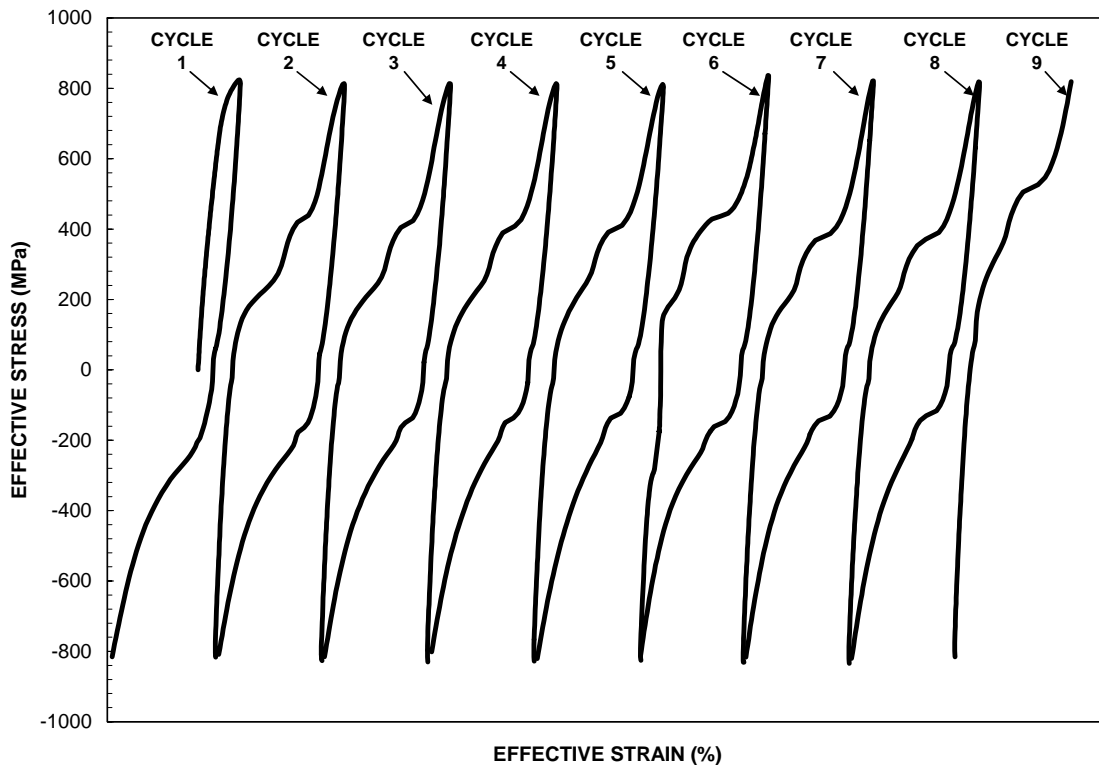


Figure 3-23. Effective stress-strain hysteresis loops obtained in combined tension-torsion fatigue test with an axial stress range of 1480 MPa and a shear stress range of 500 MPa. Hysteresis loops for increasing cycles are offset to the right to show changes in shape of loops.

The area inside of the effective stress-strain hysteresis loops reduces slightly and the ends of the loops at the maximum effective stress amplitudes become sharper as cycle count increases. The asymmetry of effective stress-strain behavior is further revealed in figure 3-24.

Figure 3-25 shows the evolution of the maximum and minimum strain, maximum shear strain, and effective strain with increasing cycle number. Both maximum strain and minimum strain increase as cycle count increases. This indicates that axial strain ratcheting takes place. The axial strain range,  $\Delta\epsilon$ , remains nearly constant throughout all 8 cycles. Maximum shear strain drops significantly from 2.09% to 0.89% in the first 8

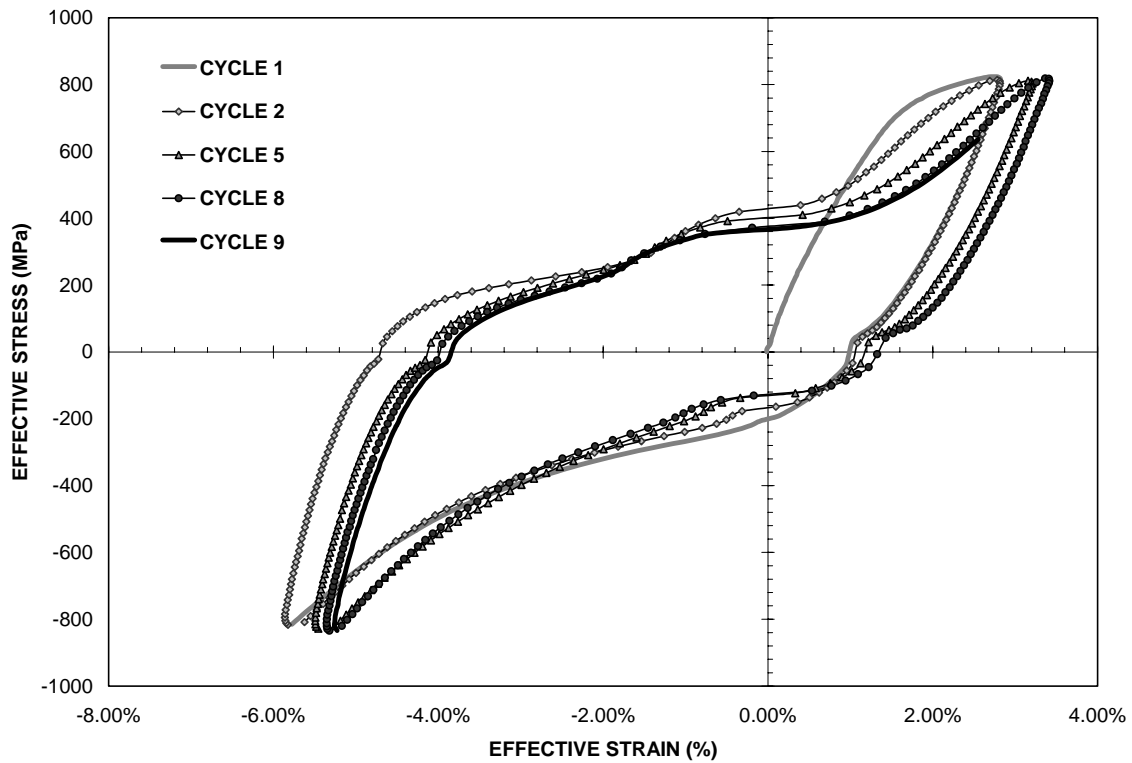


Figure 3-24. Effective stress-strain curves obtained in combined tension-torsion with axial stress range of 1480 MPa and shear stress range of 500 MPa.

cycles, while minimum shear strain decreases from  $-5.19\%$  on cycle 2 to  $-5.76\%$  on cycle 8. These drops in both minimum and maximum engineering shear strain indicate strain softening. The maximum effective strain increases from  $2.83\%$  (cycle 2) to  $3.42\%$  (cycle 8). The maximum effective strain is close the maximum strain, in fact the data points overlap on cycles 2-8. The minimum effective strain increases from  $-5.86\%$  to  $-5.35\%$  during cycles 1-8. The effective strain range,  $\Delta\varepsilon_{\text{eff}}$ , remains constant.

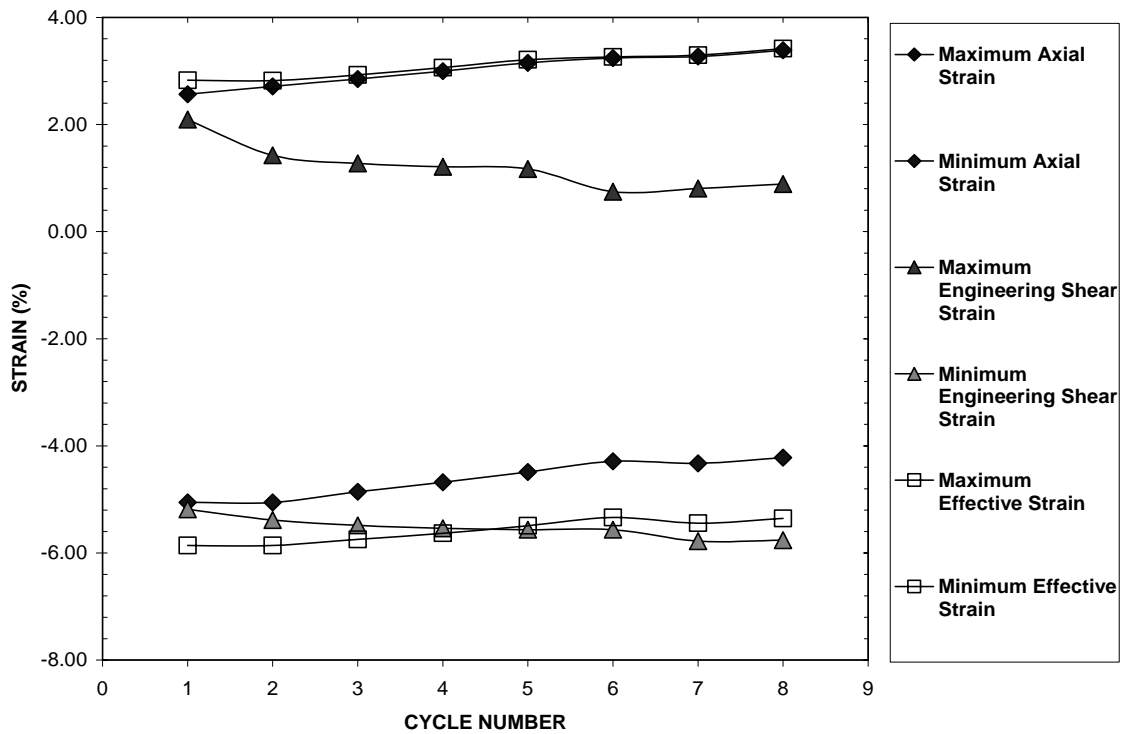


Figure 3-25. Evolution maximum and minimum axial strain, shear strain, and effective strain with fatigue cycles in a fatigue test with axial stress range of 1480 MPa and shear stress range of 500 MPa.

### 3.4.2 Combined Tension-Torsion Fatigue, Axial Stress Range = 1120 MPa, Shear Stress Range = 500 MPa

Fatigue test with an axial stress range of 1120 MPa and a shear stress range of 500 MPa (von Mises effective stress range = 1416 MPa) produced 42 full cycles with failure occurring in tension on cycle 43.

Axial hysteresis loops are shown in figure 3-26. The ‘plastic’ strain per cycle,  $\Delta\epsilon_p$ , decreases throughout all 42 cycles. The shape of axial hysteresis loops stabilizes cycle 10. From cycle 10 on hysteresis loops are narrow with smooth tension-going and compression-going stress-strain curves.

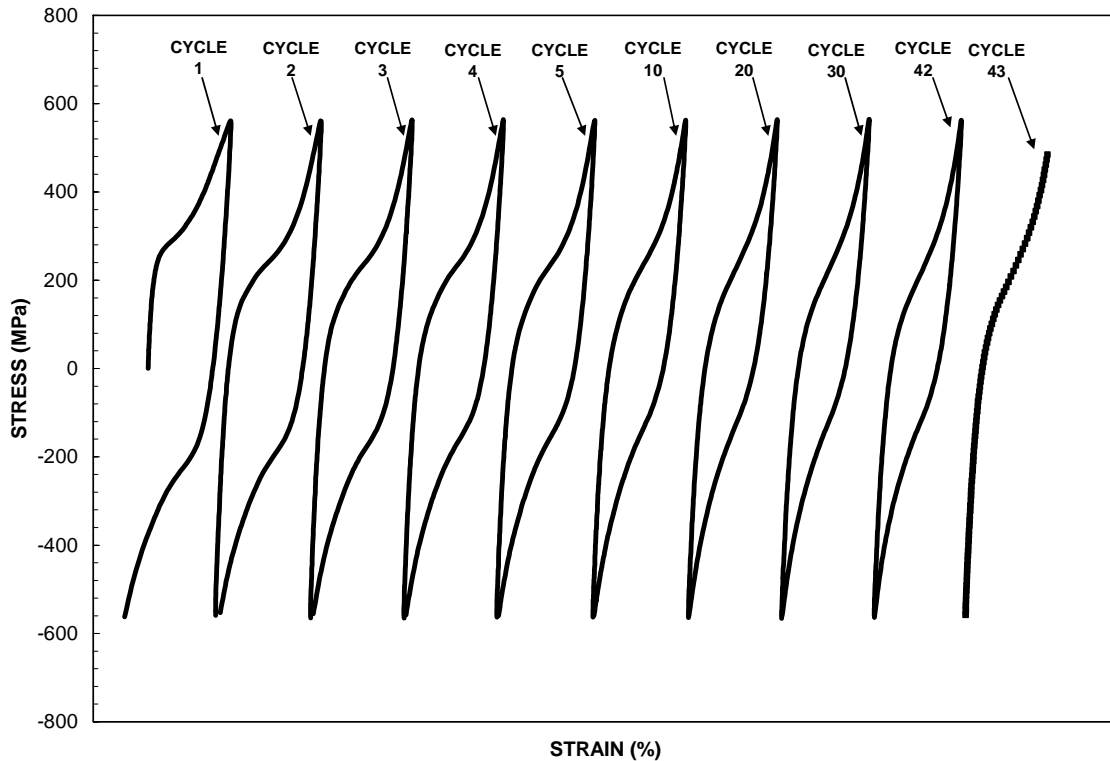


Figure 3-26. Axial stress-strain hysteresis loops obtained in combined tension-torsion fatigue test with an axial stress range of 1120 MPa and a shear stress range of 500 MPa. Hysteresis loops for increasing cycles are offset to the right to show changes in shape of loops.

Figure 3-27 reveals asymmetry of the axial stress-strain curves. The ‘plastic’ strain range,  $\Delta\epsilon_p$ , decreases significantly as cycle count increases. Noteworthy shift of the loops takes place where axial stress changes sign. The decreases in  $\Delta\epsilon_p$  and area inside the loop are primarily due to the portion of the hysteresis loop in the upper half plane as cycling progresses.

The shear stress-strain hysteresis loops can be seen in figure 3-28. As cycle count increases, hysteresis loops assume a more regular, “flatter” appearance. Shear strain ratcheting is evident in figure 3-29.

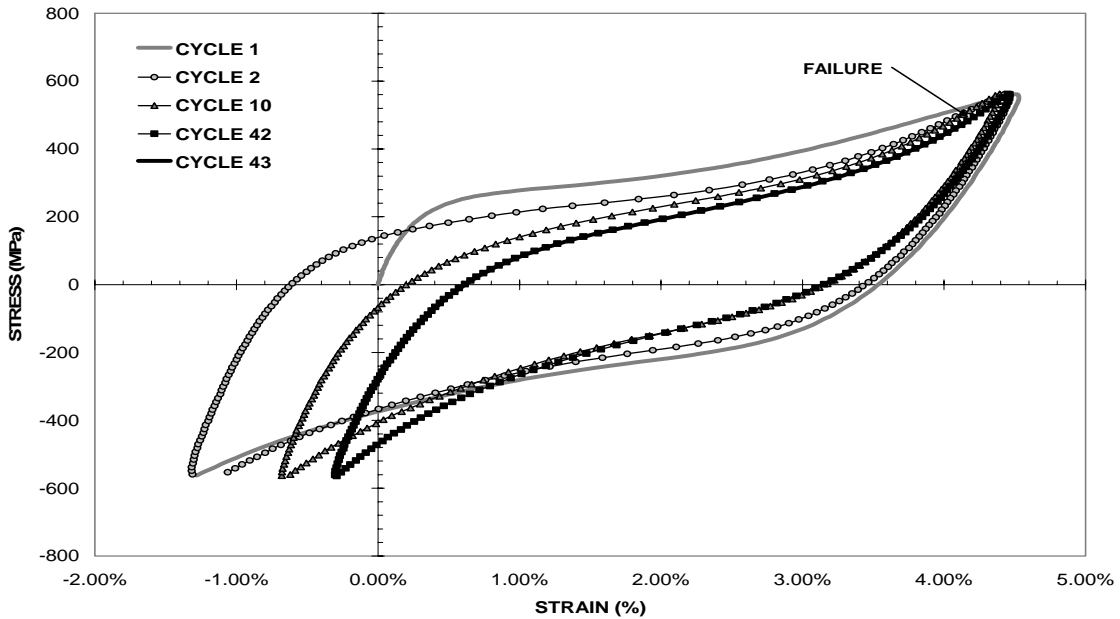


Figure 3-27. Axial stress-strain curves obtained in combined tension-torsion with axial stress range of 1120 MPa and shear stress range of 500 MPa.

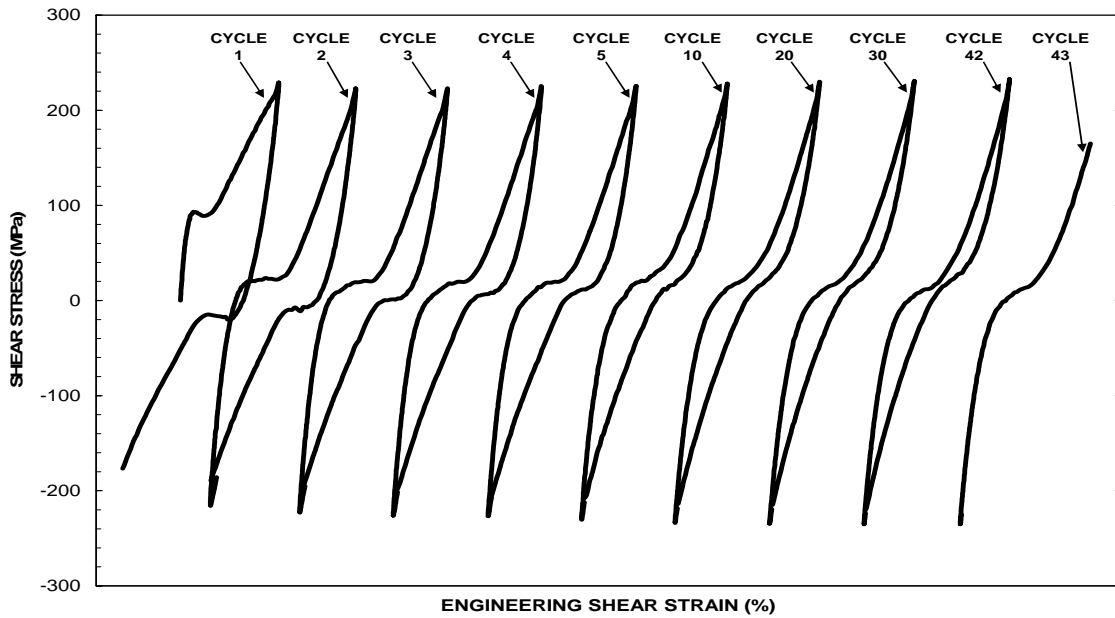


Figure 3-28. Shear stress-strain hysteresis loops obtained in combined tension-torsion fatigue test with an axial stress range of 1120 MPa and a shear stress range of 500 MPa. Hysteresis loops for increasing cycles are offset to the right to show changes in shape of loops.

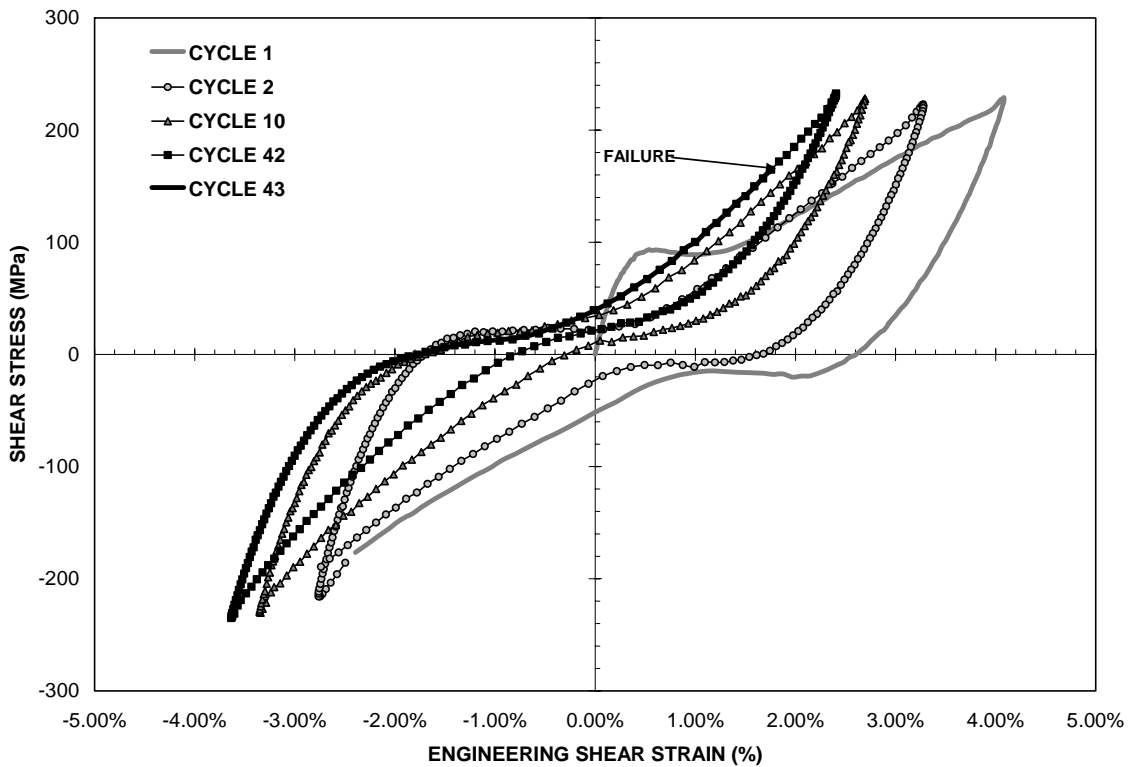


Figure 3-29. Shear stress-strain curves obtained in combined tension-torsion with axial stress range of 1120 MPa and shear stress range of 500 MPa.

Figure 3-30 shows the evolution of effective stress-strain hysteresis loops with cycles. Area within the hysteresis loops decreases with cycling. The loops maintain their irregular shape throughout the test. It is noteworthy that while the portion of the loop located in upper half-plane changes throughout the test, the portion located in the lower half-plane remains stable.

Figure 3-31 shows effective stress-strain curves for selected cycles. Effective stress-strain behavior is very much asymmetric. Area enclosed by effective stress-strain hysteresis loops decreases considerably with fatigue cycles.



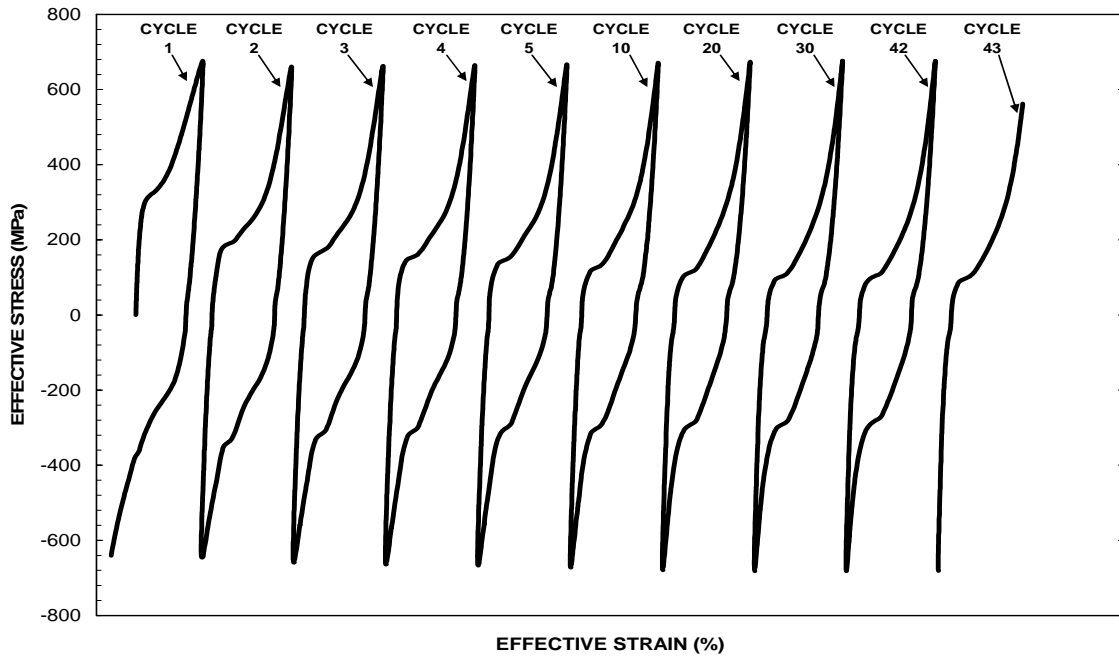


Figure 3-30. Effective stress-strain hysteresis loops obtained in combined tension-torsion fatigue test with an axial stress range of 1120 MPa and a shear stress range of 500 MPa. Hysteresis loops for increasing cycles are offset to the right to show changes in shape of loops.

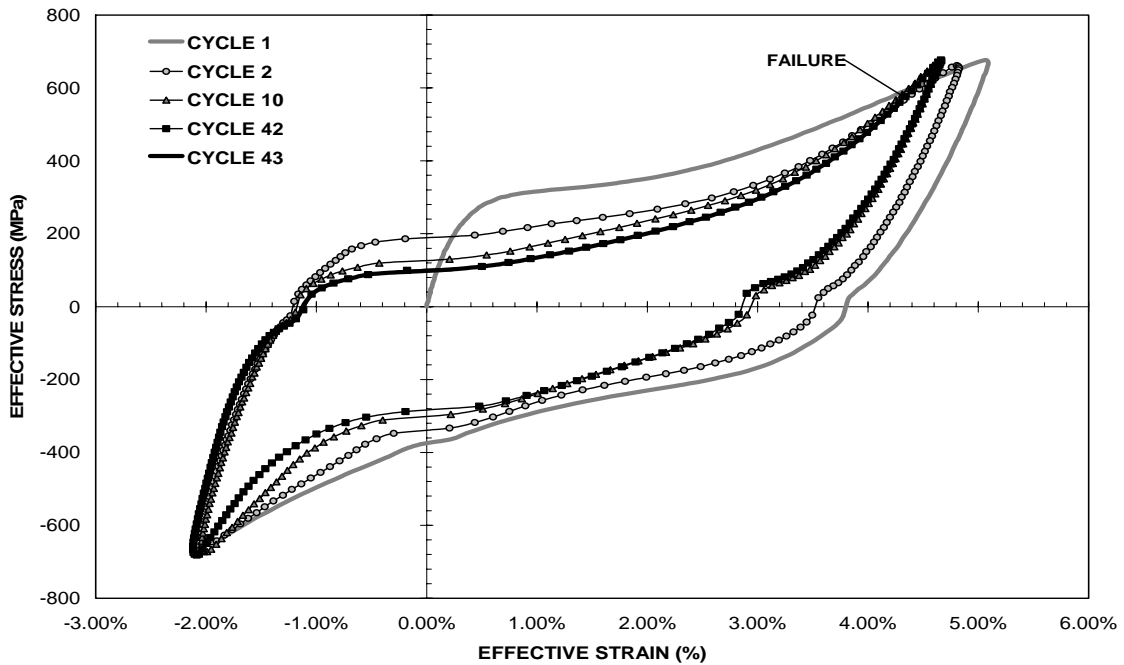


Figure 3-31. Effective stress-strain curves obtained in combined tension-torsion with axial stress range of 1120 MPa and shear stress range of 500 MPa.

Figure 3-32 shows the maximum and minimum axial strain, engineering shear strain, and effective strain progression as functions of cycle number. The maximum axial strain decreases from 4.53% (cycle 1) to 4.39% at cycle 10 where it remains until cycle 20 before rising to 4.46% (cycle 42). The minimum axial strain steadily increases from -1.32% (cycle 1) to -0.30% (cycle 42). The axial strain range decreases from 5.84% to 4.77% over the first 42 cycles, indicating slight cyclic hardening.

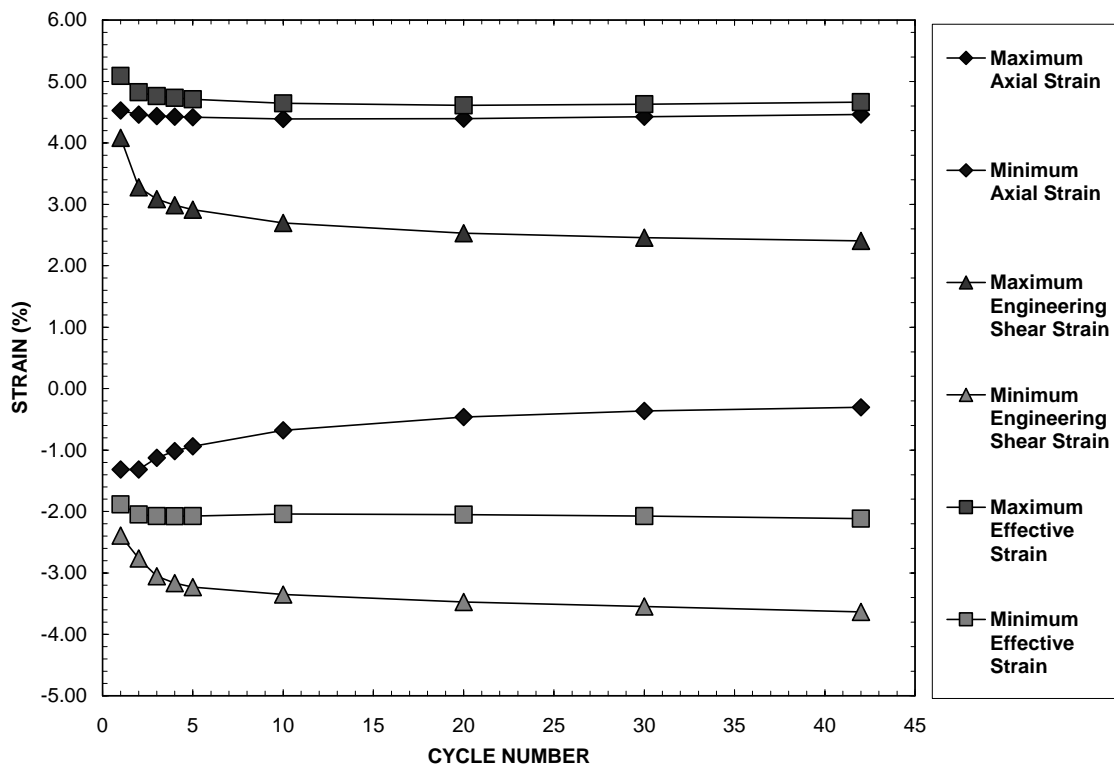


Figure 3-32. Evolution maximum and minimum axial strain, shear strain, and effective strain with fatigue cycles in a fatigue test with axial stress range of 1120 MPa and shear stress range of 500 MPa.

Both the maximum and minimum engineering shear strain decrease with fatigue cycling. While the maximum shear strain decreases from 4.08% to 2.41% and the minimum shear strain decreases from -2.39% to -3.63% throughout 42 cycles, the engineering shear

strain range changes from 6.48% to 6.04%. The maximum effective strain decreases slightly from 5.09% (cycle 1) to 4.67% (cycle 42). The minimum effective strain shows an increase of 0.24% from cycles 1-42. The increase in minimum axial strain combined with the decrease in minimum shear strain results in minimal change in the minimum effective strain as cycle count increases. The effective strain range remains constant.

### **3.4.3 Combined Tension-Torsion Fatigue, Axial Stress Range = 1000 MPa, Shear Stress Range = 500 MPa**

Fatigue test with an axial stress range of 1000 MPa and a shear stress range of 500 MPa (von Mises effective stress range = 1323 MPa) survived 4163 cycles before failing on cycle 4164 in tension.

The evolution of axial hysteresis loops can be seen in figure 3-33. The ‘plastic’ strain per cycle,  $\Delta\varepsilon_p$ , is small and becomes negligible with increasing cycles. After the first 100 cycles,  $\Delta\varepsilon_p$  is hardly distinguishable. The thin hysteresis loop seen in cycle 2 is very similar in shape to the loop observed in cycle 4150.

Figure 3-34 demonstrates that axial stress-strain behavior is asymmetric through fatigue life. All cycles show asymmetry, as 65% of the hysteresis loops appear in positive strain space. Shear stress-strain hysteresis loops for selected cycles are shown in figure 3-35. Shear stress-strain hysteresis loops in figure 3-35 are similar in shape to the axial stress-strain loops shown in figure 3-33. Both axial and shear hysteresis loops are very narrow. Area within each loop decreases from small to negligible as fatigue cycling progresses. Figure 3-36 reveals that shear stress-strain behavior is almost symmetric.

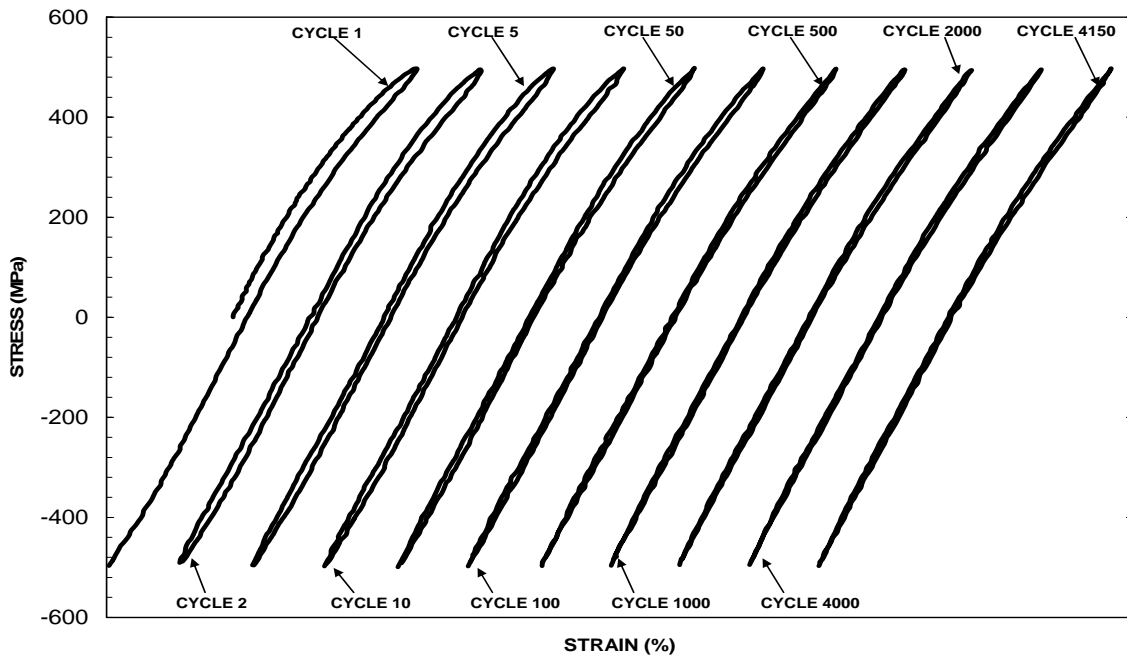


Figure 3-33. Axial stress-strain hysteresis loops obtained in combined tension-torsion fatigue test with an axial stress range of 1000 MPa and a shear stress range of 500 MPa. Hysteresis loops for increasing cycles are offset to the right to show changes in shape of loops.

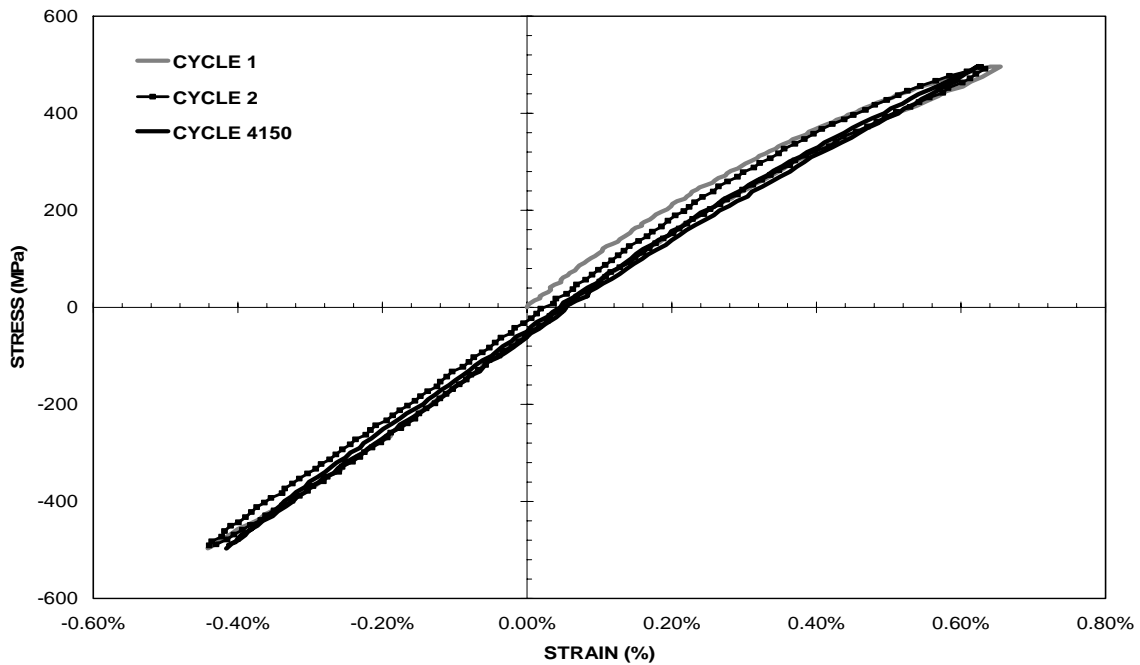


Figure 3-34. Axial stress-strain curves obtained in combined tension-torsion with axial stress range of 1000 MPa and shear stress range of 500 MPa.

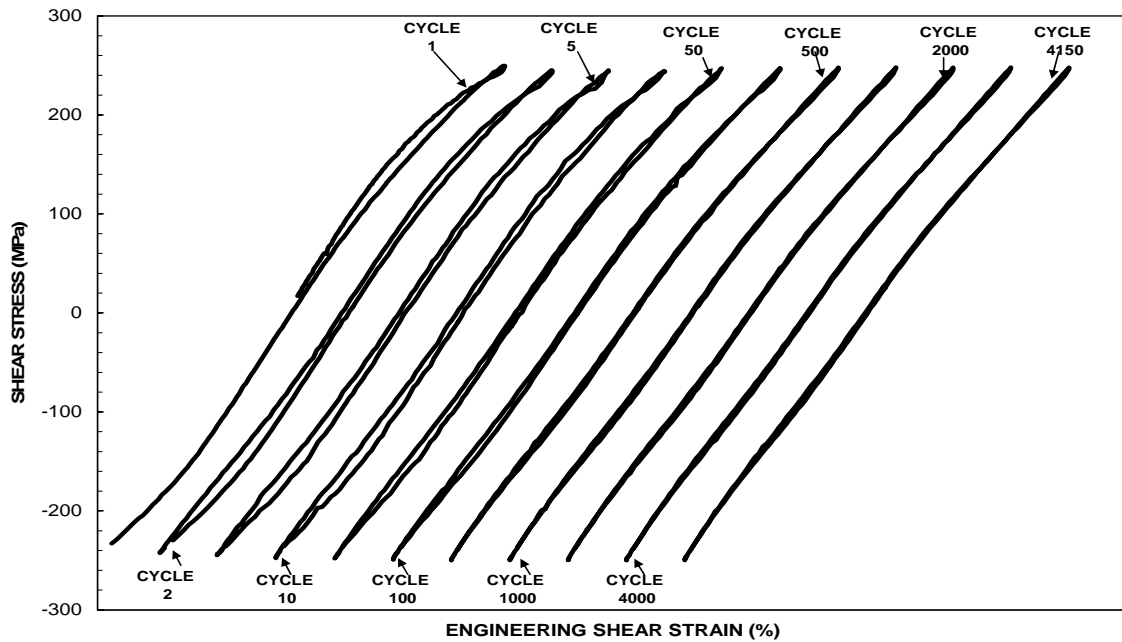


Figure 3-35. Shear stress-strain hysteresis loops obtained in combined tension-torsion fatigue test with an axial stress range of 1000 MPa and a shear stress range of 500 MPa. Hysteresis loops for increasing cycles are offset to the right to show changes in shape of loops.

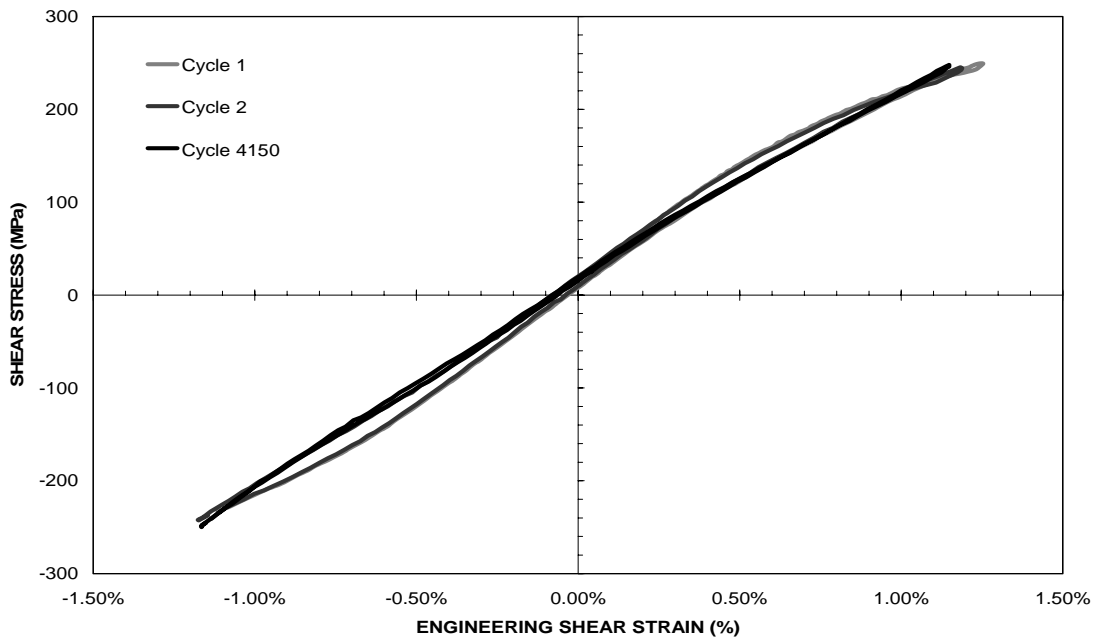


Figure 3-36. Shear stress-strain curves obtained in combined tension-torsion with axial stress range of 1000 MPa and shear stress range of 500 MPa.

Effective stress-strain hysteresis loops are shown in figure 3-37 for selected cycles. The hysteresis loops are narrow; area within a hysteresis loop is small and decreases with cycling.

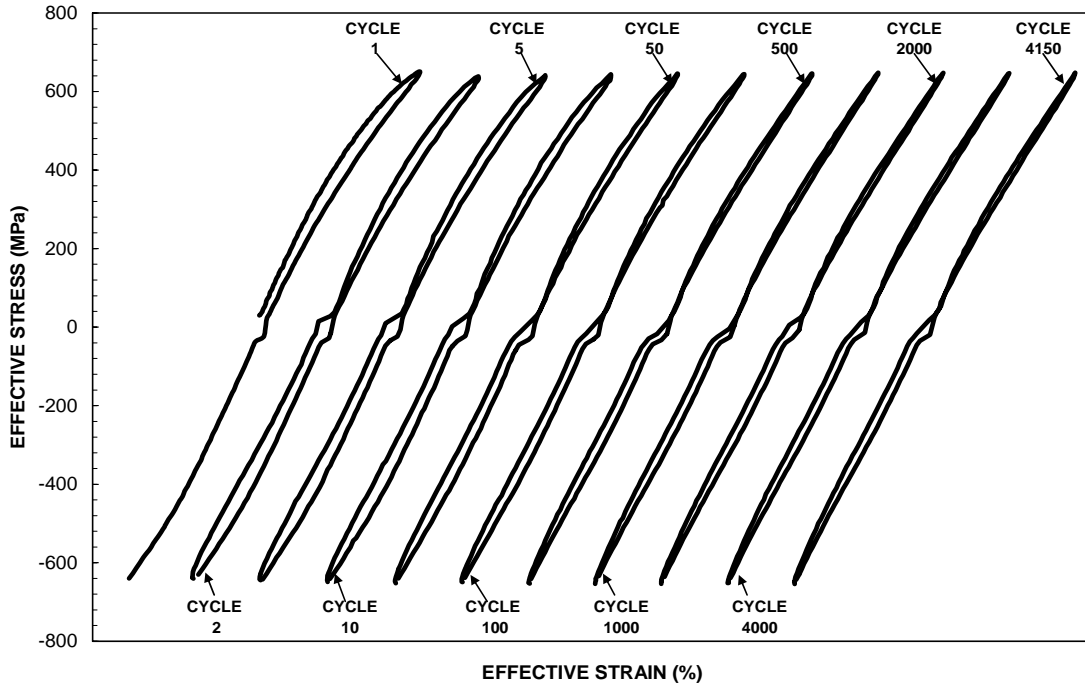


Figure 3-37. Effective stress-strain hysteresis loops obtained in combined tension-torsion fatigue test with an axial stress range of 1000 MPa and a shear stress range of 500 MPa. Hysteresis loops for increasing cycles are offset to the right to show changes in shape of loops.

Effective stress-strain curves in figure 3-38 appear to be nearly symmetric, only a slight bias in tension is observed. Area is small and becomes negligible with fatigue cycling.

Figure 3-39 shows progression of the maximum and minimum axial strain, engineering shear strain, and effective strain as functions of cycle number. It is seen that axial strain range, shear strain range, and effective strain range remain nearly constant. Material exhibits cyclically neutral behavior.

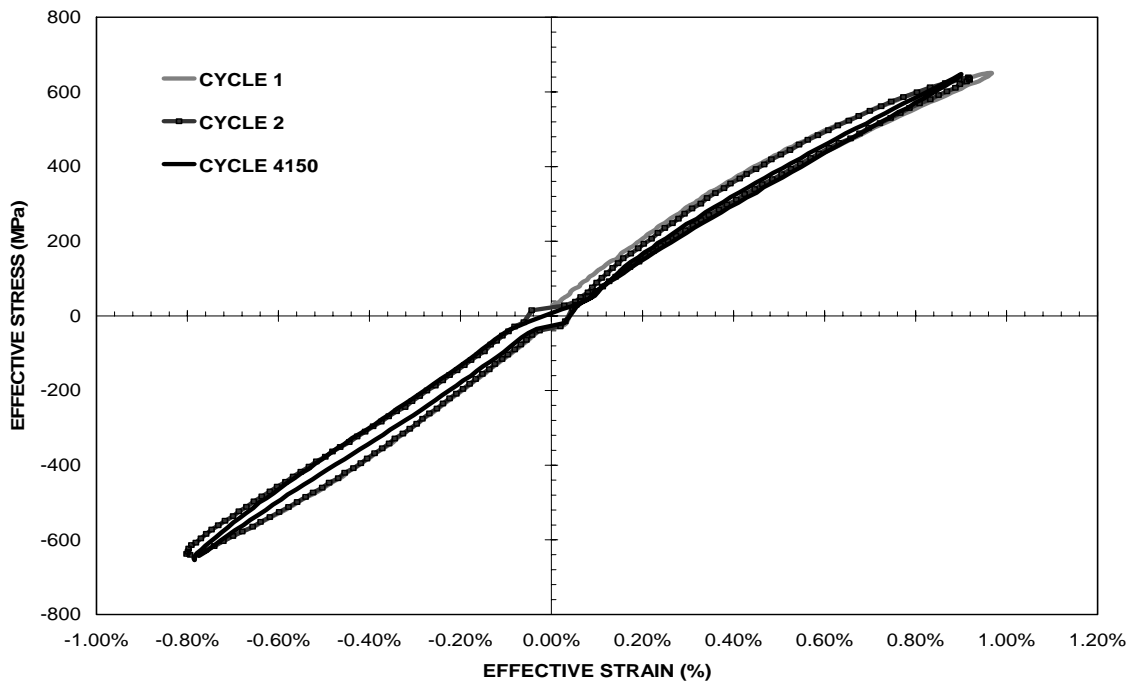


Figure 3-38. Effective stress-strain curves obtained in combined tension-torsion with axial stress range of 1000 MPa and shear stress range of 500 MPa.

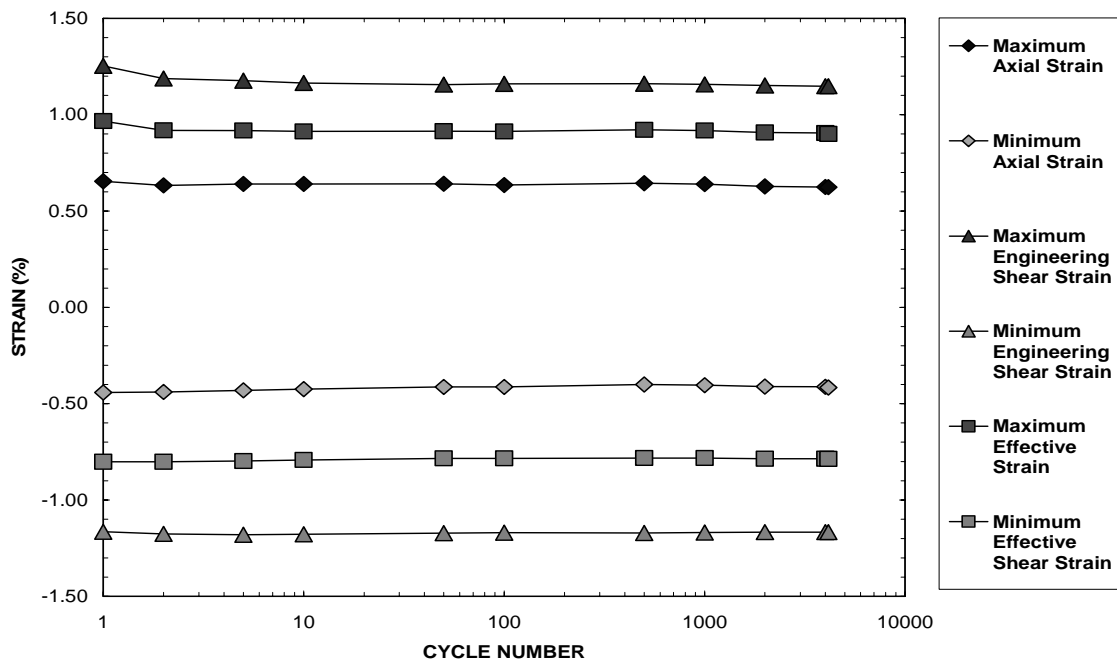


Figure 3-39. Evolution maximum and minimum axial strain, shear strain, and effective strain with fatigue cycles in a fatigue test with axial stress range of 1000 MPa and shear stress range of 500 MPa.

### **3.4.4 Combined Tension-Torsion Fatigue, Axial Stress Range = 500 MPa, Shear Stress Range = 500 MPa**

Fatigue test with an axial stress range of 500 MPa and a shear stress range of 500 MPa (von Mises effective stress range = 1000 MPa) failed in tension on cycle 11079.

The evolution of the axial hysteresis loops with increasing cycle count can be seen in figure 3-42. The ‘plastic’ strain per cycle,  $\Delta\varepsilon_p$ , and the area inside each hysteresis loop decrease as cycle count increases. The largest reduction in area and  $\Delta\varepsilon_p$  occurs in the first 100 cycles before the loop size and shape stabilize. Only slight reductions in area and  $\Delta\varepsilon_p$  are noted after cycle 100.

Figure 3-41 demonstrates the asymmetry of the axial stress-strain behavior. The asymmetric loops collapse with increasing cycle count. Figure 3-41 also reveals that the slope of the line drawn through peak and valley points of a given cycle increases as cycling progresses.

Shear stress-strain hysteresis loops for selected cycles are shown in figure 3-42. It is seen that the ‘plastic’ engineering shear strain range and the area inside each hysteresis loop decrease as cycle count increases. The shape of shear hysteresis loops becomes stable at cycle 1000. The loops become narrower and the slope of the line drawn through the peak and valley point of a given loop increases with increasing cycle count. Shear stress-strain curves in figure 3-43 demonstrate that cyclic stress-strain behavior rapidly becomes asymmetric as peak strain decreases and valley strain increases (albeit slightly) with cycling.



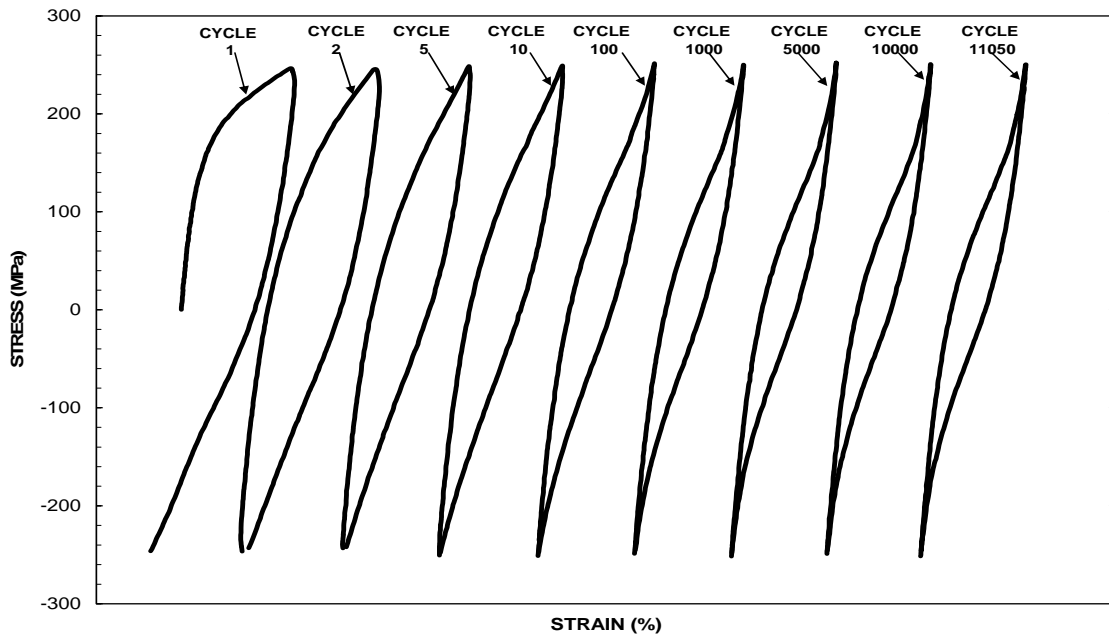


Figure 3-40. Axial stress-strain hysteresis loops obtained in combined tension-torsion fatigue test with an axial stress range of 500 MPa and a shear stress range of 500 MPa. Hysteresis loops for increasing cycles are offset to the right to show changes in shape of loops.

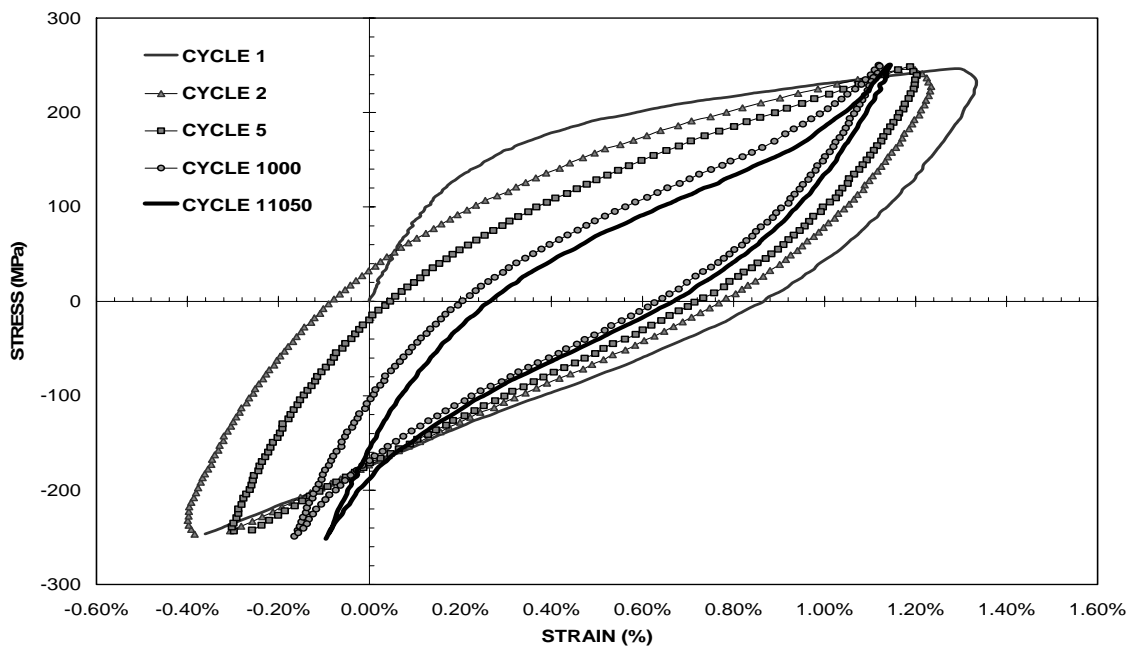


Figure 3-41. Axial stress-strain curves obtained in combined tension-torsion with axial stress range of 500 MPa and shear stress range of 500 MPa.

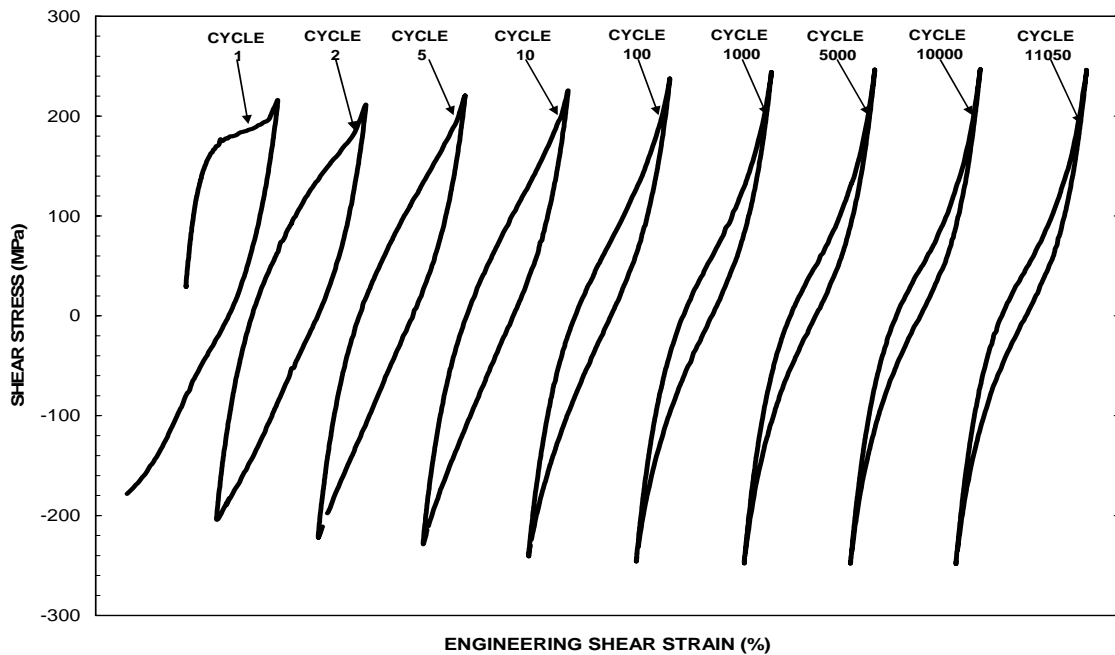


Figure 3-42. Shear stress-strain hysteresis loops obtained in combined tension-torsion fatigue test with an axial stress range of 500 MPa and a shear stress range of 500 MPa. Hysteresis loops for increasing cycles are offset to the right to show changes in shape of loops.

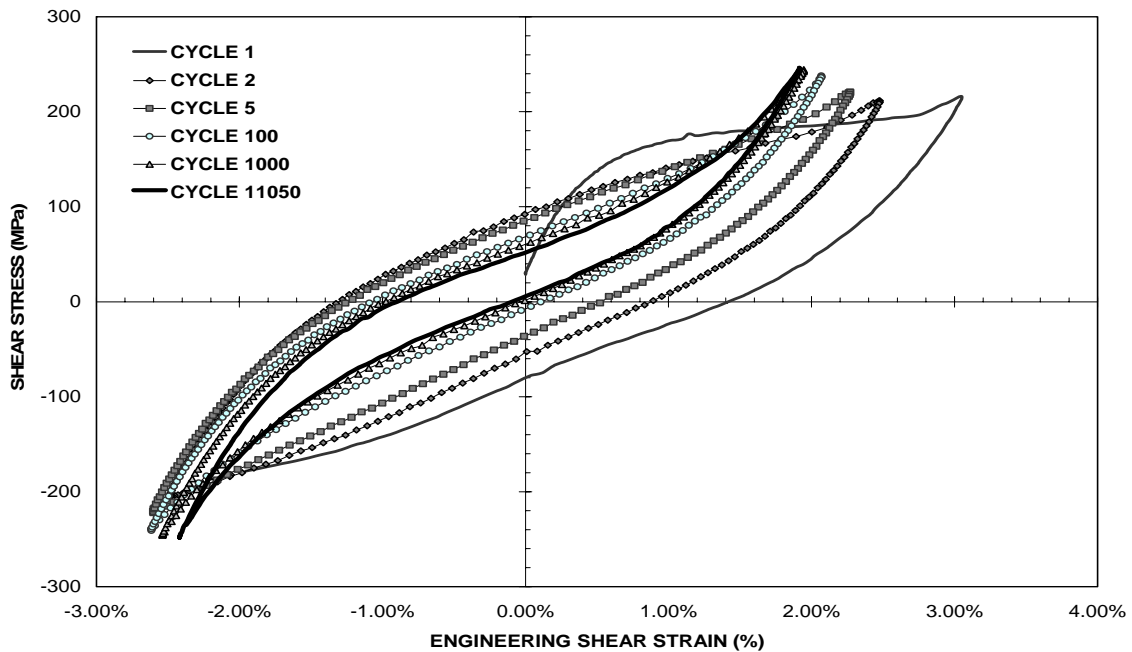


Figure 3-43. Shear stress-strain curves obtained in combined tension-torsion with axial stress range of 500 MPa and shear stress range of 500 MPa.

Evolution of the effective stress-strain hysteresis loop is shown in figure 3-44.

The area inside hysteresis loop decreases as the cycle count increases, with the decrease being more pronounced during the first 1000 cycles.

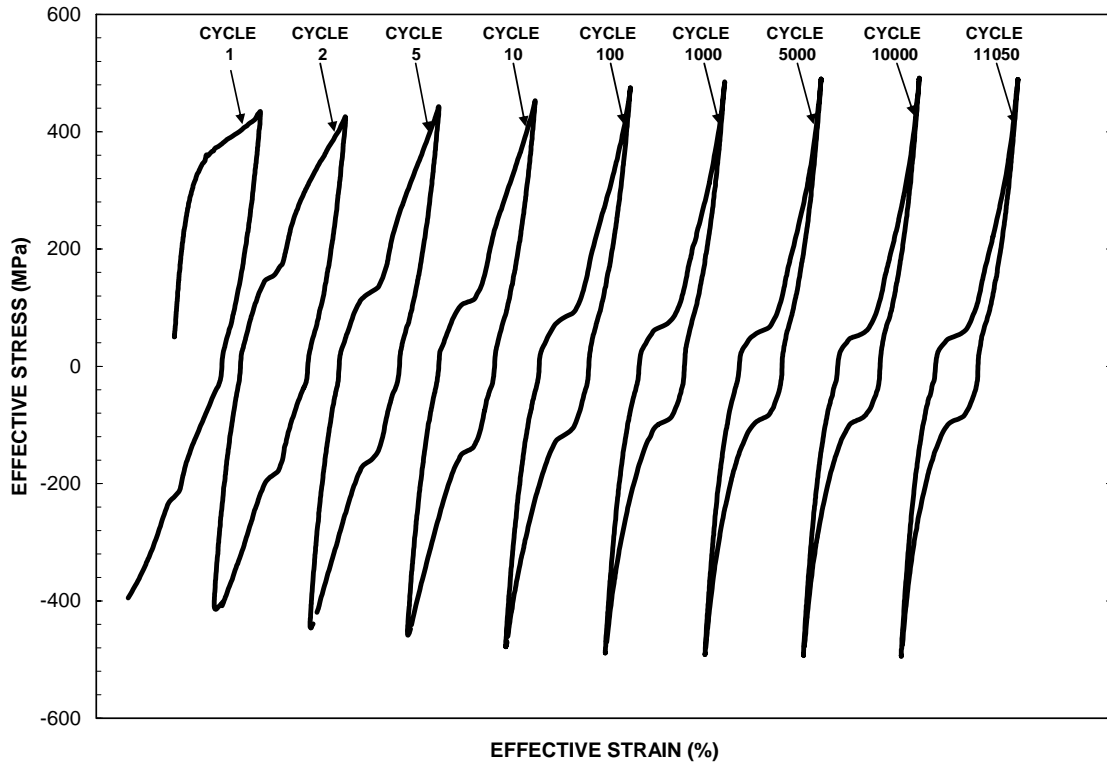


Figure 3-44. Effective stress-strain hysteresis loops obtained in combined tension-torsion fatigue test with an axial stress range of 500 MPa and a shear stress range of 500 MPa. Hysteresis loops for increasing cycles are offset to the right to show changes in shape of loops.

Effective stress-strain curves for selected cycles are shown in figure 3-45. The area within a loop decreases as cycle count increases and is clearly seen in figure 3-45. Maximum effective strain decreases and minimum effective strain increases as cycle count increases. The effective hysteresis loops appear to stabilize after 5000 cycles.

Figure 3-46 shows progression of the maximum and minimum axial strain, engineering shear strain, and effective strain as functions of cycle number.

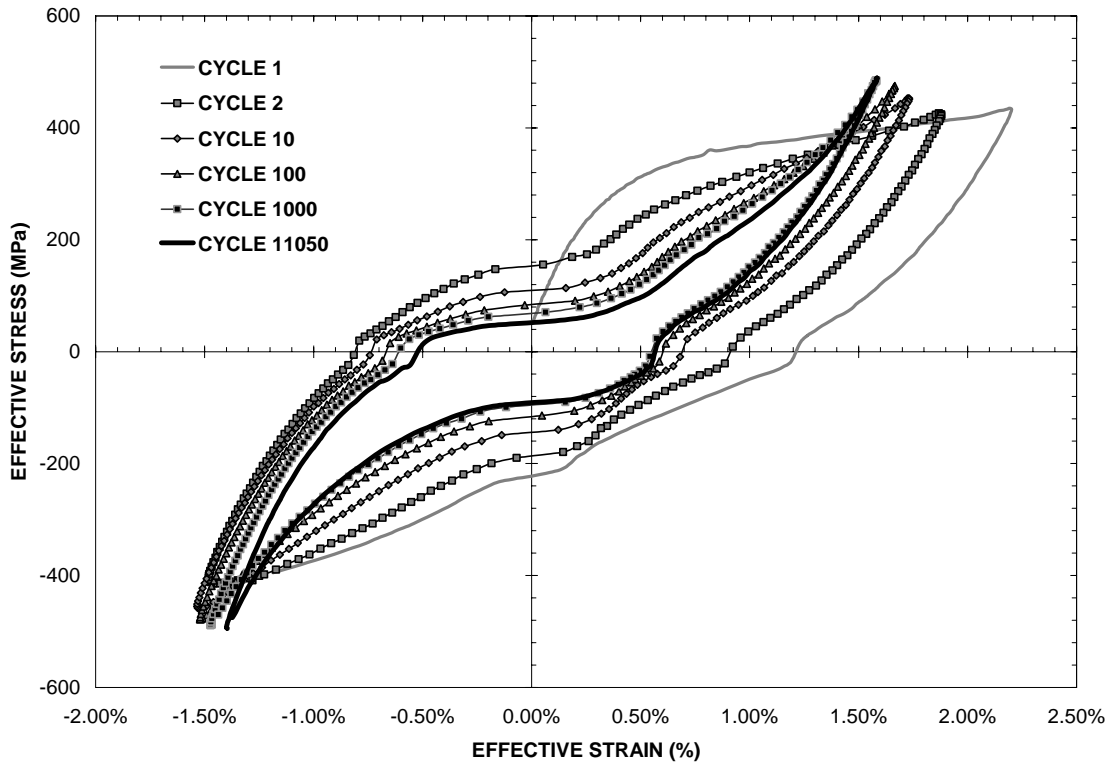


Figure 3-45. Effective stress-strain curves obtained in combined tension-torsion with axial stress range of 500 MPa and shear stress range of 500 MPa.

Maximum axial strain decreases from 1.33% to 1.15% minimum axial strain increases from  $-0.40\%$  to  $-0.10\%$  during cycles 1–11050. The axial strain range decreases from 1.73% to 1.25% over the course of the test indicating cyclic hardening. Maximum engineering shear strain decreases from 3.05% (cycle 1) to 1.91% (cycle 11050). Minimum engineering shear strain decreases from  $-2.35\%$  (cycle 1) to  $-2.62\%$  (cycle 10) and remains stable for the first 1000 cycles. After cycle 1000, the minimum engineering shear strain per cycle increases to  $-2.54\%$  at cycle 11050. The engineering shear strain range drops from 5.40% to 4.33% over 11050 cycles. Once again, cyclic hardening is observed. The maximum effective strain decreases from 2.20% (cycle 1) to 1.58% in the first 1000 cycles and remains stable over the next 10050 cycles. The

minimum effective strain nearly remains constant. The effective strain range decreases from 3.62% (cycle 1) to 2.99% (cycle 11050) indicating slight cyclic hardening.

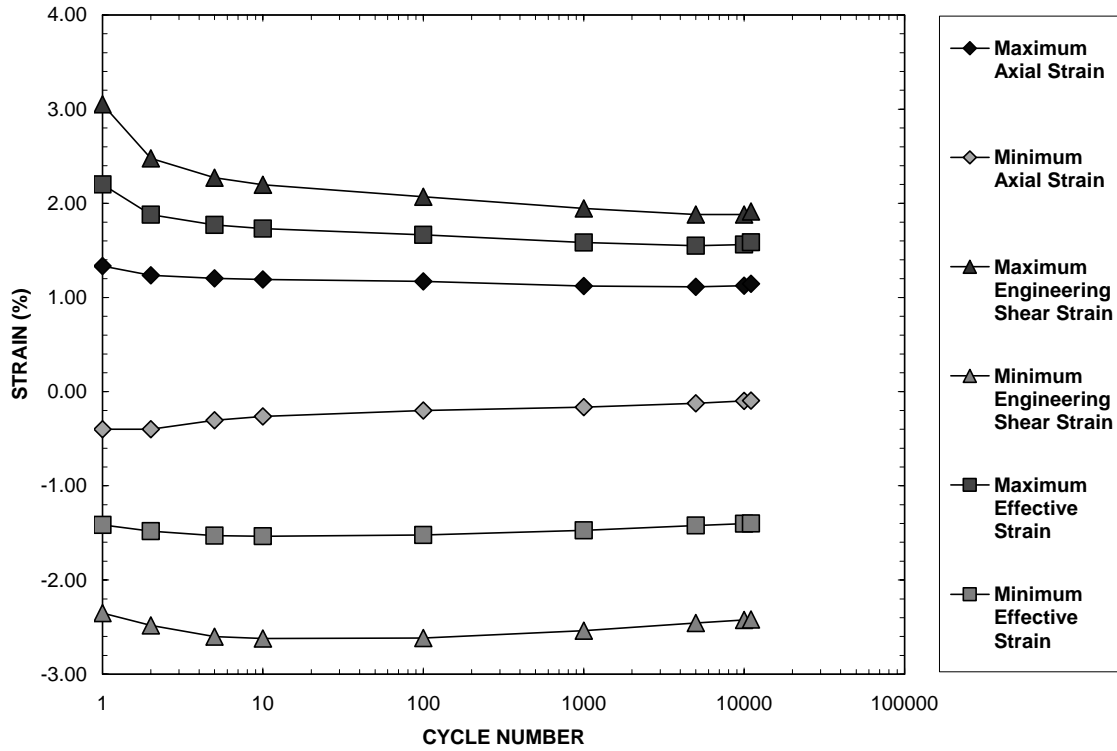


Figure 3-46. Evolution maximum and minimum axial strain, shear strain, and effective strain with fatigue cycles in a fatigue test with axial stress range of 500 MPa and shear stress range of 500 MPa.

### **3.4.5 Combined Tension-Torsion Fatigue, Axial Stress Range = 250 MPa, Shear Stress Range = 500 MPa**

Fatigue test with an axial stress range of 250 MPa and a shear stress range of 500 MPa (von Mises effective stress range = 901 MPa) failed in tension on cycle 37018.

The evolution of the axial hysteresis loops with increasing cycle count can be seen in figure 3-47. The ‘plastic’ strain per cycle,  $\Delta\varepsilon_p$ , and the area inside each hysteresis loop decrease as cycle count increases. The largest reduction in area and  $\Delta\varepsilon_p$  occurs in the first 100 cycles before the loop size and shape stabilize. Only slight reductions in area and  $\Delta\varepsilon_p$  are noted after cycle 100.

The asymmetry of the axial stress-strain behavior is clearly seen in figure 3-48. The asymmetric loops collapse with increasing cycle count. Figure 3-48 also reveals that the slope of the line drawn through peak and valley points of a given cycle increases with cycling.

Shear stress-strain hysteresis loops for selected cycles are shown in figure 3-49. It is seen that the ‘plastic’ engineering shear strain per cycle,  $\Delta\gamma_p$ , and the area inside each hysteresis loop decrease as cycle count increases. The shape of shear hysteresis loops becomes stable at cycle 100. The loops become narrower and the slope of the line drawn through the peak and valley point of a given loop increases with cycling.

Shear stress-strain curves in figure 3-50 demonstrate that cyclic shear stress-strain behavior becomes asymmetric as peak strain decreases and valley strain remains stable in the first 7750 cycles.

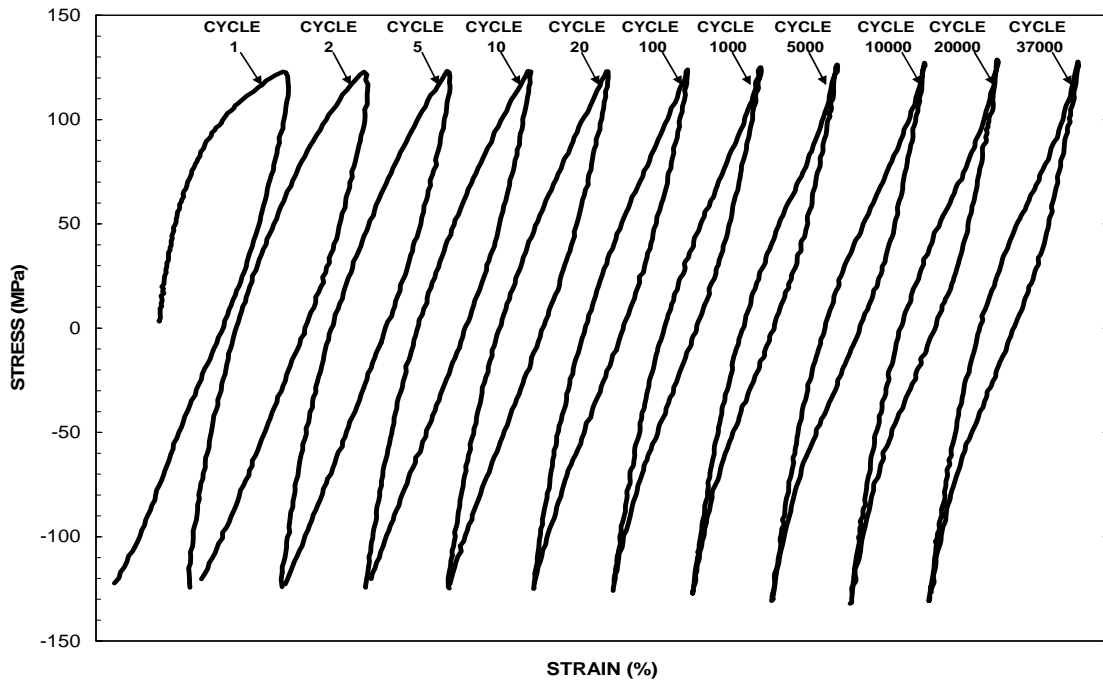


Figure 3-47. Axial stress-strain hysteresis loops obtained in combined tension-torsion fatigue test with an axial stress range of 250 MPa and a shear stress range of 500 MPa. Hysteresis loops for increasing cycles are offset to the right to show changes in shape of loops.

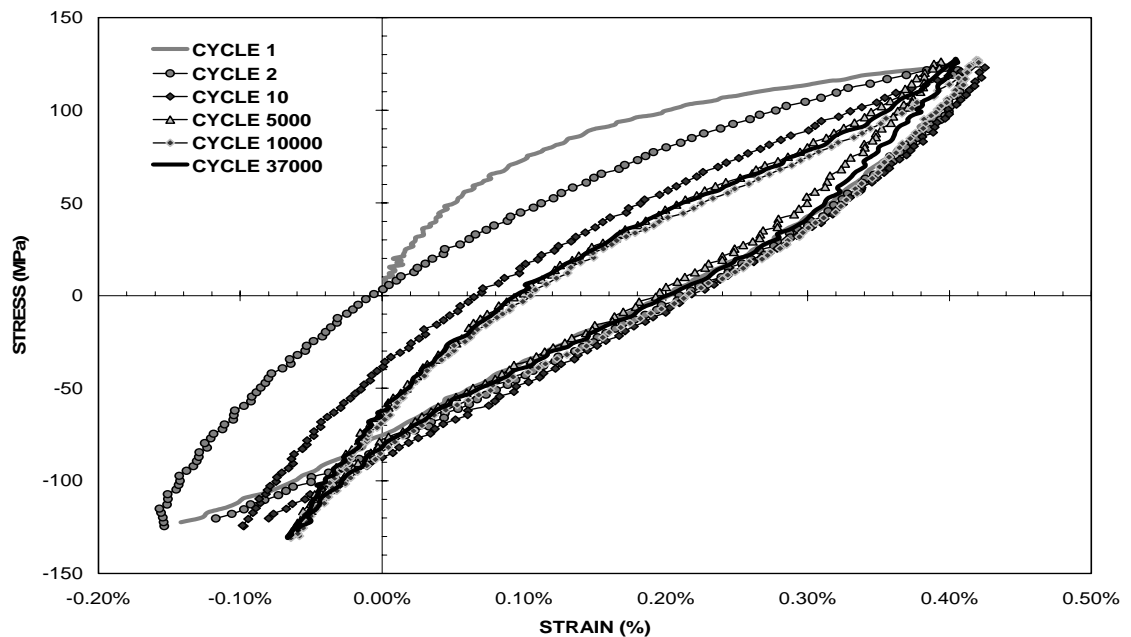


Figure 3-48. Axial stress-strain curves obtained in combined tension-torsion with axial stress range of 250 MPa and shear stress range of 500 MPa.

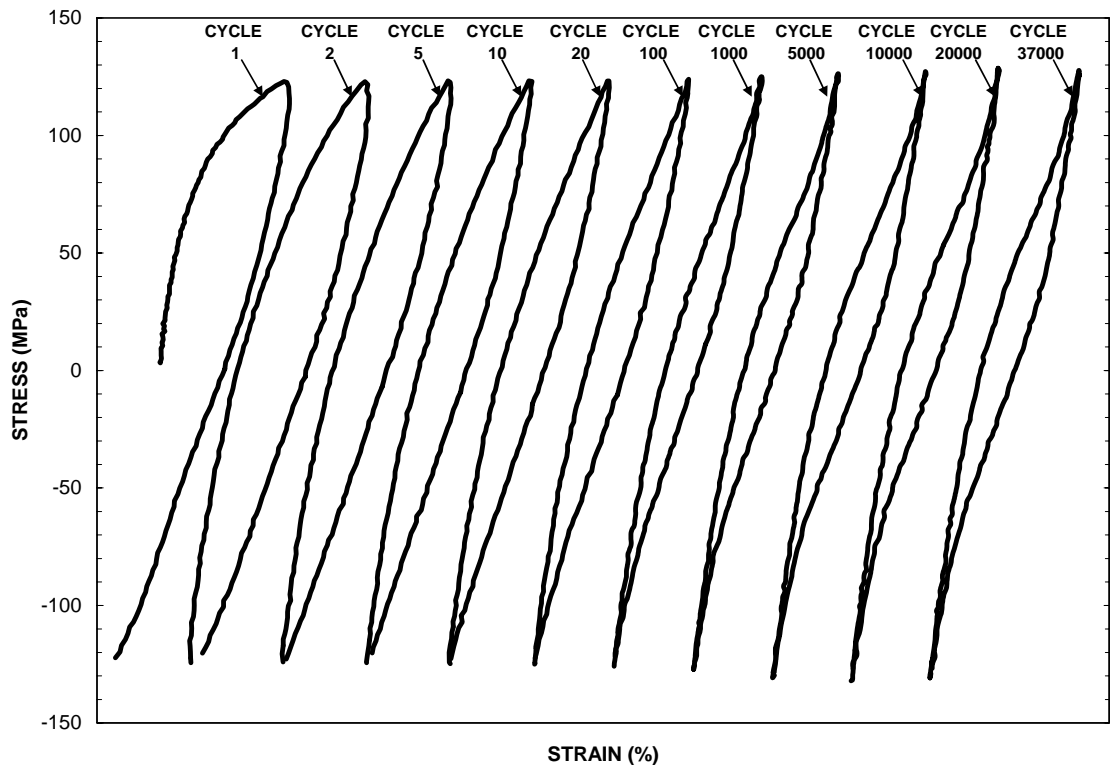


Figure 3-49. Shear stress-strain hysteresis loops obtained in combined tension-torsion fatigue test with an axial stress range of 250 MPa and a shear stress range of 500 MPa. Hysteresis loops for increasing cycles are offset to the right to show changes in shape of loops.

After cycle 7750, the cyclic shear stress-strain behavior becomes less asymmetric as peak strain increases in 300 cycles and valley strain remains stable. Cyclic shear stress-strain behavior becomes asymmetric as peak strain decreases slightly and valley strain remains stable after cycle 8050 as seen in figure 3-51.

Effective stress-strain curves for selected cycles are shown in figure 3-53. The area within a loop collapses as cycle count increases. The maximum effective stress per cycle decreases through the first 5000 cycles and increases and stabilizes at cycle 10000 while the minimum effective stress per cycle remains stable as cycle count increases. The effective hysteresis loops appear to stabilize after 10000 cycles.



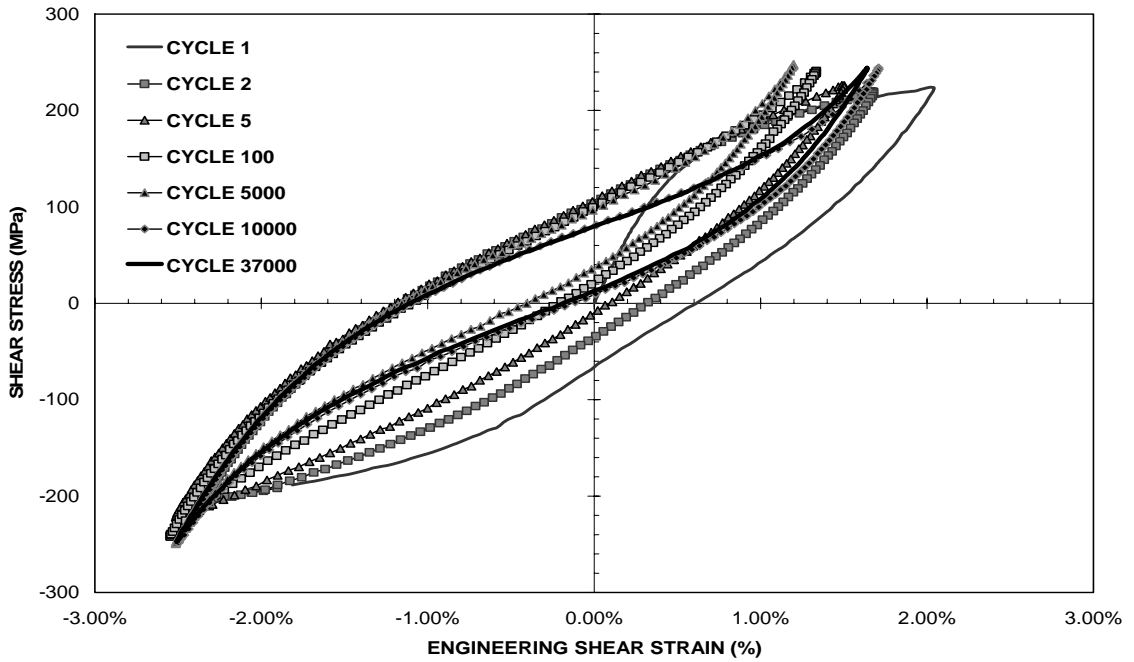


Figure 3-50. Shear stress-strain curves obtained in combined tension-torsion with axial stress range of 250 MPa and shear stress range of 500 MPa.

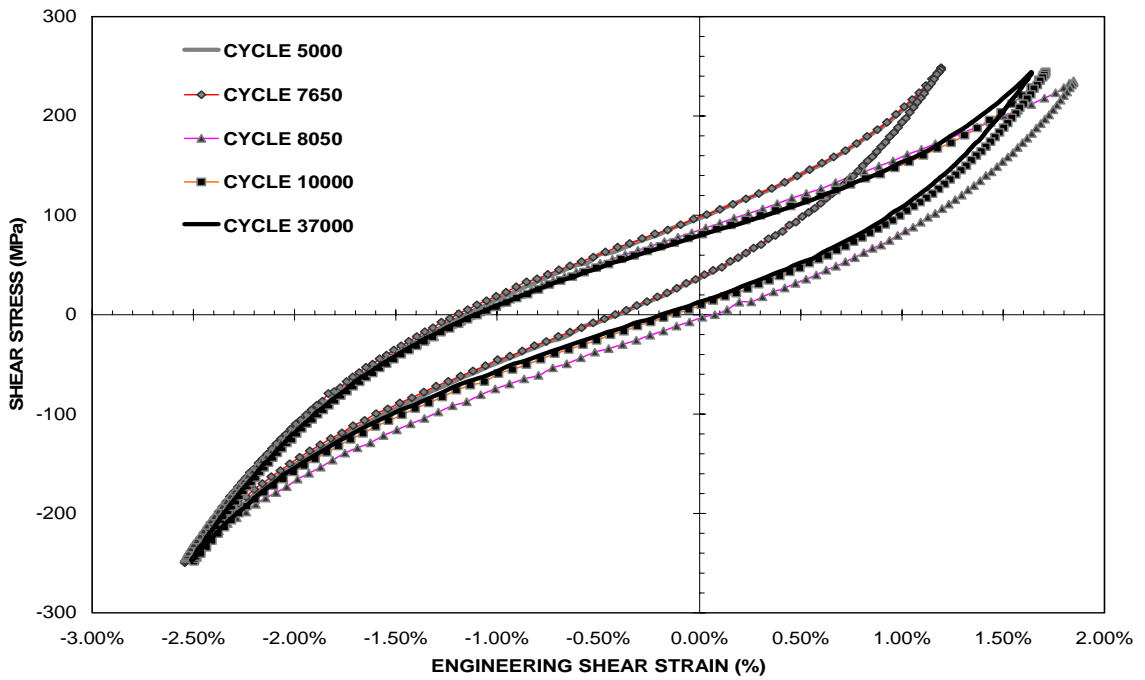


Figure 3-51. Shear stress-strain curves obtained in combined tension-torsion with axial stress range of 250 MPa and shear stress range of 500 MPa. Emphasis on cycle 5000 to cycle 10000.

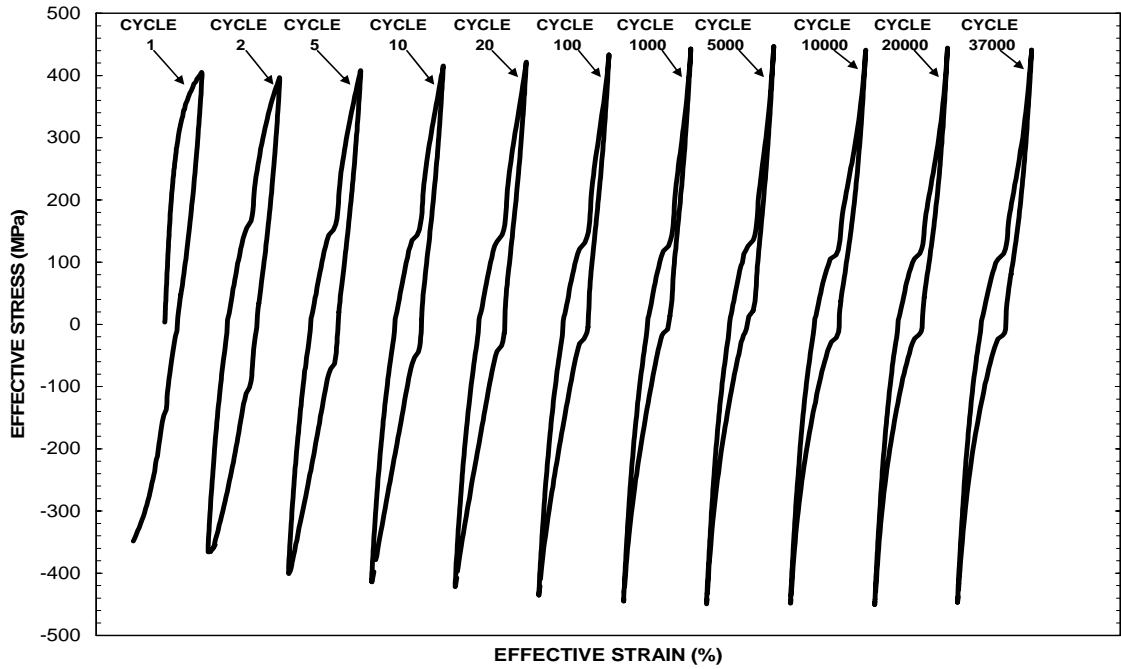


Figure 3-52. Effective stress-strain hysteresis loops obtained in combined tension-torsion fatigue test with an axial stress range of 250 MPa and a shear stress range of 500 MPa. Hysteresis loops for increasing cycles are offset to the right to show changes in shape of loops.

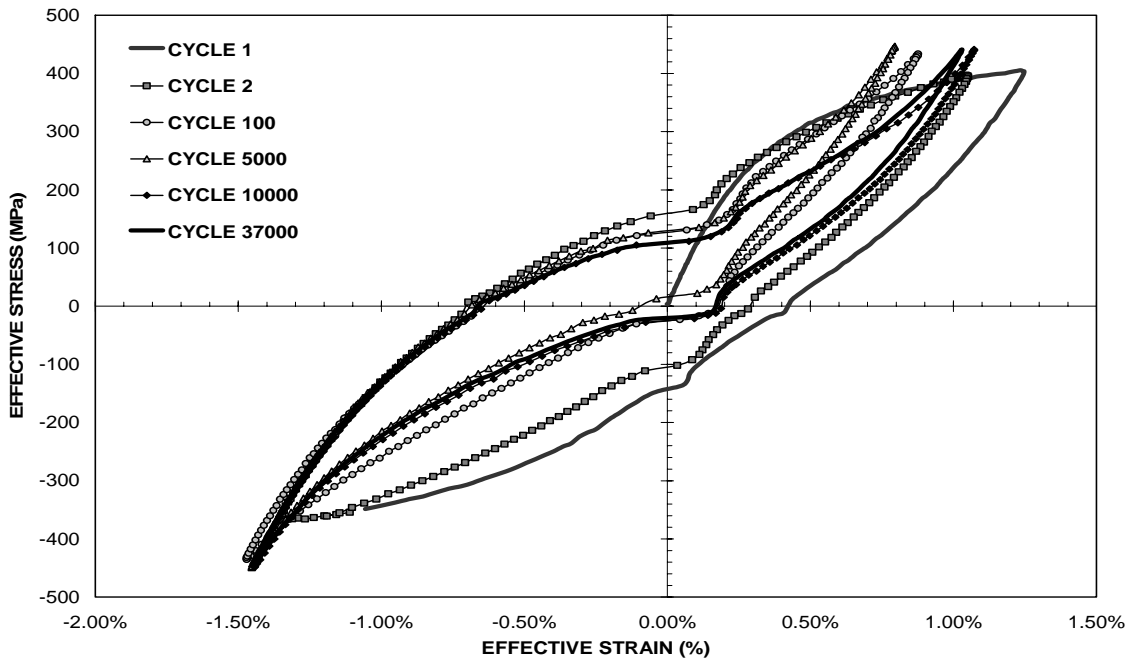


Figure 3-53. Effective stress-strain curves obtained in combined tension-torsion with axial stress range of 250 MPa and shear stress range of 500 MPa.

Figure 3-54 shows progression of the maximum and minimum axial strain, engineering shear strain, and effective strain as functions of cycle number. Maximum axial strain remains stable at 0.41% while minimum axial strain increases from  $-0.16\%$  (cycle 1) to  $-0.07\%$  (cycle 100) before stabilization. The axial strain range decreases from  $0.57\%$  to  $0.48\%$  in the first 100 cycles and remains constant. The maximum engineering shear strain decreases from  $2.04\%$  (cycle 1) to  $1.64\%$  (cycle 3700). The minimum engineering shear strain decreases from  $-2.18\%$  (cycle 1) to  $-2.49\%$  (cycle 20) and remains stable.

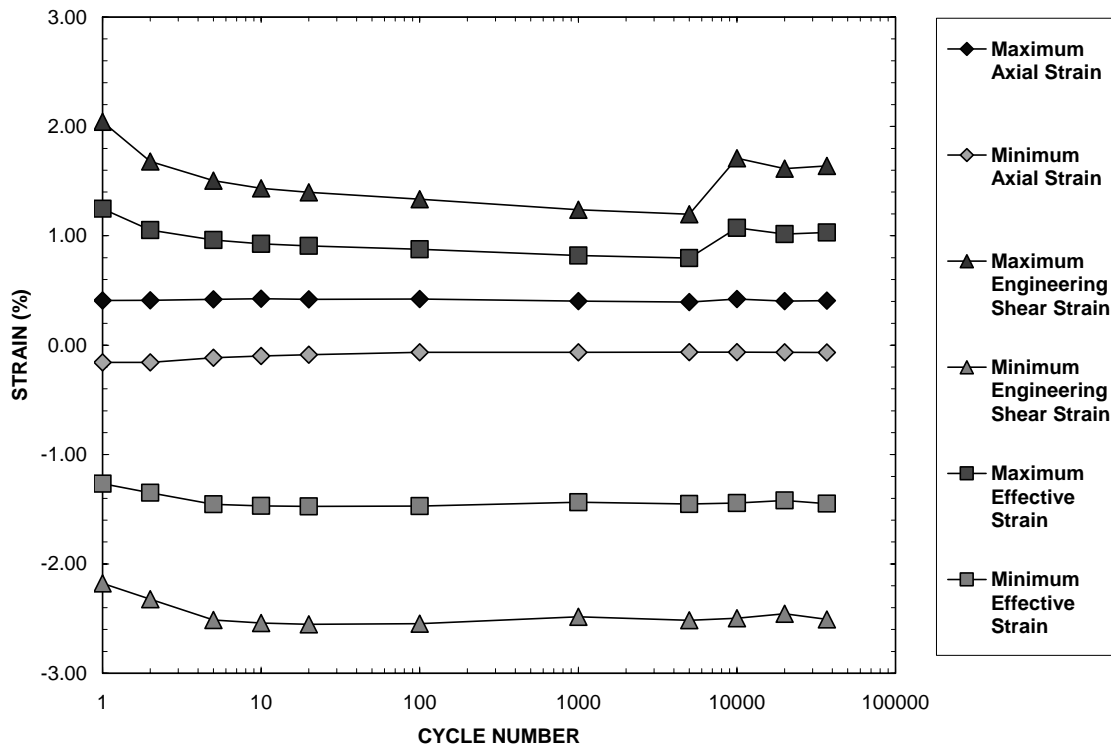


Figure 3-54. Evolution maximum and minimum axial strain, shear strain, and effective strain with fatigue cycles in a fatigue test with axial stress range of 250 MPa and shear stress range of 500 MPa.

The engineering shear strain range drops from  $4.22\%$  (cycle 1) to  $3.71\%$  (cycle 5000). After cycle 5000, the engineering shear strain range jumps to  $4.21\%$  (cycle 10000) but

decreases to 4.15% (cycle 37000) indicating cyclic hardening. The maximum effective strain decreases through the first 5000 cycles before increasing at cycle 10000 and stabilizing. The minimum effective strain remains nearly constant. The effective strain range decreases slightly through cycles 1-37000 indicating slight cyclic hardening.

### **3.4.6 Evolution of Axial Strain Range, Shear Strain Range, and Effective Strain Range in Combined Tension-Torsion Fatigue**

Figure 3-55 shows the axial engineering strain range as function of cycle number for all combined tension-torsion tests. In all tests the axial strain range decreases with cycling indicating cyclic hardening. This trend is most pronounced at higher effective stress range levels. As the effective stress range decreases to 902 MPa, behavior becomes cyclically neutral.

Figure 3-56 shows shear strain range as a function of cycle number for all combined tension-torsion fatigue tests. In all tests the engineering shear strain range decreases with cycling indicating cyclic hardening. This trend is most pronounced at higher effective stress range levels. As the effective stress range decreases to 902 MPa, behavior becomes cyclically neutral.

Figure 3-57 shows effective strain range as a function of cycle number for all combined tension-torsion fatigue tests. In all tests the effective strain range is cyclically neutral.

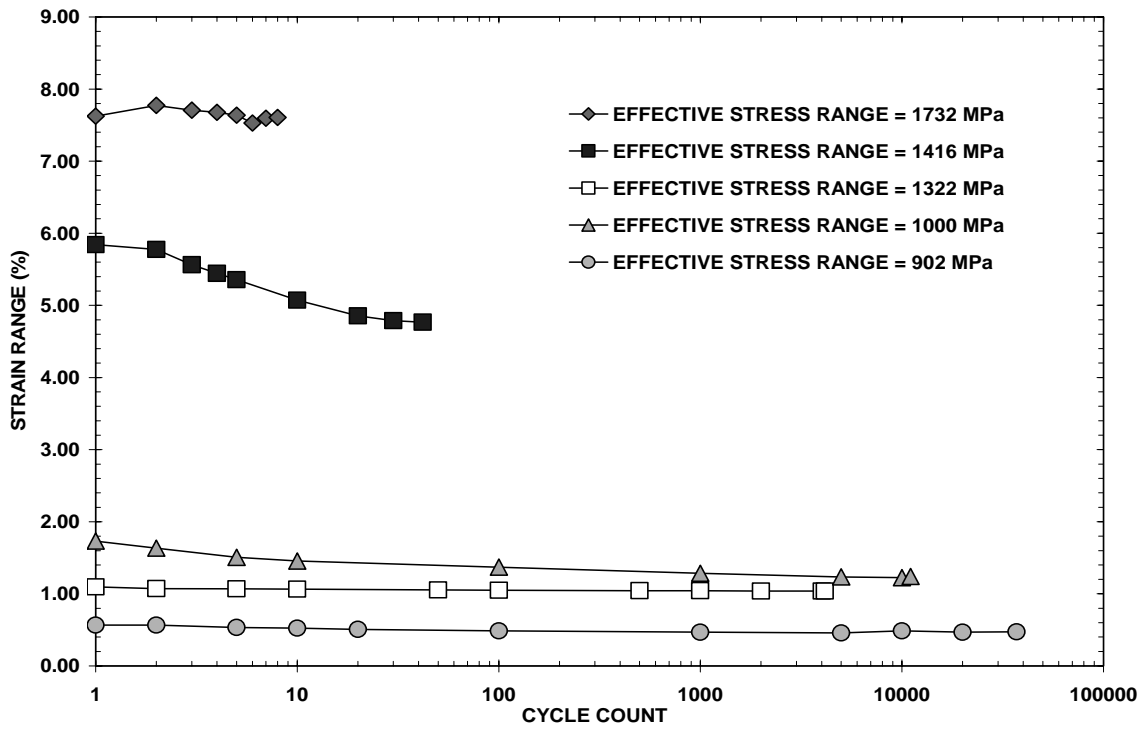


Figure 3-55. Biaxial fatigue axial strain range progression with select cycle count.

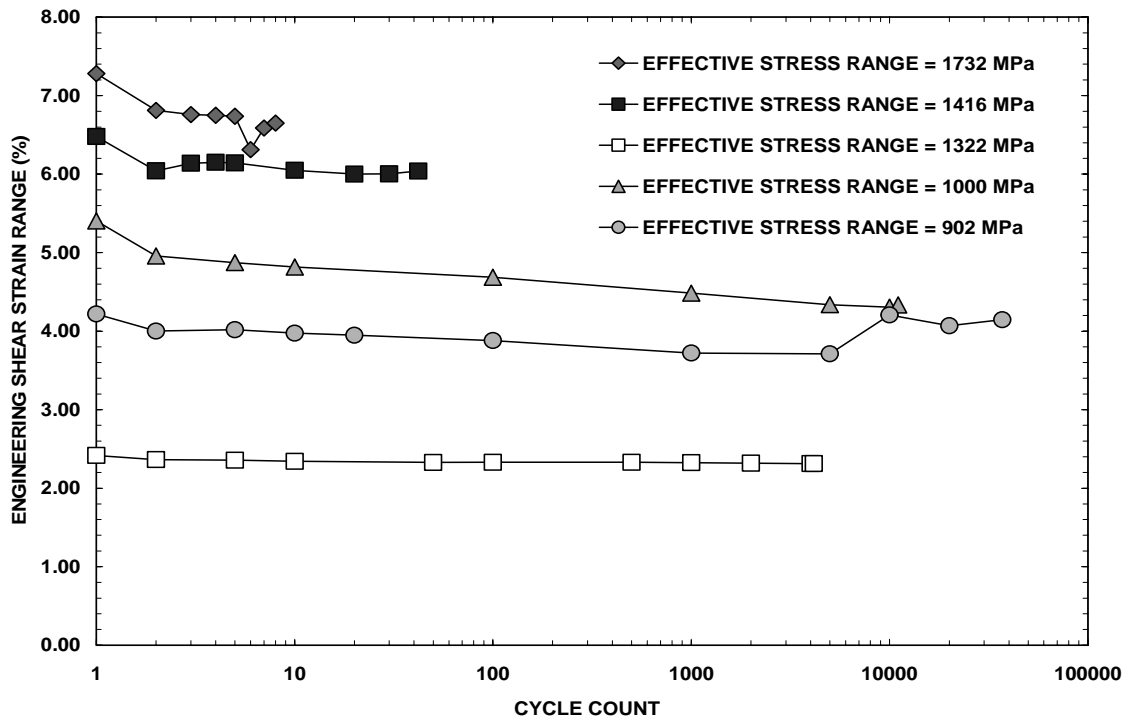


Figure 3-56. Biaxial fatigue torsional engineering shear strain range progression with select cycle count.

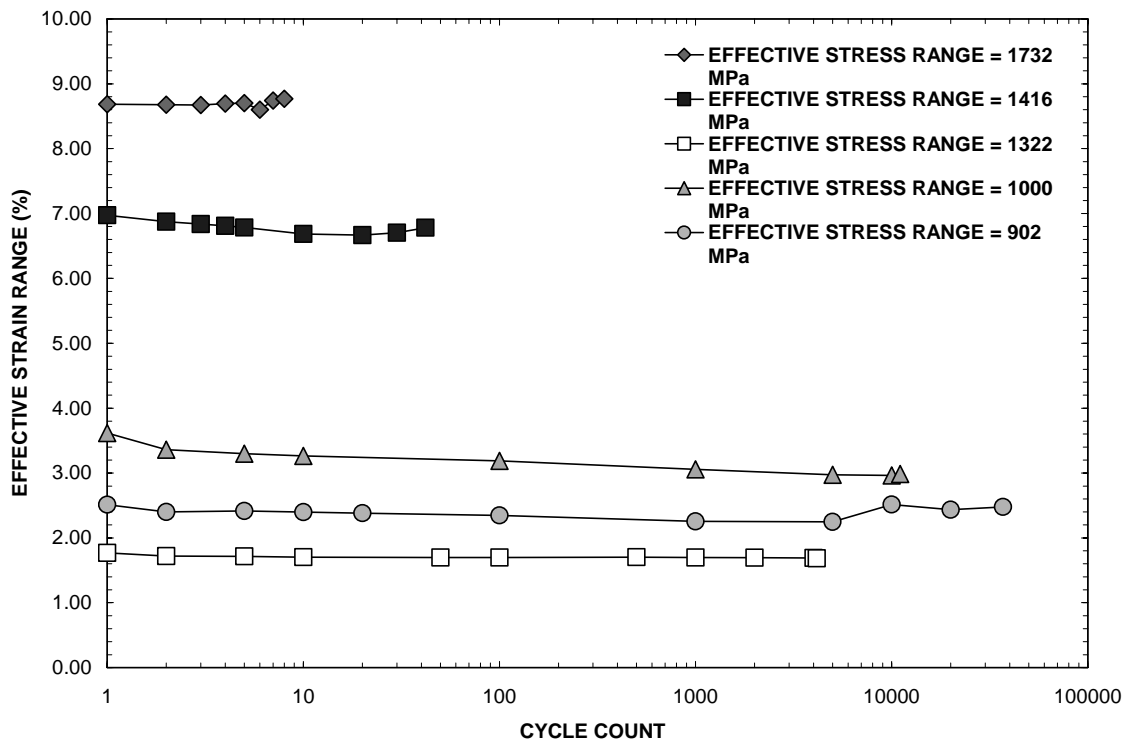


Figure 3-57. Biaxial fatigue effective strain range progression with select cycle count.

### 3.4.7 Comparison of Effective Strain Range Evolution in Pure Torsion Fatigue and in Combined Tension-Torsion Fatigue

Figure 3-58 shows the effective strain range as function of cycle number for all pure torsion (denoted with a “PT”) and combined tension-torsion (denoted with a “CL”) tests. It is immediately noticeable that for a given effective stress range; combined tension-torsion produces higher effective strain ranges than pure torsion fatigue even though pure torsion fatigue resulted in the greatest effective stress range in these experiments. While combined tension-torsion fatigue tests result in cyclically neutral effective stress ranges throughout all tests, pure torsion effective stress ranges decrease

and then increase. This indicates that pure torsion fatigue results in cyclic hardening before experiencing cyclic softening prior to failure. This trend is most pronounced at higher effective stress range levels. As the effective stress range decreases behavior becomes cyclically neutral in both pure torsion and combined tension-torsion fatigue tests.

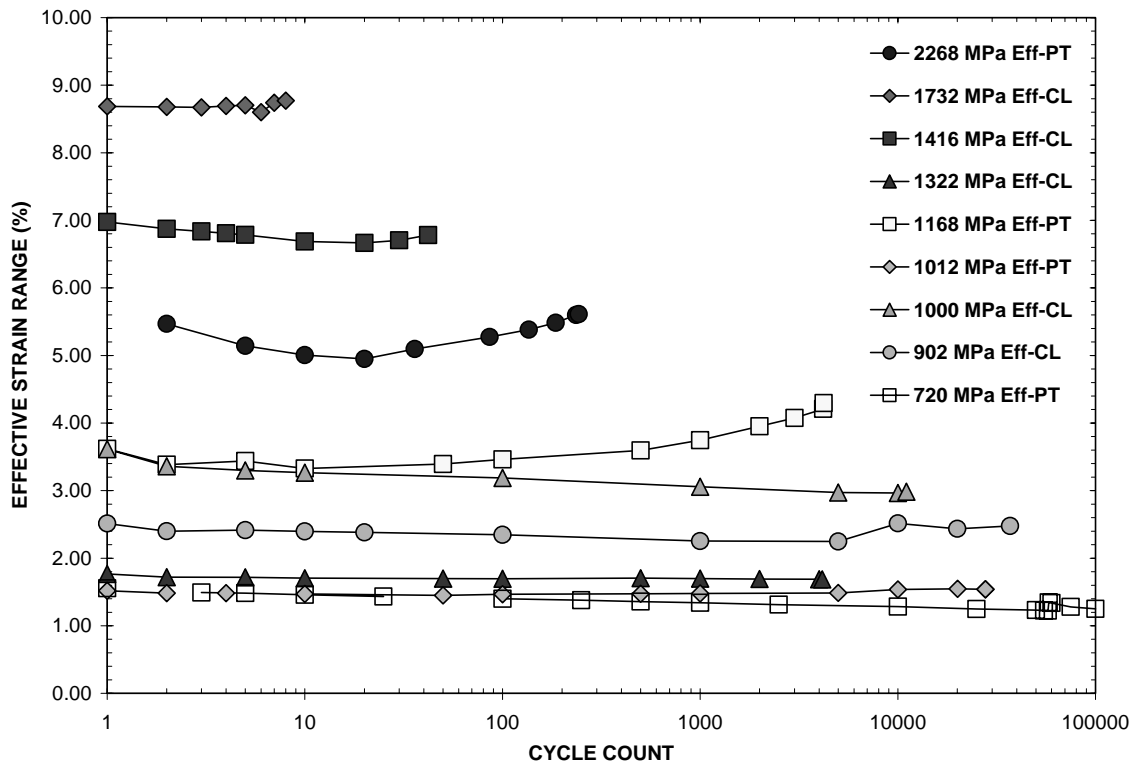


Figure 3-58. Biaxial and torsional fatigue effective strain range progression with select cycle count, where Eff is effective stress, CL denotes biaxial fatigue, PT denotes torsion fatigue, and FL is short for Fatigue Life

The asymmetric behavior and irregular hysteresis loop shapes that decrease in area with cycling seen in both pure torsion and combined tension-torsion will have to be accounted for as researchers develop experiment-based constitutive and life-prediction models. While Nitinol demonstrates cyclically neutral behavior, this material simply cannot be mathematically simulated with classic modeling theories. The asymmetric and

irregular shape phenomena seen in the hysteresis loops make the applicability of pure elastic theory and pure plastic theory impossible. The detailed observations on the mechanical behavior evolution with cycling made here will be a valuable asset in a constitutive modeling endeavor.

### **3.5 Post-Failure Analysis**

This section examines the fracture surfaces obtained in tension, torsion fatigue, tension-dominant biaxial fatigue, and torsion-dominant biaxial fatigue. Tensile failure is indicated by a full specimen crosscut sever that slices perpendicular to the gage length. A cyclic, pure torsion fracture is indicated by an angled 45 degree spiraling crack that winds around the gage section. A parallel crack that propagates along the gage section bridging the angled cracks is also observable in a cyclic, pure torsion failure. A tension-dominant biaxial failure will display characteristics closer to a tensile failure though some torsion failure characteristics can be observed. A torsion-dominant biaxial failure will display characteristics more in line with a cyclic, pure torsion failure, although tensile fracture behavior may also be observed. Photographs of fracture surfaces as well as typical fracture micrographs are presented.



### 3.5.1 Tensile Failure of NiTi SMA

The purpose of this section is to typify failure mechanisms of uniaxial failure. This effort includes brief microstructure analysis of the fracture surface. The location of the SEM micrograph (where applicable) is marked on corresponding pictures. Specimen temperature remained below 43°C (110°F), much lower than the temperature required to trigger a thermal martensite to austenite phase change (19, 29) in NiTi SMA, but it is not known if stress-induced martensite-to-austenite phase changes took place.

The equiatomic NiTi specimen subject to a tensile test failed in the standard form (straight across). Its fracture can be seen in figure 3-59. A close-up of the crack is seen in figure 3-60. At 100x magnification, ridges as seen in figure 3-61a radiate out from the inner surface. Particular troughing is not visible at 500 times magnification (figure 3-61b). Ridges (or martensite “needles”) are visible at higher magnifications in figure 3-61b.



Figure 3-59. Tensile Test Failure

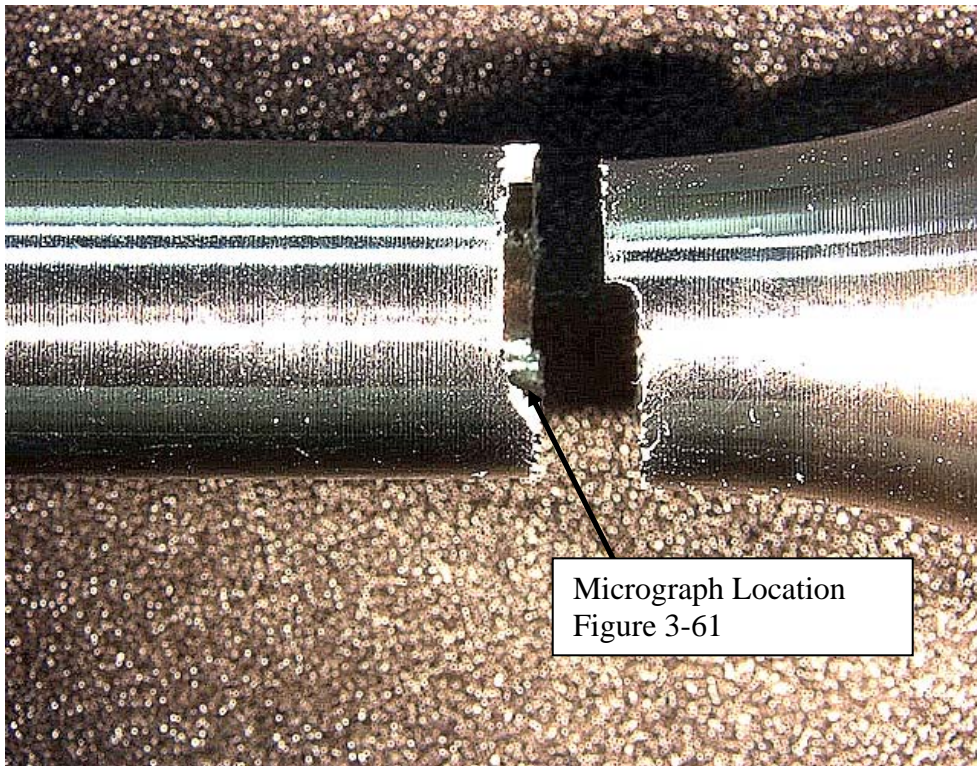


Figure 3-60. Tensile Test Failure Close-up

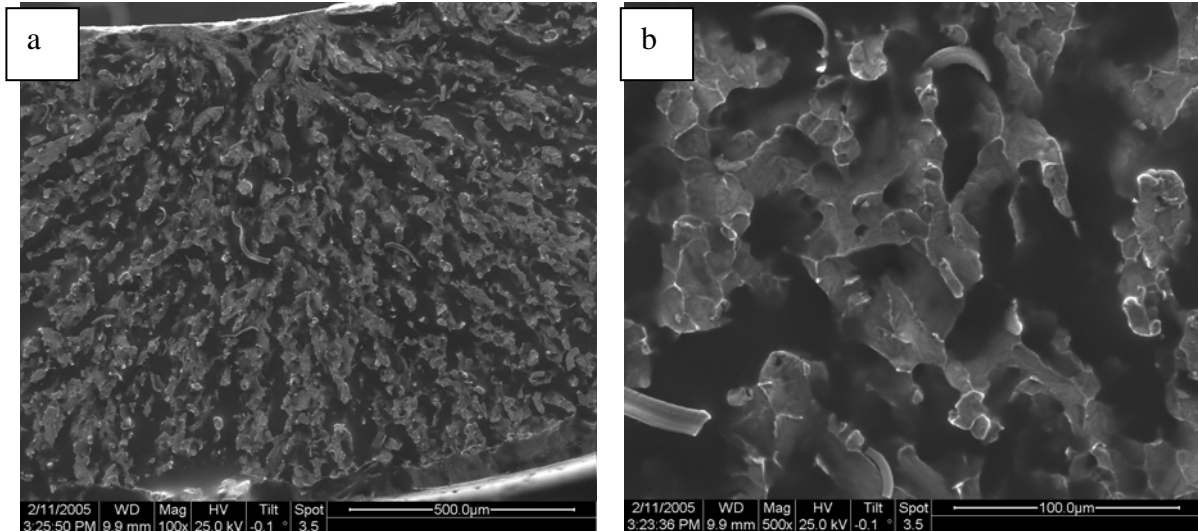


Figure 3-61. Micrograph of tensile failure at 100x magnification (a) and 500x magnification (b). Loading Direction is perpendicular to image. The full width of the thin-walled tube is visible in A.

### 3.5.2 Failure of NiTi in Torsion Fatigue

The purpose of this section is to illustrate failure mechanisms of cyclic, fully-reversed torsional failure. This effort includes brief microstructure characterization of the fracture surface. The location of the SEM micrograph (where applicable) is marked on corresponding pictures. A thermal phase change from martensite to austenite was not expected as recorded specimen temperatures never rose above 43°C (110°F), but it is not known if stress-induced phase changes took place.

A cyclic torsional failure occurred for the extreme case of shear stress range of 1310 MPa. The shear fracture is seen to completely sever the specimen in figure 3-62. A 45° crack is seen on the left that eventually splits and creates a valley where the specimen separated. A crack that propagates parallel to the gage section is visible on the right of figure 3-62.

The 673 MPa shear stress range fracture did not sever the specimen. Instead, a twisting 45° crack is visible in figure 3-63 that wraps around the gage section with a short section that runs parallel to the gage section in the middle. The micrographs reveal a troughing V-shape across the thin wall (figure 3-64a) along the angled portion fracture surface. It has been shown in literature that SMA wire subjected to loading and unloading in pure bending rearranges martensite plates in a similar V-shape pattern (22). Longer, more drawn out islands than seen in tensile failure oriented along the V-troughs are better seen at 250x magnification as observed in figure 3-64b. The parallel fracture surface caused by pure torsion cycling is shown in figure 3-65. Large, flat, shale-like islands dominate along troughs that run parallel to the gage section.

The fracture caused by a shear stress range of 1012 MPa can be seen in figure 3-66. A similar, torsional 45° twisting crack that spans the gage section is visible here but does not include a parallel portion as noted in higher shear stress ranges.

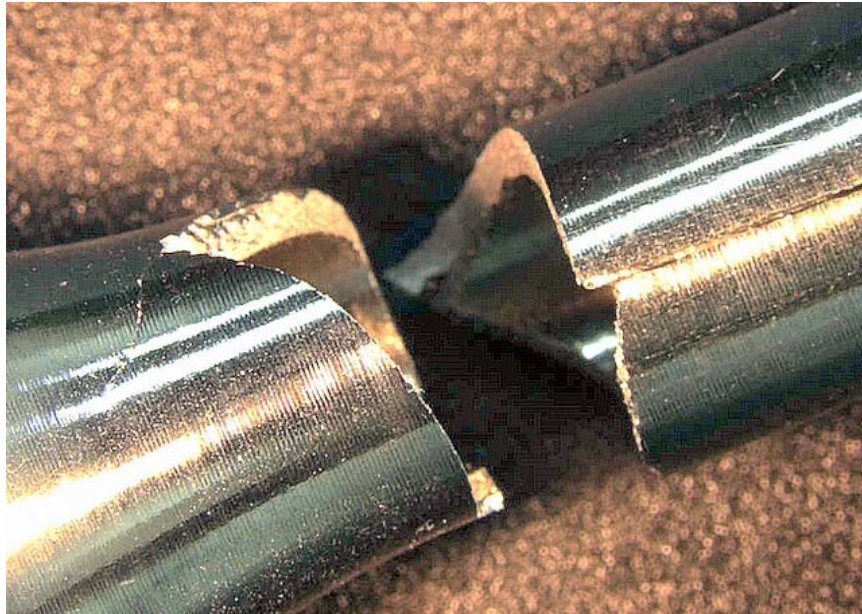


Figure 3-62. Pure Torsion 1310 MPa Shear Stress Range (2269 MPa Effective Stress Range) Failure

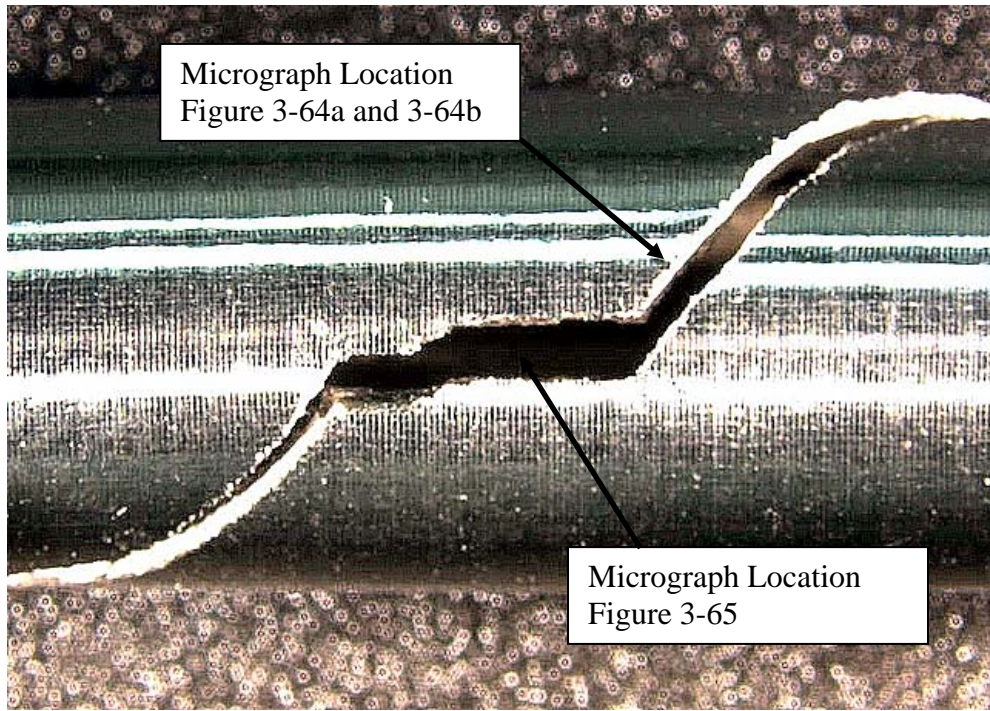


Figure 3-63. Pure Torsion 674 MPa Shear Stress Range (1167 MPa Effective Stress Range) Failure

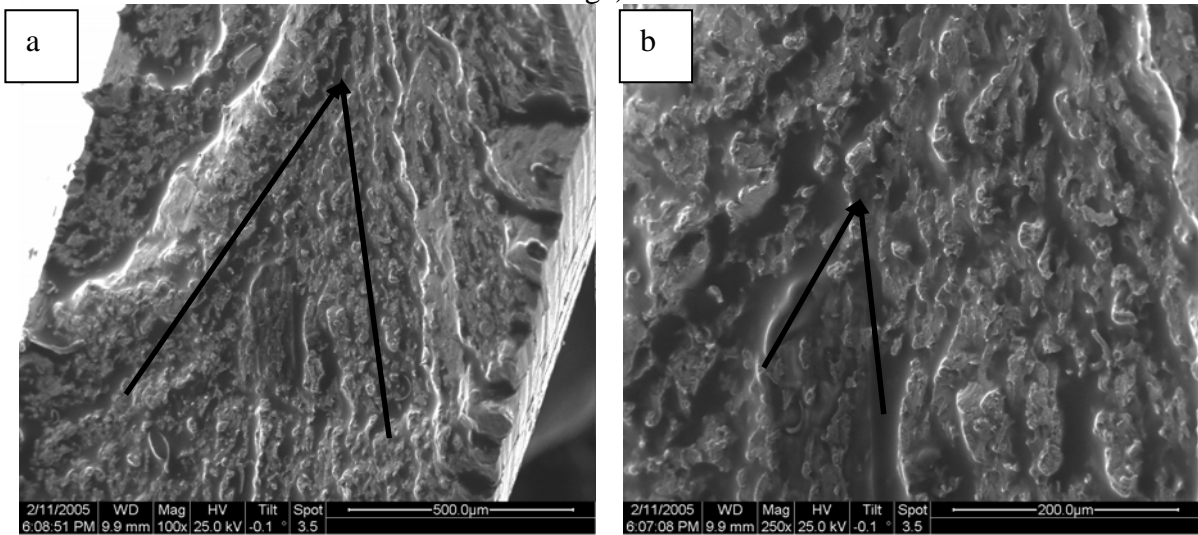


Figure 3-64. Micrograph of cyclic torsion angled fracture at 100x (A) and 250x (B) magnification. The full width of the thin-walled tube is visible in 4.5-7a. The black arrows mark out V-shaped troughs meeting in the center of the thin-walled tube.

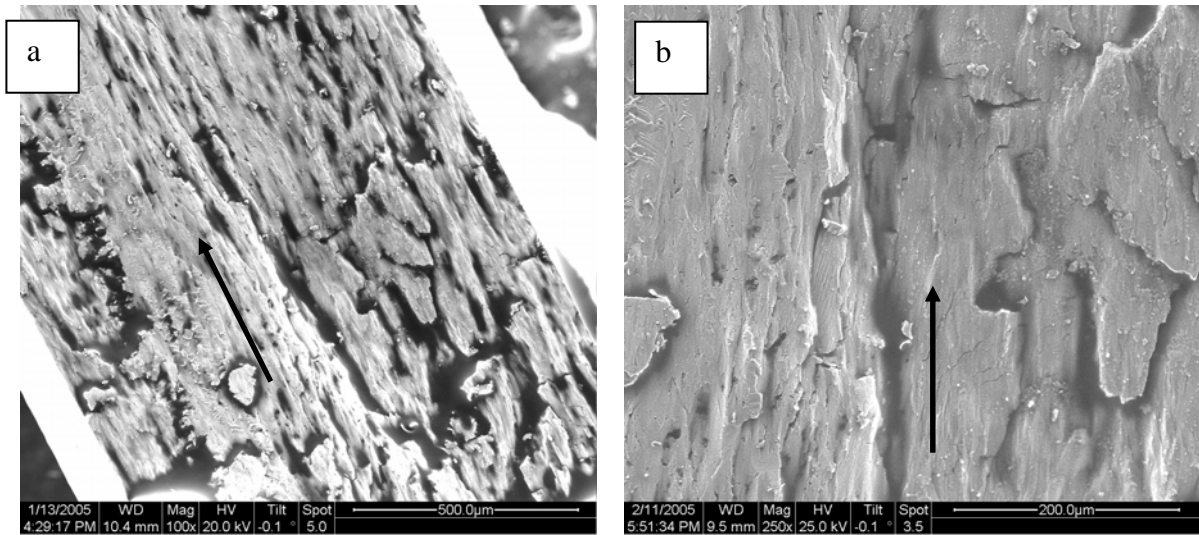


Figure 3-65. Micrograph of cyclic torsion parallel fracture at 100x (a) and 250x (b) magnification. The full width of the thin-walled tube is visible (a). The black arrows mark out circumferential troughs in the thin-walled tube.

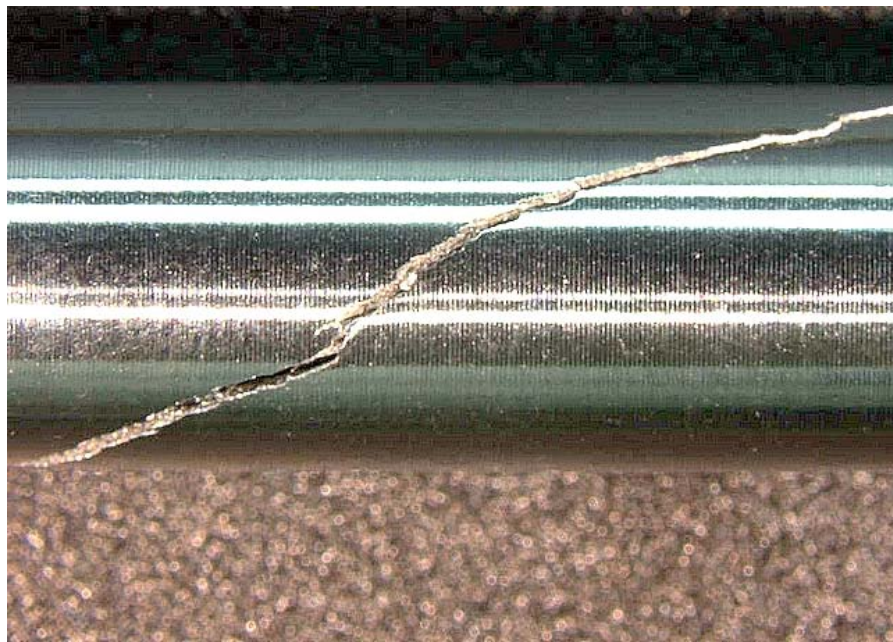


Figure 3-66. Pure Torsion 584 MPa Shear Stress Range (1012 MPa Effective Stress Range) Failure

### 3.5.3 Cyclic Bi-axial Failure

The purpose of this section is to draw comparisons of the bi-axial failure to either tensile failure or cyclic torsional failure. This effort includes brief microstructure analysis of the fracture surface as it can be compared to either typical tensile or typical cyclic torsional failure. Comparisons of tensile-dominant and torsion-dominant failures are made through analysis and characterization of failure types. The location where the SEM micrograph was taken is marked on the corresponding picture where applicable. A thermal phase change from martensite to austenite was not expected as specimen temperatures never rose above 110°F, but it is not known if stress induced phase changes took place.

Specimen tested with the largest bi-axial effective stress range, 1732 MPa, failed across the gage section with slight torsional tearing. The tensile-dominant fracture occurred in across the gage section with slight torsional tearing noted. A pure tensile failure would have generated a pure crosscut failure as seen in figure 3-60. A spiraled, angled fracture would be expected to be seen in a torsional failure. Angled fractures spiraling away from the failure section are not visible in this failure (figure 3-67).

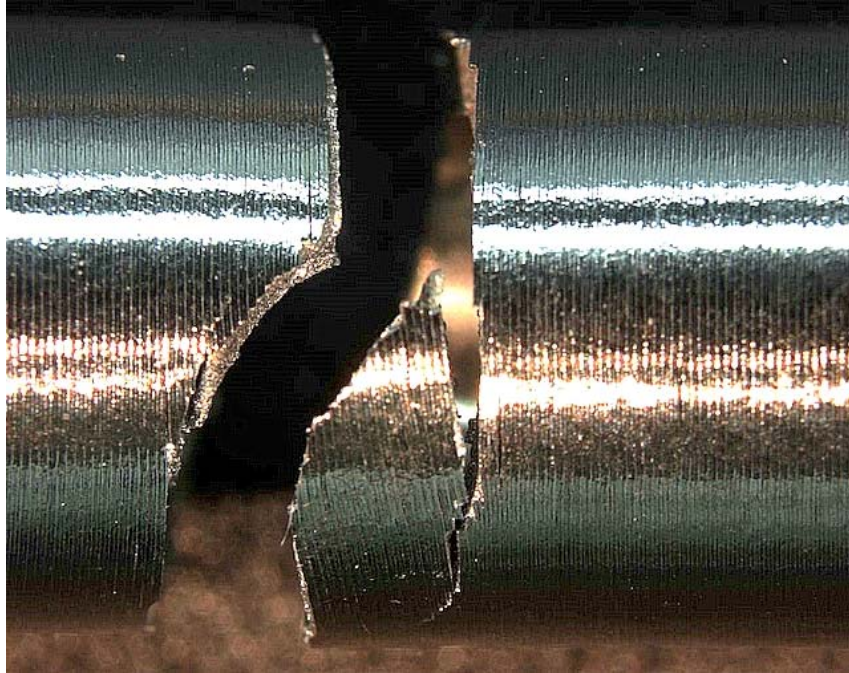


Figure 3-67. Combined 1500 MPa Stress Range with 500 MPa Shear Stress Range Failure(1732 MPa Effective Stress Range)

Specimen tested with the next largest effective stress range, 1416 MPa, also failed across the gage section. However, the amount of torsional tearing is increased as noted by larger sections of angled crack propagation. The sever seen in figure 3-68 does not cut straight through the specimen as is seen in a tensile failure, but rather is offset in a spiral fashion suggesting more contribution to the failure from shear stress than seen in the very tensile-dominant effective stress range of 1732 MPa. The fact that the crack propagation does not spiral past the fracture surface into the far ends of the gage section suggest that the failure is still prominently tensile. The micrographs seen in figure 3-69 do not show strong trough features as seen in pure torsion cyclic failures. However, drawn-out islands as seen cyclic torsional fractures (figure 3-64) hint toward an angled flow from the inner surface to the outer surface. The lack of dominant troughs hint



towards a tensile-dominant failure, but drawn-out, shapely islands that flow away from the fracture apex make ruling out torsional influence impossible.

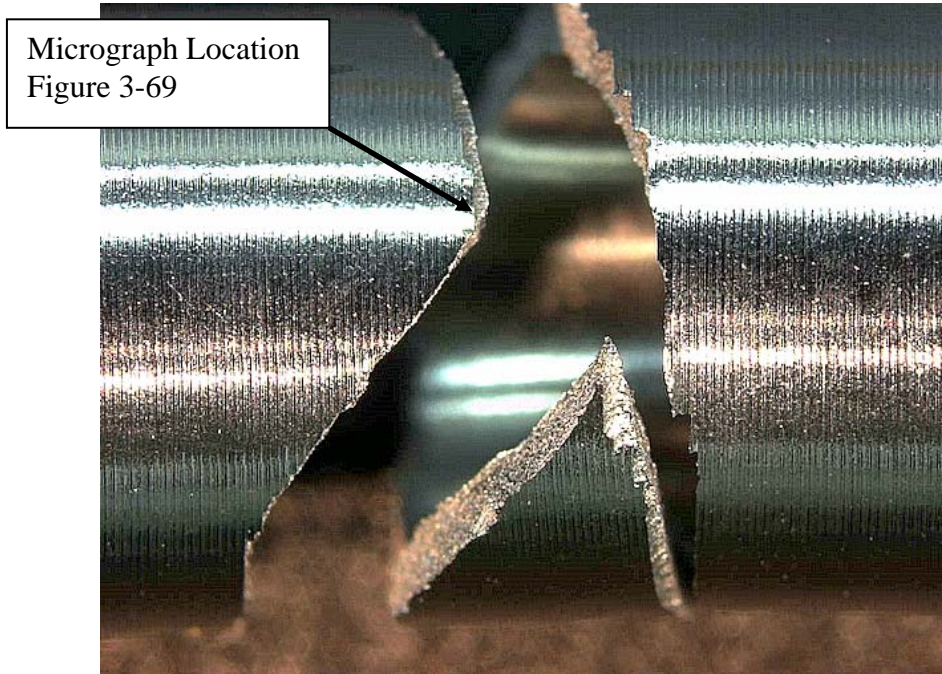


Figure 3-68. Combined 1120 MPa Stress Range with 500 MPa Shear Stress Range Failure (1416 MPa Effective Stress Range)

A more pronounced spiraling in the cross-sectional failure is observed in figure 3-70 caused by the bi-axial effective stress range of 1323 MPa. Still, the fracture is dominated by tensile failure, as no spiraling cracks are seen propagating away from the fracture. The angling of the cross-sectional failure is the largest observed of the bi-axial tests with effective stress ranges of 1732, 1416, and 1323 MPa.

The effective stress range of 1000 MPa produced angled cracks that appear to propagate along the gage section at a 45° angle. While the specimen did separate as seen in figure 3-71 with what appears like an angled tensile failure, a crack is clearly visible

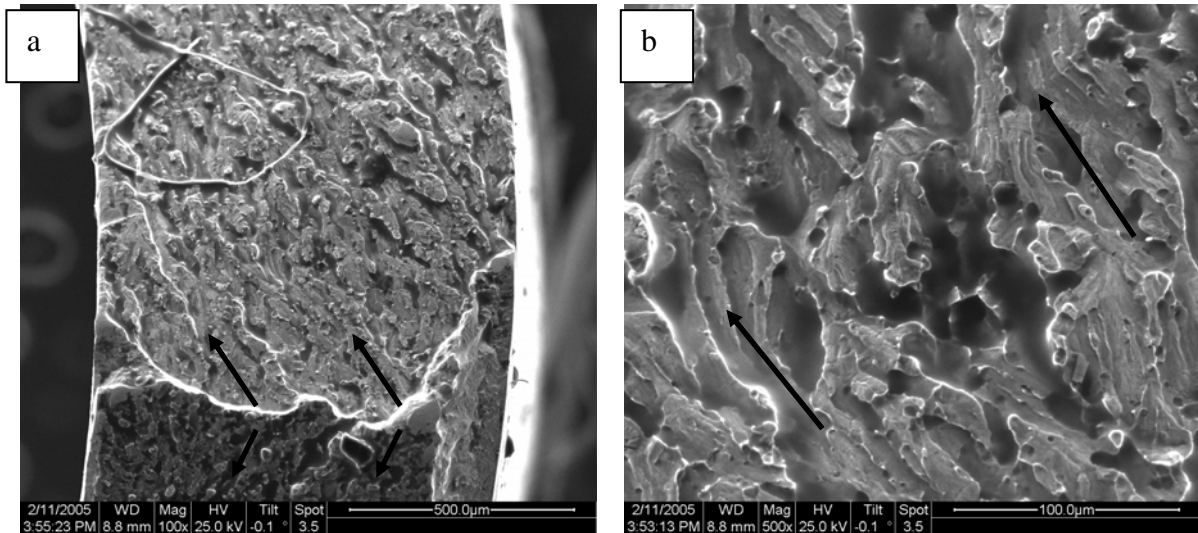


Figure 3-69. Micrograph of combined tension-torsion cyclic fracture at 100x (a) and 500x (b) magnification. The full width of the thin-walled tube is visible in 4.5-10a. Arrows point out apparent trough flow away from the apex.

that propagated along the gage section at a  $45^\circ$  angle away from the separating cross-sectional failure. The presence of the angled crack suggests a failure mechanism akin to torsional cyclic loading while the complete cross-sectional (although angled) crack suggests tensile failure. This fracture does not appear to be particularly dominated by either tension or torsion. It is interesting to note that the 1000 MPa effective stress range was achieved by combining numerically equal ranges of 500 MPa in stress and shear stress.

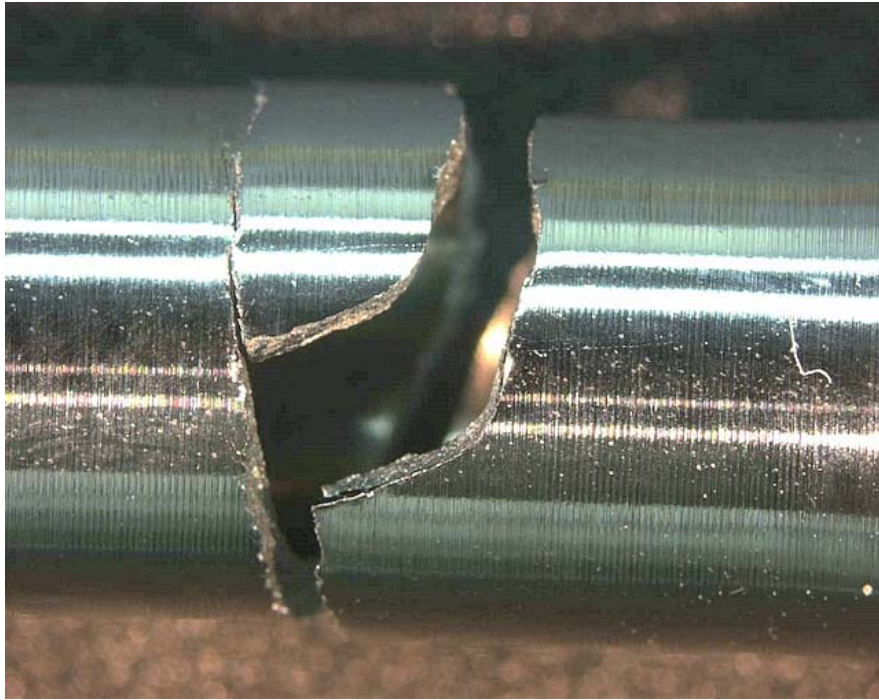


Figure 3-70. Combined 1000 MPa Stress Range with 500 MPa Shear Stress Range Failure (1323 MPa Effective Stress Range)

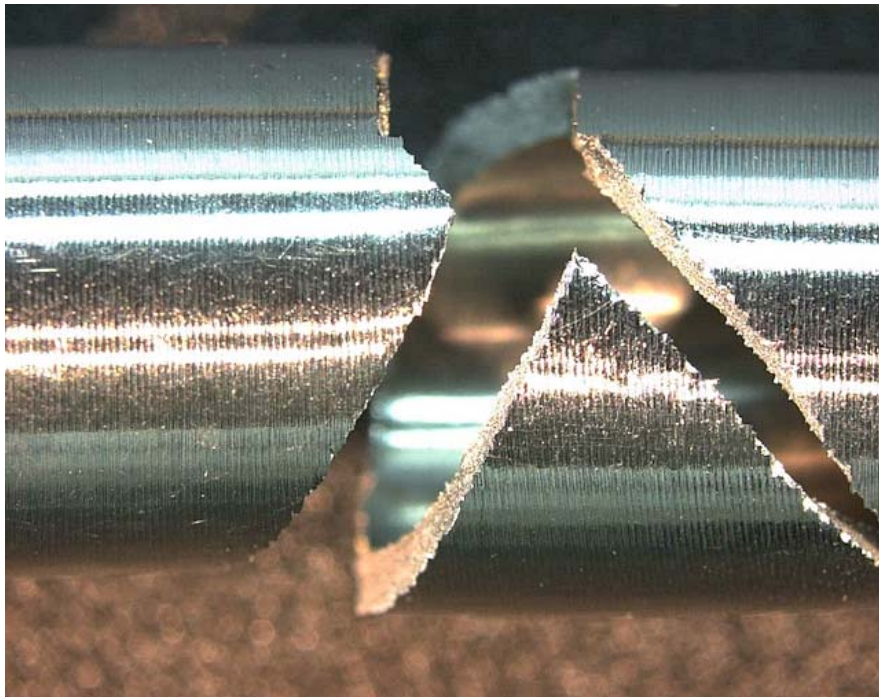


Figure 3-71. Combined 500 MPa Stress Range with 500 MPa Shear Stress Range Failure (1000 MPa Effective Stress Range)

Tensile failure is evident as the specimen did separate across the gage section. This angled cross-sectional fracture can be seen on the left side of the figure. Torsional failure is clearly observable as a 45° crack is seen spiraling along the gage section with a short fracture surface that is parallel with the gage section. This torsional crack looks very much like the cyclic torsional failure seen in figure 3-63. The area of the specimen that failed across the gage section presented in figure 3-73 resembles a tensile failure as the micrographs show slight troughs and is populated by numerous small islands. The slight depressions suggest a circumferential flow that curves outward eventually connecting the outer edge to inner edge. Figure 3-74 shows the torsional angled fracture that spirals along the spine. Here, torsional V-troughs are clearly observable that points along the torsional fracture away from the tensile sever. The parallel fracture seen in figure 3-75 is strikingly similar to the pure torsional cyclic failure seen in figure 3-64. In the case of biaxial fracture, this parallel fracture demonstrates parallel troughs to the gage section and large, flat, shale-like islands govern the fracture surface. Figure 3-76 shows the area where the parallel crack transitions to an angled fracture that continues spiraling along the gage section. Slight trough flow is noted starting on the inside edge and flowing outward and away from the transition point of parallel fracture to angled fracture.

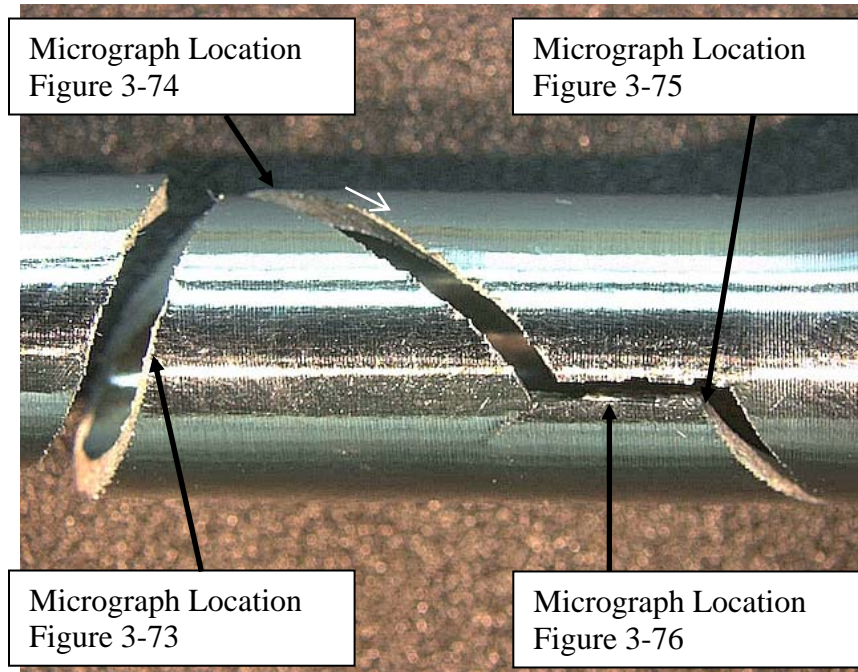


Figure 3-72. Combined 250 MPa stress range with 500 MPa shear stress range failure (901 MPa effective stress range). Micrograph locations are marked with arrows as well as the direction of the V-troughs on the fracture surface.

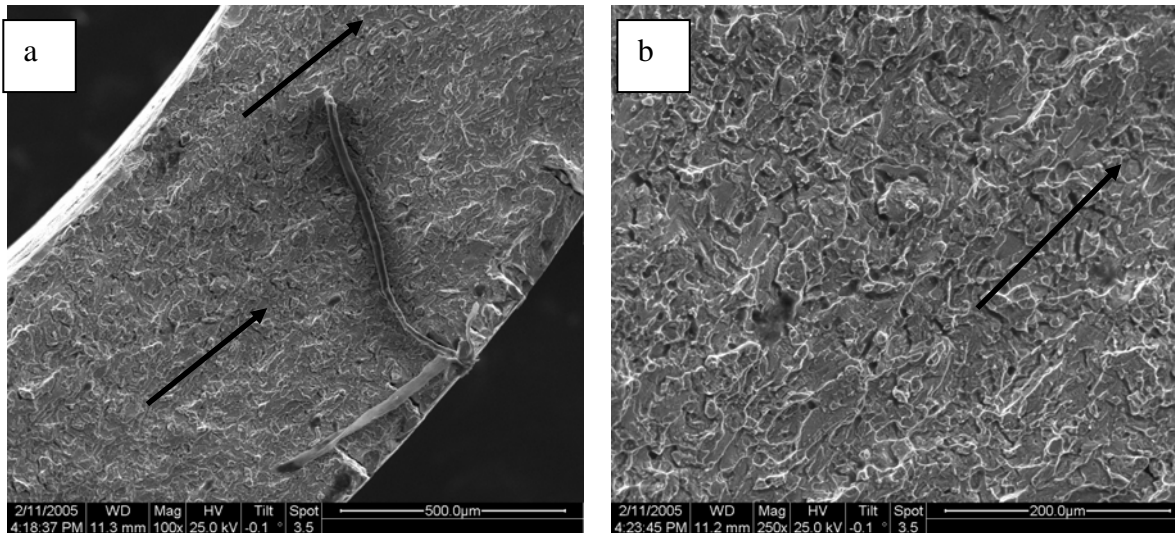


Figure 3-73. Micrograph of combined tension-torsion 901 MPa effective stress range tensile-area fracture at 100x (a) and 250x (b) magnification. The full width of the thin-walled tube is visible in 3-72a. Arrows point out suggest trough direction

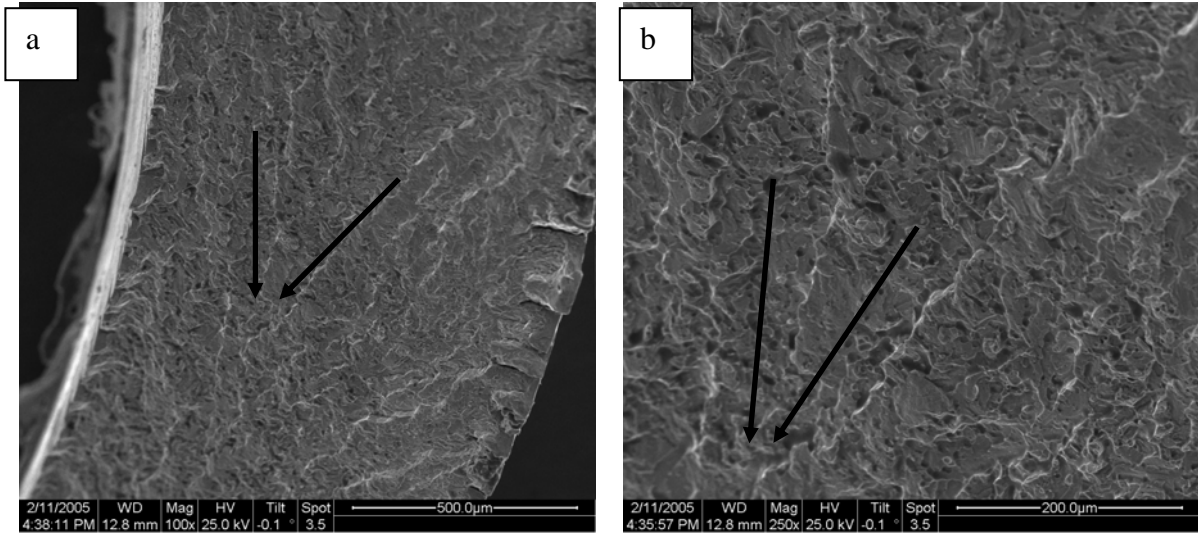


Figure 3-74. Micrograph of combined tension-torsion 901 MPa effective stress range angled fracture surface at 100x (a) and 500x (b) magnification. The full width of the thin-walled tube is visible in 3-73a. Arrows point out apparent V-trough flow away from the tensile failure and towards the parallel fracture area.

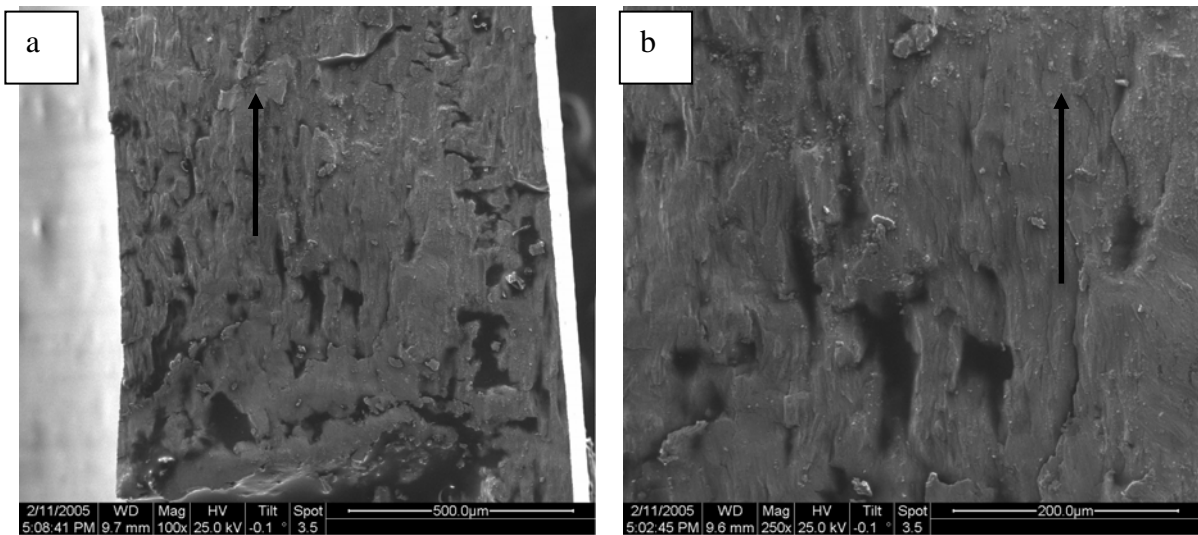


Figure 3-75. Micrograph of combined tension-torsion 901 MPa effective stress range parallel fracture at 100x (a) and 500x (b) magnification. The full width of the thin-walled tube is visible in 3-74a. Arrows point out apparent parallel trough flow along the gage section

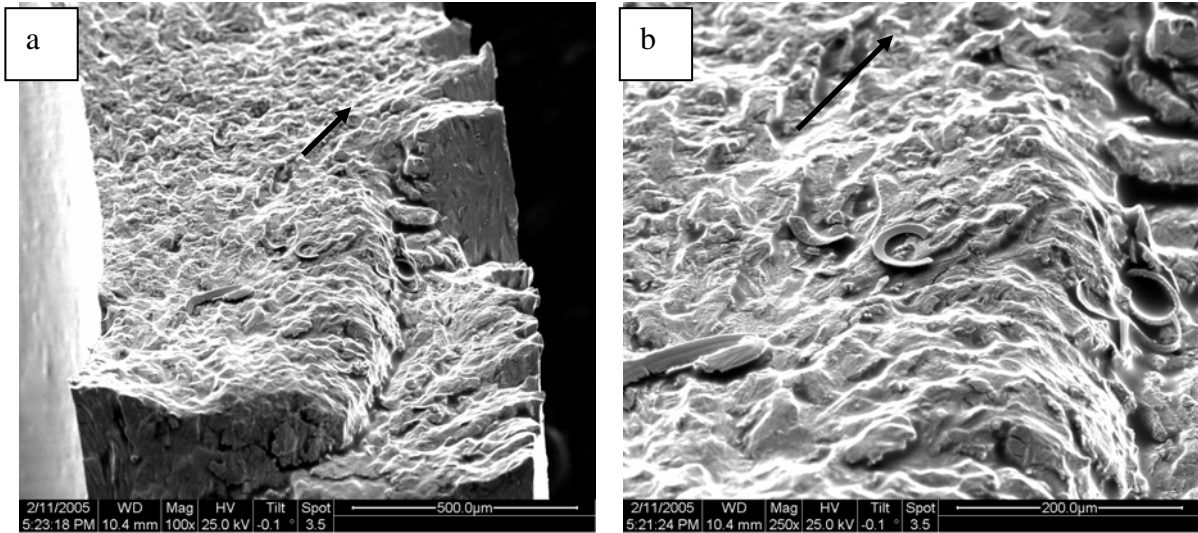


Figure 3-76. Micrograph of combined tension-torsion 901 MPa effective stress range angle fracture away from parallel fracture at 100x (a) and 500x (b) magnification. The full width of the thin-walled tube is visible in 3-75a. Arrows point out apparent trough flow away from the parallel fracture section.

#### IV. Conclusions and Recommendations

The present research effort investigated pure torsion and combined tension-torsion fatigue behavior of martensitic Nitinol at room temperature. Monotonic tests in tension and torsion were conducted to typify uni-directional stress-strain behavior establishing a modulus of elasticity of 109 GPa, an ultimate tensile strength of 957 MPa, and a shear modulus of 29 GPa.

Fully-reversed torsion fatigue tests were conducted with shear stress ranges of 416 (survived  $10^5$  cycles), 584 ( $N_f = 27789$  cycles), 674 ( $N_f = 4219$  cycles), and 1310 ( $N_f = 244$  cycles) MPa. In fully-reversed biaxial fatigue tests, a shear stress range of 500 MPa was superimposed on the axial stress ranges of 250 ( $N_f = 37018$  cycles), 500 ( $N_f = 11079$  cycles), 1000 ( $N_f = 4164$  cycles), 1120 ( $N_f = 43$  cycles), and 1500 ( $N_f = 9$  cycles) MPa.

Fatigue S-N (stress vs cycles to failure) curves were generated that can be readily used in design with appropriate safety factors. Fatigue lives obtained in torsion-dominated biaxial tests were similar to those obtained in pure torsion. Conversely, tension-dominated biaxial fatigue was significantly more damaging by decreasing fatigue lives by nearly two orders of magnitude. While less obvious than the applicability of S-N curves, it is equally important that detailed observations on the evolution of mechanical behavior with cycling are provided to guide development of experiment-based constitutive and life-prediction models. Constitutive modeling requires abundant observations and descriptions of material stress-strain behavior which are provided in this research effort. Applicability of von Mises criterion to correlating uniaxial and biaxial



test results was examined. Evolution of stress-strain behavior with cycling was discussed.

It was found that increasing axial loads in biaxial fatigue resulted in increasing axial strain ranges and increasing torsional engineering shear strain ranges though the shear stress range remained constant throughout all biaxial tests.

Finally, characterization and brief discussion of the different types and surfaces of fracture were presented in an effort to help gain understanding of the torsional and biaxial failure mechanisms of Nitinol.

Since the available information regarding torsional and biaxial cyclic fatigue behavior of Nitinol is very limited, further research opportunities are ample (11; 16). Further studies could include repeating the current effort at elevated temperatures, superimposing axial varied stress ranges on different shear stress ranges, or superimposing varied shear stress ranges on a constant axial stress range. The goal is not to understand every material property of Nitinol today, but rather to add observations and characterizations of the material fatigue behavior to the existing knowledge so that perhaps a greater understanding can be achieved tomorrow.

## Bibliography

1. American Society for Testing and Materials International (ASTM). "Standard Test Method for Shear Modulus at Room Temperature," E143-02 (2002).
2. American Society for Testing and Materials International (ASTM). "Standard Test Methods for Tension Testing of Metallic Materials," E8-04 (2004).
3. American Society for Testing and Materials International (ASTM). "Standard Test Method for Young's Modulus, Tangent Modulus, and Chord Modulus," E111-04 (2004).
4. American Society for Testing and Materials International (ASTM). "Strain-Controlled Axial-Torsional Fatigue Testing with Thin-Walled Tubular Specimens," E2207-02, (2002).
5. Clark, Cary R. and Domenic P. Marcelli. "Shape Memory Alloy Actuator Fatigue Properties," *Part of the SPIE Conference on Smart Materials Technologies, SPIE*, 3675: 311-320 (March 1999).
6. Cross, William B, Anthony H. Kariotis, and Frederick J. Stimler. "Nitinol Characterization Study," NASA CR-1433 (1969).
7. Erbstoesz, B., B. Armstrong, M. Taya, and K. Inoue. "Stabilization of the shape Memory Effect in NiTi: An Experimental Investigation," *Scripta Materialia*, 42: 1145-1150 (2000).
8. Fremond, M. and S. Miayzaki. *Shape Memory Alloys*. New York: Springer-Verlag Wien New York, 1996.
9. Jacot, Dean and Dan Clingman. "Shape Memory Alloy Consortium and Demonstration," *Smart Structures and Materials 2000: Industrial and Commercial Applications of Smart Structures Technologies SPIE*, 3991: 178-186 (2000).
10. Keefe, Andrew C. and Gregory P. Carman. "Thermo-Mechanical Characterization of Shape Memory Alloy Torque Tube Actuators," *Smart Material Structures*, 9: 665-672 (2000).
11. Keefe, Andrew C, Greg P. Carman, and A. Peter Jardine. "Torsional Behavior of Shape Memory Alloys," Department of Mechanical and Aerospace Engineering, UCLA, Northrop Corporation, El Segundo, CA.

12. Lim, T. Jesse and David L McDowell. "Mechanical Behavior of an Ni-Ti Shape Memory Alloy Under Axial-Torsional Proportional and Nonproportional Loading," *Journal of Engineering Materials and Technology*, 121: 9-18 (January 1999).
13. Liu, Yong, Zeliang Xie, and Jan Van Humbeeck. "Cyclic Deformation of NiTi shape Memory Alloys," *Materials Science and Engineering*, A273-275: 673-678 (1999).
14. Mabe, James H, Robert T. Ruggeri, Ed Rosenzweig, and Chin-Jye Yu. "NiTiNol Performance Characterization and Rotary Actuator Design," *Smart Structures and Materials Conference SPIE*, 5388-11: 1-15 (2004).
15. McKelvey, A. L. and R. O. Ritchie. "Fatigue-Crack Growth Behavior in the Superelastic and Shape-Memory Alloy Nitinol," *Metallurgical and Materials Transactions*, 32A: 731-743 (March 2001).
16. McNaney, J. M., V. Imbeni, Y. Jung, Panayiotis Papadopoulos, and R. O. Ritchie. "An Experimental Study of the Superelastic Effect in a Shape-Memory Nitinol Alloy Under Biaxial Loading," *Mechanics of Materials*, 35: 969-986 (2003).
17. McNichols, J. L, P. C. Brookes, and J. S. Cory. "NiTi Fatigue Behavior," *J. Appl. Phys*, 52(12): 7442-7444 (December 1981).
18. Melton, K. N. and O. Mercier. "Fatigue of NiTi Thermoelastic Martensites," *Acta Metallurgica*, 27: 137-144 (1979).
19. Miyazaki, S in *Engineering Aspects of Shape Memory Alloys*, T. W. Duerig, K. N. Melton, D. Stöckel, and C. M. Wayman, eds., Butterworth Heinemann, London, 1990, pp. 394-413.
20. Miyazaki, S, K. Mizukoshi, T. Ueki, T. Sakuma, and Yinong Liu. "Fatigue Life of Ti-50 at.% and Ti-40Ni-10Cu (at.%) Shape Memory Alloy Wires," *Materials Science and Engineering*, A273-275: 658-663 (1999)
21. Okabe, Nagatoshi, Maho Hosogi, Toshio Skuma, and Keisuke Okita. "A New Fatigue Model for Titanium-Nickel-Copper Shape Memory Alloy Subjected to Superelastic Cyclic Deformation," *Materials Transactions*, 43: 809-814 (2002).
22. Rejzner, J, C. Lexcellent, and B. Raniecki. "Pseudoelastic Behavior of Shape Memory Alloy Beams Under Pure Bending: Experiments and Modelling," *International Journal of Mechanical Sciences*, 44: 665-686 (2002).

23. Strnadel, B, S. Ohashi, H. Ohtsuka, T. Ishihara, and S. Miyazaki. "Cyclic Stress-Strain Characteristics of Ti-Ni and Ti-Ni-Cu Shape Memory Alloys," *Materials Science and Engineering*, A202: 148-156 (1995).
24. ----. "Effect of Mechanical Cycling on the Pseudoelasticity Characteristics of Ti-Ni and Ti-Ni-Cu Alloys," *Materials Science and Engineering*, A203: 187-196 (1995).
25. Tabanli, R. M, N. K. Simha, and B. T. Berg. "Mean Stress Effects on Fatigue of NiTi," *Materials Science and Engineering*, A273-275: 644-648 (1999).
26. ----. "Mean Strain Effects on the Fatigue Properties of Superelastic NiTi," *Metallurgical and Materials Transactions A*, 32A: 1866-1869 (July 2001).
27. Tobushi, H, T. Hashimoto, Y. Shimeno, and K. Takata. "Fatigue Properties of TiNi Shape Memory Alloy," *Materials Science Fourm*, 327-328: 151-154 (2000).
28. Tobushi, H, T. Nakahara, T. Hashimoto, Y. Shimeno, and K. Takata. "Fatigue Properties of TiNi Shape Memory Alloy and Applications to a Heat Engine and an Actuator," *Archives of Mechanics*, 51(6): 833-845 (1999).
29. Tobushi, H, S. Yamada, T. Hachisuka, A Ikai, and K Tanaka. "Thermomechanical Properties Due to Martensitic and R-Phase Transformations of TiNi Shape Memory Alloy Subjected to Cyclic Loadings," 0964-1726/96/060788 (1996).
30. Tobushi, Hisaaki, Takashi Hachisuka, Sinya Yamada, and Ping-Hua Lin. "Rotating-Bending Fatigue of a TiNi Shape-Memory Alloy Wire," *Mechanics of Materials*, 26: 35-42 (1997).

## **Vita**

Lieutenant Daniel Mark Jensen graduated from Chilton High School in Chilton, Wisconsin. He was enrolled at the University of Wisconsin-Milwaukee, Wisconsin for two years before transferring to the University of Minnesota in the Twin Cities, Minnesota. He graduated from the University of Minnesota in Spring 2001 with a Bachelor of Aerospace Engineering and Mechanics. Lieutenant Jensen was commissioned in the spring of that same year through the AFROTC program at the University of Minnesota, Detachment 415.

Lieutenant Jensen began his US Air Force career as a Laser Test Engineer at the Directed Energy Directorate, Air Force Research Laboratories (AFRL) located at Kirtland AFB in Albuquerque, New Mexico. He entered the Graduate School of Astronautical Engineering at the Air Force Institute of Technology in August 2003. Upon graduation, he will be assigned to the Space and Missile Center, Air Force Space Command located at Los Angeles AFB, CA.

<b>REPORT DOCUMENTATION PAGE</b>				<i>Form Approved OMB No. 074-0188</i>	
<p>The public reporting burden for this collection of information is estimated to average 1 hour per response, including the time for reviewing instructions, searching existing data sources, gathering and maintaining the data needed, and completing and reviewing the collection of information. Send comments regarding this burden estimate or any other aspect of the collection of information, including suggestions for reducing this burden to Department of Defense, Washington Headquarters Services, Directorate for Information Operations and Reports (0704-0188), 1215 Jefferson Davis Highway, Suite 1204, Arlington, VA 22202-4302. Respondents should be aware that notwithstanding any other provision of law, no person shall be subject to a penalty for failing to comply with a collection of information if it does not display a currently valid OMB control number.</p> <p><b>PLEASE DO NOT RETURN YOUR FORM TO THE ABOVE ADDRESS.</b></p>					
<b>1. REPORT DATE (DD-MM-YYYY)</b> 21 March 2005		<b>2. REPORT TYPE</b> Master's Thesis		<b>3. DATES COVERED (From - To)</b> August 2003 - March 2005	
<b>4. TITLE AND SUBTITLE</b>  Biaxial Fatigue Behavior of NiTi Shape Memory Alloy				<b>5a. CONTRACT NUMBER</b>	
				<b>5b. GRANT NUMBER</b>	
				<b>5c. PROGRAM ELEMENT NUMBER</b>	
<b>6. AUTHOR(S)</b>  Jensen, Daniel M., 1 <sup>st</sup> Lieutenant, USAF				<b>5d. PROJECT NUMBER</b>	
				<b>5e. TASK NUMBER</b>	
				<b>5f. WORK UNIT NUMBER</b>	
<b>7. PERFORMING ORGANIZATION NAMES(S) AND ADDRESS(S)</b> Air Force Institute of Technology Graduate School of Engineering and Management (AFIT/EN) 2950 Hobson Way, Building 640 WPAFB OH 45433-8865				<b>8. PERFORMING ORGANIZATION REPORT NUMBER</b>  AFIT/GA/ENY/05-M06	
<b>9. SPONSORING/MONITORING AGENCY NAME(S) AND ADDRESS(ES)</b> Brian Sanders, Ph.D. , AFRL/VASA 2210 8th Street, STE 1 Wright-Patterson AFB, OH 45433-7542 (v) (937) 255-8296				<b>10. SPONSOR/MONITOR'S ACRONYM(S)</b> AFRL/VASA	
				<b>11. SPONSOR/MONITOR'S REPORT NUMBER(S)</b>	
<b>12. DISTRIBUTION/AVAILABILITY STATEMENT</b>  APPROVED FOR PUBLIC RELEASE; DISTRIBUTION UNLIMITED.					
<b>13. SUPPLEMENTARY NOTES</b>					
<b>14. ABSTRACT</b> <p>Nitinol is a shape memory alloy (SMA) capable of martensite-to-austenite phase transformations enabling shape-memory behavior. Shape-memory properties make Nitinol a strong candidate material for use in aircraft applications such as actuators. Structural integrity and reliability of torque tube actuators must be assured before this material can be used in flight-critical components. Thorough understanding of the fatigue response of the material is essential for a structurally-sound SMA actuator design. The present effort investigates pure torsion and combined tension-torsion fatigue behavior of Nitinol at room temperature. Monotonic tests in tension and torsion were conducted to typify uni-directional stress-strain behavior. Fully-reversed torsion fatigue tests were conducted with shear stress ranges of 416, 584, 674, and 1310 MPa. In fully-reversed biaxial fatigue tests, a shear stress range of 500 MPa was superimposed on the axial stress ranges of 250, 500, 1000, 1120, and 1500 MPa. Fatigue behavioral characteristics, including fatigue S-N curves were established. Fatigue lives obtained in torsion-dominated biaxial tests were similar to those obtained in pure torsion. Conversely, tension-dominated biaxial fatigue was significantly more damaging, resulting in decreased fatigue lives. Applicability of von Mises criterion to correlating uniaxial and biaxial test results was examined. Evolution of stress-strain behavior with cycling is discussed.</p>					
<b>15. SUBJECT TERMS</b> Nitinol, NiTi, Shape Memory Alloy, Biaxial Fatigue, Fatigue, Combined Tension-Torsion					
<b>16. SECURITY CLASSIFICATION OF:</b>			<b>17. LIMITATION OF ABSTRACT</b>	<b>18. NUMBER OF PAGES</b>	<b>19a. NAME OF RESPONSIBLE PERSON</b>
a. REPORT	b. ABSTRACT	c. THIS PAGE			<b>19b. TELEPHONE NUMBER (Include area code)</b>
U	U	U	UU	101	Marina Ruggles-Wrenn (937) 255-3636, ext 4641 Marina.ruggles-wrenn@afit.edu